

---

# Numerical modeling to estimate the impact of built infrastructure on permafrost degradation

## Case study from Ilulissat, Greenland

Thesis for the Degree Master of Science

---

### **AUTHOR**

Luisa Näke - 581152 (NTNU), s202351 (DTU)

### **SUPERVISORS**

Seyed Ali Ghoreishian Amiri - NTNU  
Thomas Ingeman-Nielsen - DTU  
Frederieke Miesner - AWI  
Julia Boike - AWI

July 21, 2023

## Acknowledgements

I would like to thank everyone who contributed to the success of this thesis.

In particular, I would like to thank my supervisors for their regular, critical and supportive mentoring. These include Frederieke Miesner and Julia Boike from the Permafrost Research Section of Alfred Wegener Institute (AWI), Thomas Ingeman-Nielsen from the Department of Environmental and Resource Engineering of Technical University of Denmark (DTU) and Seyed Ali Ghoreishian Amiri from the Department of Civil and Environmental Engineering of Norwegian University of Science and Technology (NTNU).

In particular, Frederieke Miesner (AWI) and Sebastian Westermann (University of Oslo) helped me in understanding the CryoGrid community model and debugging the code.

Furthermore, I would like to thank Johanna Scheer (PhD candidate at DTU), Thomas Ingeman-Nielsen and the Greenland Survey "ASIAQ" for providing and using (partly preprocessed) measurement data from Ilulissat.

Special thanks also go to all proofreaders from the SPARC (Sensitivity of Permafrost in the Arctic) group of the AWI in Potsdam, in particular Julia Boike, Maybrit Goldau, Jannika Gottuk, Brian Groenke, Jennika Hammar, Daniela Hollenbach Borges, Frederieke Miesner and Marie Rolf as well as Seyed Ali Ghoreishian Amiri from NTNU and Philipp Näke. Furthermore I thank my family, who also supported me during the whole thesis phase.

## Abstract

Infrastructure in permafrost landscapes affects the ground thermal regime and may enhance permafrost degradation. The stability and usability of the infrastructure depend likewise on the thermal conditions of the subsurface. The study area in Ilulissat (West Greenland) is affected by typically warm and often ice-rich permafrost. Consequently, the infrastructure is likely to accelerate thawing of the ground. Numerical models can be used to estimate the influence of infrastructure on permafrost degradation, subsidence, and ponding near roads.

In this study, I investigated the influence of roads in Ilulissat using a specific configuration of the one-dimensional, laterally coupled heat-transfer model CryoGrid, which is part of a larger toolbox capable of simulating various processes. I used ERA5 reanalysis data (1980–2020) and MPI-ESM model projections according to the SSP5–8.5 scenario (2020–2100) as climate forcing and validated them with site data from the local weather station (1991–2021). Borehole data from Ilulissat and the north-eastern surroundings provide information on soil stratigraphy properties to first build the model for the natural, undisturbed tundra. I subsequently added the elevated gravel embankment as linear infrastructure to the model with several tiles for the roadway and the shoulder. In additional model runs, I quantified the effect of snow by changing the snow distribution near the road to imitate plowing as well as thermal properties, excess ice layer and road albedo. I utilized observations from the weather station and iButton ground surface temperature sensors for validation of the model runs.

My simulations show that the construction of a road had a direct influence on the thermal regime by warming the soil. A general deepening of the active layer was projected within the current century, which is supported by borehole observations. Likewise, the associated measures of maintenance such as accumulation of cleared snow affected the response of the soil, as an insulator of the embankment, preventing stored heat from escaping. Furthermore, the effects of a darker road surface, the thermal properties of the gravel and the accelerated thawing and ponding due to the presence of excess ice were observed. As the current state of permafrost is vulnerable to climate change, it is important to rely on models to provide realistic projections.

## Contents

<b>Acknowledgements</b>	<b>i</b>
<b>Abstract</b>	<b>ii</b>
<b>List of Figures</b>	<b>v</b>
<b>List of Tables</b>	<b>x</b>
<b>Nomenclature</b>	<b>xi</b>
<b>List of Abbreviations</b>	<b>xii</b>
<b>Introduction</b>	<b>1</b>
Objective and scope of the work . . . . .	1
Structure . . . . .	1
<b>1 Theory</b>	<b>2</b>
1.1 Permafrost . . . . .	2
1.2 Road construction in permafrost regions . . . . .	6
1.2.1 Challenges . . . . .	6
1.2.2 Solutions . . . . .	9
1.2.3 Thermal modeling through and under embankments . . . . .	9
<b>2 Methods</b>	<b>11</b>
2.1 Model scales and challenges . . . . .	11
2.2 Climate . . . . .	13
2.3 Forcing data . . . . .	13
2.3.1 Reanalysis data . . . . .	13
2.3.2 Projection models . . . . .	14
2.3.3 Connection and downscaling algorithm . . . . .	15
2.4 Ground thermal regime . . . . .	16
2.4.1 Boreholes . . . . .	16
2.4.2 iButtons . . . . .	16
2.5 CryoGrid community model . . . . .	17
2.5.1 CryoGrid classes . . . . .	20
2.6 Initialization bias . . . . .	22
<b>3 Case - Ilulissat, West Greenland</b>	<b>24</b>
3.1 Climate . . . . .	25
3.1.1 Weather station . . . . .	25
3.1.2 Climate forcing . . . . .	27
3.2 Ground thermal regime . . . . .	28
3.2.1 Borehole data . . . . .	28
3.2.2 iButton data . . . . .	31
3.3 Road construction . . . . .	33
3.4 Model setup . . . . .	34

<b>4 Results</b>	<b>39</b>
4.1 Forcing data . . . . .	39
4.1.1 Temperature . . . . .	39
4.1.2 Snowfall . . . . .	44
4.2 Ground thermal regime . . . . .	45
4.2.1 Boreholes . . . . .	45
4.2.2 iButtons . . . . .	48
4.3 CryoGrid model runs . . . . .	50
4.3.1 Initialization bias . . . . .	50
4.3.2 Scenario a) Standard scenario . . . . .	51
4.3.3 Scenario b) Low road albedo . . . . .	54
4.3.4 Scenario c) Low road albedo and cleared embankment . . . . .	57
4.3.5 Scenario d) Embankment cleared from snow . . . . .	60
4.3.6 Scenario e) Changed gravel layer properties . . . . .	63
4.3.7 Scenario f) Excess ice . . . . .	66
4.4 Comparison of the scenarios . . . . .	69
4.4.1 Influence of road surface color . . . . .	70
4.4.2 Influence of road layer properties . . . . .	71
4.4.3 Influence of excess ice in the ground . . . . .	72
4.4.4 Influence of snow removal practice . . . . .	72
<b>5 Discussion</b>	<b>74</b>
5.1 Forcing data . . . . .	74
5.2 Model results . . . . .	77
5.3 Road construction . . . . .	81
<b>6 Conclusion</b>	<b>82</b>
<b>References</b>	<b>I</b>
<b>Appendices</b>	<b>XV</b>
<b>A Dalton Highway, Alaska</b>	<b>XV</b>
<b>B Temperature profiles old boreholes</b>	<b>XXI</b>
<b>C Trumpet plots</b>	<b>XXIII</b>

## List of Figures

1	Map of permafrost zonation in the Northern Hemisphere based on classified modelled permafrost probabilities . . . . .	2
2	Typical temperature curve (trumpet curve) from a permafrost environment and terms used for different zones and boundaries . . . . .	3
3	Schematic representation of the formation of open-system and closed-system pingos .	5
4	Selected damages of a road cross section in permafrost environment . . . . .	8
5	Classification of model classes with their temporal and spatial scale . . . . .	11
6	Hierarchy of the types of CryoGrid classes required for multi-physics simulations within the CryoGrid community model . . . . .	17
7	Example of a CryoGrid stratigraphy in a one-dimensional tile class with three stratigraphy classes coupled by interaction classes . . . . .	18
8	Schematic representation of the CryoGrid stratigraphy when a snow cover is present	18
9	Schematic representation of the CryoGrid stratigraphy interacting with a lateral interaction (IA) class . . . . .	19
10	CryoGrid stratigraphy in the tile class TILE_1D_standard with two stratigraphy classes . . . . .	21
11	Example of a transient mean function due to initialization of a simulation program .	23
12	Map of the Ilulissat area with inserted small map of Greenland with selected place names . . . . .	24
13	Temperature course for a standard year in Ilulissat between 1991 and 2020 . . . . .	25
14	Climate graph with temperature (1961-1990) and precipitation (1961-1984) for Ilulissat	26
15	Wind rose of Ilulissat with frequency of wind direction (%) and wind speed (m/s) . .	27
16	Map with grid points of ERA5, MPI-ESM, NorESM and the points of interest in the West Greenland region around Ilulissat . . . . .	27
17	Street map of Ilulissat with locations of the boreholes . . . . .	30
18	Terrain map of Ilulissat with locations of the boreholes . . . . .	30
19	iButton network deployed in Ilulissat for the year 2020-2021 . . . . .	32
20	Close-up of the location of the iButtons sensors that are close to the road with their data recording period . . . . .	32
21	Schematic standardised cross section of a road on permafrost subsoil . . . . .	33
22	Schematic half cross section showing the modelled road center to adjacent tundra in Ilulissat . . . . .	34
23	Schematic half cross section showing the modelled road center to adjacent tundra in Ilulissat with double amount of snow on shoulder and toe and single amount of snow on the tundra . . . . .	36
24	Schematic half cross section showing the modelled road center to adjacent tundra in Ilulissat with shoulder cleared from snow, toe with double amount of snow and tundra single amount of snow . . . . .	36
25	Schematic half cross section from the road centre to the adjacent tundra in Ilulissat with excess ice layer between 1 m and 2 m depth . . . . .	38
26	Comparison of 2 m temperature from ERA5 reanalysis data with measured 2 m air temperature from DMI's weather station . . . . .	39
27	Closeup for the comparison of 2 m temperature from ERA5 reanalysis data with measured 2 m air temperature from DMI's weather station . . . . .	39

28	Correlation of the 2 m temperature of ERA5 reanalysis data with measured 2 m air temperature data from DMI's weather station . . . . .	40
29	Freezing and thawing degree indices for the climate forcing ERA5, MPI-ESM and the weather station from DMI. . . . .	41
30	Mean annual air temperature from ERA5 and MPI-ESM with the corresponding temperature differences . . . . .	42
31	Weekly averaged maximum, mean and minimum 2 m air temperature for the first week and the 20 <sup>th</sup> week for each year . . . . .	42
32	Weekly averaged changes in slope of the mean 2 m air temperature for 12 projection intervals for the period 2020-2093 based on MPI-ESM SSP5-8.5 . . . . .	43
33	Weekly averaged changes in slope of the mean 2 m air temperature for projection period 2020-2093 based on the MPI-ESM SSP5-8.5 . . . . .	43
34	Accumulated snowfall per season from August, 01 <sup>st</sup> to July, 31 <sup>st</sup> for the climate forcing ERA5 + MPI-ESM and the weather station from DMI. . . . .	44
35	First and last day of snowfall [day of year (DOY)] for the climate forcing ERA5 + MPI-ESM and the weather station from DMI. . . . .	45
36	Comparison between the air temperature and the temperature at 1.5 m depth in borehole 79012 from ASIAQ from July 1980 to April 1981 . . . . .	46
37	Comparison between the air temperature and the temperatures per depth in borehole ILU2018-03 from DTU between August 2018 and October 2019 . . . . .	46
38	Temperature distribution of borehole ILU2018-03 for the period from October 2018 to September 2019 and simulated ground temperatures with CryoGrid based on a single tundra tile . . . . .	47
39	Ground surface temperature of iButton sensors in Ilulissat for three selected roadside locations and their snow accumulation effect. . . . .	49
40	Standard deviation for the initialization bias for the depth 0.2 m and depth 3.0 m trough out the year . . . . .	50
41	Simulated temporal evolution of thaw depth with the indicated yearly maximum thaw depth for the tundra tile in the scenario a) . . . . .	51
42	Simulated temporal evolution of maximum thaw depth for all structural units with annual means and 5-year moving means for standard scenario a) . . . . .	52
43	Modelled trumpet curve for road tile with max., mean, and min. temperatures within the specified years 2000, 2020, 2050, 2075, and 2090 for standard scenario a) . . . . .	53
44	Modelled trumpet curve for tundra tile with max., mean, and min. temperatures within the specified years 2000, 2020, 2050, 2075, and 2090 for the standard scenario a) . . . . .	53
45	Simulated ground temperatures in the road, shoulder, toe, and adjacent tundra at the end of winter and summer for past, present, and future climate conditions for the standard scenario a) . . . . .	54
46	Simulated temporal evolution of maximum thaw depth for all structural units with annual means and 5-year moving means for scenario b) with low road albedo . . . . .	55
47	Modelled trumpet curve for road tile with max., mean, and min. temperatures within the specified years 2000, 2020, 2050, 2075, and 2090 for scenario b) with low road albedo. . . . .	56

48	Modelled trumpet curve for tundra tile with max., mean, and min. temperatures within the specified years 2000, 2020, 2050, 2075, and 2090 for scenario b) with low road albedo. . . . .	56
49	Simulated ground temperatures in the road, shoulder, toe, and adjacent tundra at the end of winter and summer for past, present, and future climate conditions for scenario b) with low road albedo . . . . .	57
50	Simulated temporal evolution of maximum thaw depth for all structural units with annual means and 5-year moving means for scenario c) with low road albedo and cleared shoulder . . . . .	58
51	Modelled trumpet curve for road tile with max., mean, and min. temperatures within the specified years 2000, 2020, 2050, 2075, and 2090 for scenario c) with low road albedo and cleared shoulder . . . . .	59
52	Modelled trumpet curve for tundra tile with max., mean, and min. temperatures within the specified years 2000, 2020, 2050, 2075, and 2090 for scenario c) with low road albedo and cleared shoulder . . . . .	59
53	Simulated ground temperatures in the road, shoulder, toe, and adjacent tundra at the end of winter and summer for past, present, and future climate conditions for scenario c) with low road albedo and cleared shoulder . . . . .	60
54	Simulated temporal evolution of maximum thaw depth for all structural units with annual means and 5-year moving means for scenario d) with embankment cleared from snow . . . . .	61
55	Modelled trumpet curve for road tile with max., mean, and min. temperatures within the specified years 2000, 2020, 2050, 2075, and 2090 for scenario d) with shoulder cleared from snow . . . . .	62
56	Modelled trumpet curve for tundra tile with max., mean, and min. temperatures within the specified years 2000, 2020, 2050, 2075, and 2090 for scenario d) with shoulder cleared from snow . . . . .	62
57	Simulated ground temperatures in the road, shoulder, toe, and adjacent tundra at the end of winter and summer for past, present, and future climate conditions for scenario d) with the shoulder cleared from snow . . . . .	63
58	Simulated temporal evolution of maximum thaw depth for all structural units with annual means and 5-year moving means for scenario e) with changed gravel layer properties . . . . .	64
59	Modelled trumpet curve for road tile with max., mean, and min. temperatures within the specified years 2000, 2020, 2050, 2075, and 2090 for scenario e) with changed gravel layer properties . . . . .	65
60	Modelled trumpet curve for tundra tile with max., mean, and min. temperatures within the specified years 2000, 2020, 2050, 2075, and 2090 for scenario e) with changed gravel layer properties . . . . .	65
61	Simulated ground temperatures in the road, shoulder, toe, and adjacent tundra at the end of winter and summer for past, present, and future climate conditions for scenario e) with changed gravel layer properties . . . . .	66
62	Simulated temporal evolution of maximum thaw depth for all structural units with annual means and 5-year moving means for scenario f) with excess ice between $-1$ and $-2$ m . . . . .	67

63	Modelled trumpet curve for the road tile with max., mean, and min. temperatures within the specified years 2000, 2020, 2050, 2075, and 2090 for scenario e) with excess ice between $-1$ and $-2$ m . . . . .	68
64	Modelled trumpet curve for tundra tile with max., mean, and min. temperatures within the specified years 2000, 2020, 2050, 2075, and 2090 for scenario e) with excess ice between $-1$ and $-2$ m . . . . .	68
65	Simulated ground temperatures in the road, shoulder, toe, and adjacent tundra at the end of winter and summer for past, present, and future climate conditions for scenario f) with excess ice between $-1$ and $-2$ m . . . . .	69
66	Simulated temporal evolution of change of maximum thaw depth for all structural units with difference in scenarios a) and b) as well as c) and d) to see the influence of change in road albedo . . . . .	70
67	Simulated temporal evolution of change of maximum thaw depth for all structural units with difference in scenarios a) and e) to see the influence of change in road layer properties . . . . .	71
68	Simulated temporal evolution of change of maximum thaw depth for all structural units with difference in scenarios a) and f) to see the influence of excess ice . . . . .	72
69	Simulated temporal evolution of change of maximum thaw depth for all structural units with difference in scenarios a) and d) as well as b) and c) to see the influence of snow removal from the shoulder . . . . .	73
70	Observed and projected anomalies in 2-meter air temperature averaged over the land portion of the BBDS region . . . . .	75
71	Observed and projected anomalies anomalies in total (liquid and solid) precipitation averaged over the land portion of the BBDS region . . . . .	76
72	Mean Annual Air Temperature, Modelled Active Layer Thickness and Modelled ground unfrozen water content ratio over time . . . . .	78
73	Modelled half cross section from the road centre to the adjacent tundra in Dalton . .	XV
74	Simulated ground temperatures for the Dalton Highway by Schneider von Deimling et al. (2021) in the road embankment, subgrade, and adjacent tundra at the end of winter and summer for past, present day, and future climate conditions . . . . .	XVII
75	Simulated ground temperatures for the Dalton Highway by myself in the road embankment, subgrade, and adjacent tundra at the end of winter and summer for past, present day, and future climate conditions . . . . .	XVII
76	Temporal evolution of maximum thaw depth (MTD) for Dalton Highway from Schneider von Deimling et al. (2021) for all structural units under RCP8.5 warming - conservative case without ponding at the toe. . . . .	XVIII
77	Temporal evolution of maximum thaw depth (MTD) for Dalton Highway from my model results for all structural units under RCP8.5 warming - conservative case without ponding at the toe. . . . .	XVIII
78	Simulated ground temperatures for the Dalton Highway by myself (with excess ice) in the road embankment, toe, and adjacent tundra at the end of winter and summer for past, present day , and future climate conditions . . . . .	XIX
79	Temporal evolution of maximum thaw depth for Dalton Highway from vulnerable case of Schneider von Deimling et al. (2021) for all structural units under RCP8.5 warming - conservative case without ponding at the toe . . . . .	XX

80	Temporal evolution of maximum thaw depth for Dalton Highway with excess ice from my model results for all structural units under RCP8.5 warming - conservative case without ponding at the toe . . . . .	XX
81	Modelled trumpet curve for road tile with max., mean, and min. temperatures within the specified years 2000, 2020, 2050, 2075, and 2090 for Dalton . . . . .	XXI
82	Modelled trumpet curve for road tile with max., mean, and min. temperatures within the specified years 2000, 2020, 2050, 2075, and 2090 for Dalton . . . . .	XXI
83	Temperature profiles of some two old boreholes at the airport in Ilulissat from August 1979 to April 1981 with temperatures measured in three different depths. . . . .	XXII
84	Temperature trumpet of borehole ILU2018-04 for 2020 . . . . .	XXIII
85	Temperature trumpet of borehole ILU16001T for 2018 . . . . .	XXIII
86	Temperature trumpet of borehole ILU16002T for 2018 . . . . .	XXIII
87	Temperature trumpet of borehole ILU16005T from August 2017 to July 2018 . . .	XXIII
88	Temperature trumpet of borehole ILU16009T for 2020 . . . . .	XXIV
89	Temperature trumpet of borehole ILU16010T for 2018 . . . . .	XXIV
90	Temperature trumpet of borehole ILU16011T for 2018 . . . . .	XXIV
91	Temperature trumpet of borehole ILU16015T for 2018 . . . . .	XXIV
92	Temperature trumpet of borehole ILU16019T for 2018 . . . . .	XXV
93	Temperature trumpet of borehole ILU16022T for 2018 . . . . .	XXV

## List of Tables

1	Initial temperature profile for the CryoGrid Community Model in Ilulissat . . . . .	28
2	Overview of DTU-boreholes from 2016, 2018 and 2021 in the Ilulissat area . . . . .	29
3	Overview of the locations of the iButton sensors for the three selected locations . . .	31
4	Overview of the modelled scenarios and their characteristic properties with regard to the distribution of snow, the composition and surface of the road, and the presence of excess ice . . . . .	35
5	Model parameters in the CryoGrid Community model . . . . .	35
6	Ground stratigraphies with volumetric fractions of the ground constituents for the standard scenario . . . . .	37
7	Ground stratigraphies with volumetric fractions of the ground constituents for the szenario with excess ice . . . . .	37
8	Freezing and thawing indices $I_f$ and $I_t$ from DMI weather station and ERA5 reanalysis data . . . . .	41

## Nomenclature

$\alpha$	Albedo [–]
$\phi$	Porosity [–]
$\rho_s$	Snow density [ $kg/m^3$ ]
$\theta_i$	Volumetric fraction of the ice [–]
$\theta_m$	Volumetric fraction of the minerals [–]
$\theta_o$	Volumetric fraction of the organics [–]
$\theta_w$	Volumetric fraction of the water [–]
$\theta_{\chi i}$	Volumetric fraction of the excess ice [–]
$\theta_{fc}$	Volumetric fraction of the field capacity [–]
$c_m$	Volumetric heat capacity of the mineral [ $J/(Km^3)$ ]
$I_f$	Freezing index [ $^{\circ}d$ ]
$I_t$	Thawing index [ $^{\circ}d$ ]
$k$	Hydraulic conductivity [ $m/s$ ]
$k_m$	Thermal conductivity of the mineral [ $W/(mK)$ ]
$K_{w,sat}$	Saturated hydraulic conductivity [ $m/s$ ]
$Q_{geo}$	Geothermal heat flux [ $W/m^2$ ]
$S_p$	Salinity [–]
$S_{r,i}$	Ice saturation of the pores [–]
$w$	Water content [–]

## List of Abbreviations

- ACE** Air Convection Embankments
- AL** active layer
- AWI** Alfred Wegener Institute
- BBDS** Baffin Bay/Davis Strait
- C3S** Copernicus Climate Change Service
- CMIP** Coupled Model Intercomparison Project
- DEM** digital elevation model
- DMI** Danmarks Meteorologiske Institut
- DOY** day of year
- DTU** Technical University of Denmark
- ECMWF** European Centre for Medium-Range Weather Forecasts
- ERA** ECMWF reanalysis
- ERA5** fifth generation ECMWF atmospheric reanalysis
- ESMs** Earth system models
- GTM**s Geotechnical models
- IPCC** Intergovernmental Panel on Climate Change
- LSMs** Land surface models
- MAAT** mean annual air temperature
- MAGT** mean annual ground temperature
- MPI-ESM** Max-Planck Institute - Earth System Model
- MTD** maximum thaw depth
- netCDF** Network Common Data Format
- NorESM** Norwegian Earth System Model
- NTNU** Norwegian University of Science and Technology
- POI** point of interest
- PTMs** Process-based tiling models
- QTR** Qinghai-Tibet Railway

**RCM** regional climate model

**RCP** representative concentration pathways

**SEB** surface energy balance

**SSP** Shared Socioeconomic Pathways

**THM** thermo-hydro-mechanical

**TTOP** temperature at the top of the permafrost

**WCRP** World Climate Research Programme

**WGCM** Working Group on Coupled Modelling

**ZAA** zero annual amplitude

## Introduction

### Objective and scope of the work

I prepared this thesis to obtain the academic degree "M.Sc. Cold Climate Engineering" from NTNU / "M.Sc. Civil Engineering" from DTU.

The thesis aims to estimate the thermal degradation of permafrost surrounding and beneath roads in Ilulissat, Greenland. For this purpose, different parameters and their influence on the temperatures in the soil are investigated. Parameters to be investigated include the presence of excess ice, snow removal practice or road albedo and their combinations. For the implementation of these goals, the CryoGrid community model is used. The objectives of my thesis are to transfer an existing model (Schneider von Deimling et al. 2021) to the CryoGrid community model and to Ilulissat conditions. Field data, climate reanalysis, and projection data are used to draw conclusions on thermal regime, subsidence and ponding. The infrastructure is added with different scenarios to study changes on the soil temperatures and the influence of snow-redistribution next to the road.

### Structure

In the thesis, I first describe some background information on permafrost and road construction as well as the methods for model scales, climate, forcing data, ground thermal regime and the utilised CryoGrid community model. Since this thesis is a case study for Ilulissat in Greenland, the data used for input values into the model as well as for its validation are described in more detail. The scenarios are also presented and the model setup is shown. Finally, the results of the forcing data, the ground thermal regime and the different CryoGrid scenarios are shown, compared and discussed. In the appendix, the comparison to the paper by Schneider von Deimling et al. (2021) for the Dalton Highway in Alaska is shown, which served as a personal introduction to CryoGrid.

# 1 Theory

In this section, I introduce permafrost on a general basis, different features and processes that are unique for permafrost environments. Furthermore, road constructions in permafrost regions and their challenges and solutions are described in a general, not site-specific setting.

## 1.1 Permafrost

Permafrost is a unique and critical component of Earth's cryosphere, representing an important but fragile constituent of the global climate system. It is defined as ground that remains frozen at or below  $0^{\circ}\text{C}$  for at least two consecutive years (National Snow and Ice Data Center 2023c). Permafrost is a distinctive feature of cold regions on Earth. It underlies 13 to 18 % of the exposed land surface in the Northern Hemisphere and 9 to 14 % of the exposed land surface globally (Obu 2021, Gruber 2012). Permafrost is found in a wide range of environments, from the High Arctic and Antarctic to high mountain regions and boreal forests (Figure 1). In the Northern Hemisphere it occurs primarily in high latitudes, including regions of North America, Europe, and Asia. Permafrost is also found in some high-altitude regions, such as the Andes, the Alps and the Tibetan Plateau. While most permafrost is on land, there is also some subsea permafrost beneath offshore Arctic

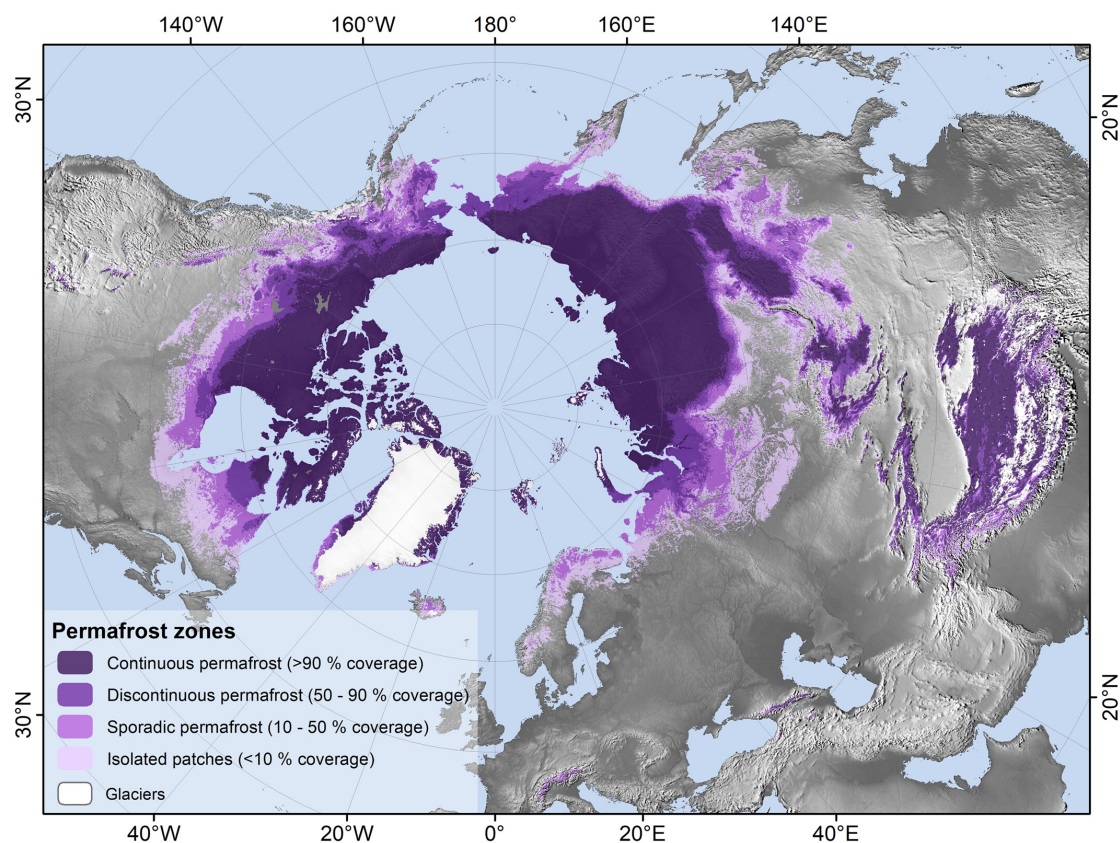


Figure 1: Map of permafrost zonation in the Northern Hemisphere based on classified modelled permafrost probabilities (Obu (2021), adapted from Obu et al. (2019)). Permafrost zones are classified in continuous, discontinuous and sporadic permafrost as well as isolated patches and glaciers.

continental shelves (Overduin et al. 2019). Permafrost plays a critical role in shaping landscapes, influencing hydrological processes, regulating carbon dynamics, and supporting unique ecosystems (Schuur & Mack 2018, Nitzbon et al. 2019, Cahoon et al. 2022, Schwamborn et al. 2023, Gao et al. 2023, Wang et al. 2023). However, permafrost is highly vulnerable to climate change, and its degradation can have significant environmental, social, and economic impacts on both local and global scales (Timlin et al. 2021, Allard et al. 2012, Jungsberg et al. 2022, Tomaskovicova et al. 2021, Scheer et al. 2021).

Permafrost is characterized by the presence of ice and its amount within the soil matrix, which imparts unique properties to the ground. The ice in the ground can exist in various forms, including ice lenses, ice wedges, and massive ice bodies, and can constitute a significant portion of the ground's volume, ranging from a few percent up to 100 % in case of excess ice with pure ice layers (Obu 2021). In thickness, permafrost ranges from less than 1 m to greater than 1500 m (National Snow and Ice Data Center 2023c).

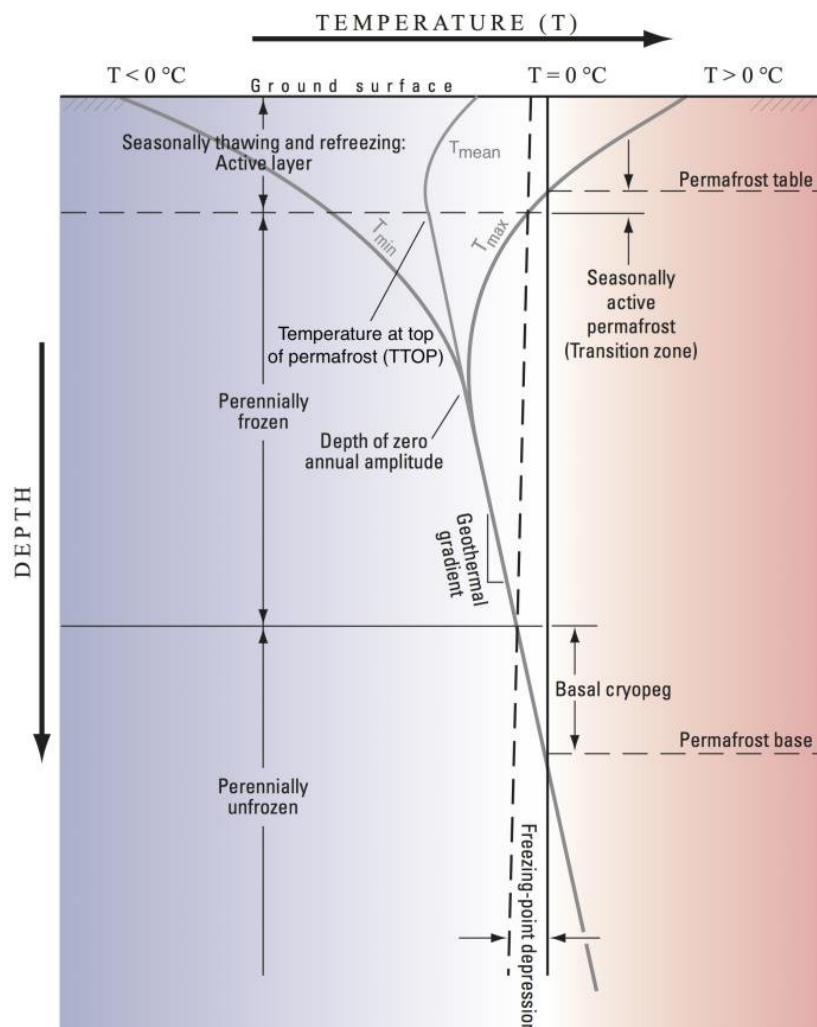


Figure 2: Typical temperature curve (trumpet curve) from a permafrost environment and terms used for different zones and boundaries (Hornum 2018).

Typical parameters associated with permafrost are explained using Figure 2. The maximum annual thaw depth is referred to as the active layer (AL) thickness. The mean annual temperature at this depth is referred to as temperature at the top of the permafrost (TTOP). Permafrost is very sensitive to changes in air temperature. Temperature variations at the ground surface (terrain level) are typically much greater than in deeper layers due to external influences such as air temperature and decrease with increasing depth. When the influence of the fluctuations diminishes, the permafrost temperature remains relatively constant over longer periods of time. The depth, where annual variations in temperature is less than  $0.1\text{ }^{\circ}\text{C}$  is called zero annual amplitude (ZAA), which is also a characteristic indicator of the thermal regime and stability of permafrost. At great depths, the geothermal gradient plays a role, leading to increased warming towards the permafrost base, where the soil is in a thawed state. Furthermore, the freezing of the soil can be delayed to some extent, as the presence of saline ground, for example, delays the transition to the frozen state by a few  $^{\circ}\text{C}$  (Chuvilin et al. 2022).

Permafrost is classified as continuous, discontinuous, sporadic and isolated. In the continuous area, 90 to 100 % of the ground is frozen, typically with the mean annual air temperature (MAAT) at or below  $0\text{ }^{\circ}\text{C}$  (National Snow and Ice Data Center 2023c). In areas, where the MAAT is typically slightly warmer but can be still below  $0\text{ }^{\circ}\text{C}$ , there is discontinuous permafrost with 50 to 90 % frozen ground. Sporadic permafrost with 10 to 50 % and isolated patches with 0 to 10 % as permanently frozen ground in cold regions are zoned in Figure 1 as well. For the latter, cold microclimates and specific vegetation or surface conditions are important, as is the case for alpine permafrost. Apart from terrestrial permafrost, there is also subsea permafrost, which lies below the seabed after the past ice ages due to rising sea levels (Osterkamp & Sherman 2019). Based on model analyses, this appears to be thinning (Overduin et al. 2019).

Permafrost regions are characterized by distinctive landforms shaped by the processes of freeze-thaw cycles and the presence of subsurface ice. Thermokarst is a landforming process in periglacial areas characterised by thawing in the upper parts of the permafrost. The thawing of the ice in the soil causes a loss of volume, which causes the soil to subside. The greater the ice content in the soil, the greater the thermokarst effect. Thermokarst lakes are formed when permafrost thaws and releases water, which in turn leads to greater thawing of the underlying ground (National Snow and Ice Data Center 2023c). The unfrozen ground under water bodies, infrastructure or other insulating objects surrounded by permafrost is called talik. With time and the addition of water, a pingo can form on it (Figure 3). In permafrost landscapes there exists massive ice or excess ice, which is the volume of ice in the ground that exceeds the total pore volume that the ground would have under natural unfrozen conditions (National Snow and Ice Data Center 2023a) and has to be fed with sufficient water to form. These are large ice masses in the ground, for example in the form of ice wedges, pingos, buried ice or large ice lenses (National Snow and Ice Data Center 2023b). Ice wedges can form in the soil when it cracks due to cold temperatures, snow melt water penetrates, refreezes and expands (Mackay 1993). The ground tends to crack again later in the same place, allowing ice wedges to grow. The increase in volume lifts the ground and creates rims, which are typical for the formation of polygons or other shapes called patterned ground.

Permafrost is particularly sensitive to changes in air temperature and snow cover, and as a result of ongoing global warming permafrost is undergoing rapid degradation in many parts of the world (Schneider von Deimling et al. 2021, Liu et al. 2020, Haynes et al. 2019). The Arctic has

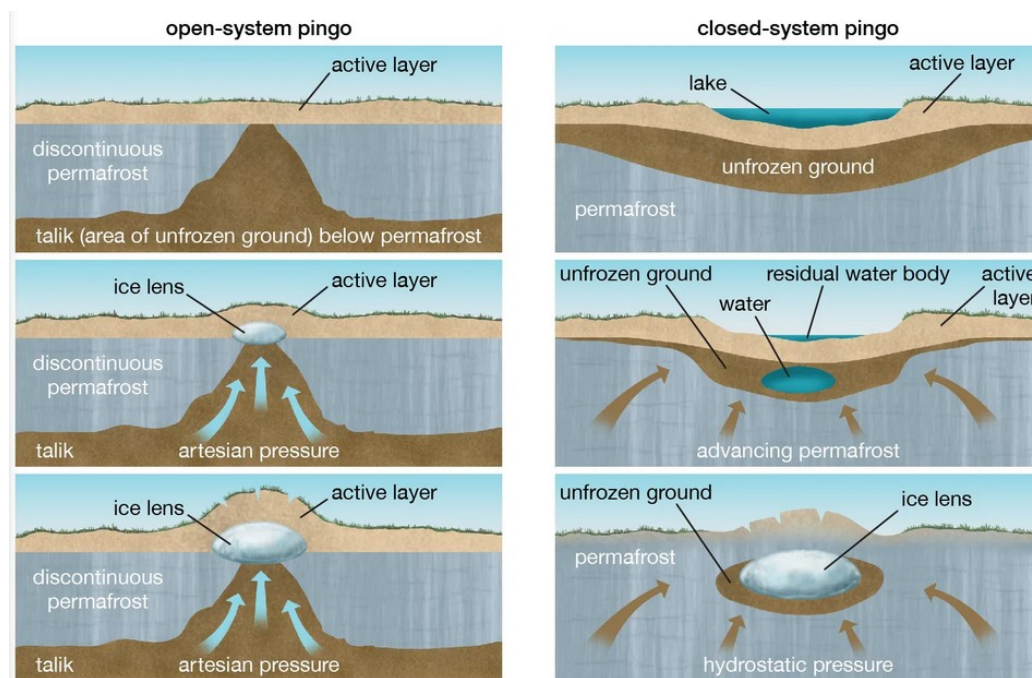


Figure 3: Schematic representation of the formation of open-system and closed-system pingos (Encyclopædia Britannica Inc. 2023).

experienced warming at twice the rate of the global average over the past few decades, resulting in permafrost thawing and subsidence of the land surface (Günther et al. 2015, Foster et al. 2022). The impacts of permafrost degradation are wide-ranging and complex, affecting various environmental and socio-economic aspects.

Permafrost contains a large amount of organic carbon, estimated to be twice the amount of carbon stored in the Earth's atmosphere (Schuur et al. 2008, 2009, Tamocai et al. 2009, Epstein 2013). As a consequence of the changing climate, the ground warms due to rising temperatures, frozen sediments thaw and release organic carbon (Biskaborn et al. 2019). This creates a positive feedback loop, where climate change leads to permafrost thaw, which in turn releases more greenhouse gases, exacerbating global warming (Schuur & Abbott 2011, Grosse et al. 2011).

Permafrost plays a crucial role in regulating hydrological processes in cold regions. It acts as a barrier that prevents water from infiltrating into the ground, leading to the formation of unique ecosystems such as wetlands and peatlands (Gautier 2021, Treat et al. 2022). However, permafrost degradation can disrupt the hydrological balance, resulting in changes to surface water and groundwater dynamics, increased erosion, and changes to aquatic habitats (Ran et al. 2023, Gao & Coon 2022, Kokelj et al. 2021, Chalov & Prokopenko 2022, Alexander et al. 2020, Forbes et al. 2022). These impacts can have significant consequences for local water resources, infrastructure, and communities that rely on water for various purposes, such as drinking water, agriculture, and transportation (Li et al. 2022, Varlamov et al. 2022, Rolph et al. 2022, Lavrillier & Gabyshev 2021, Lytkin et al. 2021).

Permafrost supports unique and fragile ecosystems that are adapted to the extreme cold and limited growing seasons. Permafrost degradation can result in changes to vegetation composition,

shifts in wildlife habitat, and alterations in ecosystem functions and services (Yun et al. 2023, Che et al. 2023, Webb et al. 2022, Dearborn et al. 2021). These changes can have cascading effects on biodiversity, food webs, and ecosystem stability (Mętrak et al. 2023, Monteux et al. 2022, Wang et al. 2022), with potential repercussions for local livelihoods, traditional subsistence practices, and cultural heritage (Gibson et al. 2021, Brubaker et al. 2011, Nicu et al. 2021, Hollesen et al. 2017, Nicu et al. 2022).

In conclusion, permafrost is a critical component of cold region environments, with important implications for global climate, hydrology, and ecosystems. Thawing and melting of permafrost can cause subsidence and changes in hydrology and ecosystems. However, permafrost is highly vulnerable to climate change, and its degradation can have far-reaching environmental, social, and economic impacts. Research is ongoing to better understand the complex dynamics of permafrost and its interactions with the changing climate, as well as to develop strategies for mitigating and adapting to permafrost degradation. Effective management of permafrost requires interdisciplinary approaches that integrate scientific knowledge, engineering approaches, traditional knowledge, and community engagement to ensure sustainable and resilient solutions for both local communities and the global environment.

Degradational aspects in permafrost infrastructure regions refer to the challenges and issues that arise due to the thawing of permafrost in areas where human-made structures, such as buildings, roads, pipelines, and other infrastructure, have been built. Permafrost thaw can have significant impacts on the stability and functionality of infrastructure in these regions. That includes thaw settlement, subsidence, erosion, permafrost degradation under structures, infrastructure damage, increased maintenance costs, disruption of transportation and environmental impacts. Addressing these aspects requires careful planning, engineering, and adaptation strategies. In my thesis, I focus on roads and its degradation underneath. It is also partly connected to subsidence, infrastructure damage and maintenance. My research question centers on the influence of different parameters, such as excess ice, albedo or snow distribution, on the thermal regime of the ground and the permafrost degradation.

## 1.2 Road construction in permafrost regions

Infrastructure faces challenges due to ice bearing permafrost and seasonal freeze thaw cycles. The degradation of permafrost can destabilise the surface, posing various challenges for road constructions in the Arctic. However, in regions with permafrost or seasonal frost, special attention must be paid to them. Measures and solutions should be found to ensure stability over time while protecting the underlying permafrost.

### 1.2.1 Challenges

Some challenges that roads face in permafrost regions are described in more detail below. The selected main challenges are: thawing of permafrost, drainage, peat and damages of roads.

#### **Excess ice and thawing of permafrost**

Warming and thawing of permafrost is a known effect when it comes to road construction in the Arctic and is related to damages, stability problems and natural hazards (Fortier et al. 2011, Parent et al. 2019, Kong & Doré 2021, Hjort et al. 2022). From one-third to more than 50 % of fundamental

circumpolar infrastructure is at risk by mid-century (Hjort et al. 2022).

Excess ice is defined as the volume of ice in the ground that exceeds the total pore volume that the ground would have under natural unfrozen conditions (National Snow and Ice Data Center 2023a). Permafrost typically contains ice-rich elements such as ice wedges or ice masses of limited extent, which are often crossed by roads (Andersland & Ladanyi 2004). Road construction affects the existing thermal regime of the soil and alters the heat exchange at the surface, leading to heat accumulation and thus degradation of the permafrost and melting of the ground ice. This results in differential settlements and hence safety issues and a tendency to longitudinal and thermal cracking (more in paragraph 1.2.1). If there is locally massive ice, "sinkholes" may occur in the pavement (Andersland & Ladanyi 2004).

According to Andersland & Ladanyi (2004) the ideal embankment is thick enough and built with a non-frost susceptible soil to serve as an insulator for the permafrost beneath. In cold permafrost regions with a mean annual ground temperature (MAGT) of  $-11^{\circ}\text{C}$  a gravel embankment should be 1.5 m thick to keep the thawing only within the embankment (Andersland & Ladanyi 2004). When it is very ice-rich permafrost, the thawing would influence the settlement and hence stability significantly. To prevent thawing next to roads, ditches should not be excavated (Lin et al. 2011).

### Drainage

Drainage is a severe issue and can cause stability and bearing capacity problems (Villumsen et al. 2007). When the moisture content increases (partly caused by climate change) in the embankment the strength will be weakened. With permafrost underneath, the drained water contributes to advection and heat transport effects, which can affect the ground thermal regime. If an embankment cuts off the natural groundwater or surface water flow during the melting season, water can accumulate and create ponds at the toe or next to the road (Connor et al. 2020). This process increases the thawing of permafrost and leads to (differential) subsidence, which can cause damage. If poor drainage occurs and the water drainage regime is changed, thawed bulbs can form under or around the embankment or ponds are created (Wang et al. 2017). Therefore, those thawed bulbs increase the transport of heat, which leads to locally uneven thawing of permafrost.

Additionally, a new drainage can be created during construction (Connor et al. 2020). The embankment itself can lead to warming of the soil beneath. In regions with high ice content, this can melt the ice, induce a water flow and transport sediments, which will end in subsidence, weakening and damage (Connor et al. 2020, Doré 2004, Zeinali et al. 2016).

### Peat

Peat can cause problems with the stability and bearing capacity of embankments, as it often stores a lot of water that cannot be drained away in such quantity (Bigum and Steenfos 1984). If the road is built on a peat layer the load of the road pushes the water out of the peat, which is why settlements can occur. Ditches would additionally drain the peat layer and thus increase the erosion of the road (Bigum and Steenfos 1984). The excavation of peat is often not actionable, cost-effective or sustainable and only worth for large road projects like high speed national roads (Villumsen et al. 2007). In general, excavation of peat should be avoided due to its important role in climate and for conservation reasons, as 80 % of the world's peatland has already been destroyed (IUCN 2021). For lower classes of roads, more cost-effective and site-specific solutions can be used, like rehabilitation

projects of roads floating on peat or as insulation for the permafrost beneath (Villumsen et al. 2007, Bigum and Steenfos 1984).

### Damages

Roads in a seasonal or permanently frozen setting are facing several problems. Approximately 30 % of total road length in permafrost areas are affected by embankment damages due to underlying permafrost degradation (Chai et al. 2018). A common phenomenon is rutting of the pavement, which is favored by the use of studded tires, heavy vehicles and low speed. This mainly affects road safety due to aquaplaning and a slippery road surface due to remaining snow during winter maintenance.

Another major damage scenario is unevenness in the longitudinal direction of the road. This is mostly caused by thaw settlements (85 %) or frost heave (15 %) (Chai et al. 2018, Wang et al. 2009). Since roads are usually built along many kilometers with similar properties of the structure and asphalt, but the conditions of the underlying soil can change, differential settlement results. Ice-rich sections exhibit larger settlements. The weight of the road structure itself may lead to additional settlement over time due to the consolidation of the predominantly fine-grained soil.

A type of damage that occurs in many different forms is cracking (Figure 4). Cracks usually develop at low temperatures because the asphalt is then stiffer and more brittle. When temperatures drop rapidly, cracks appear across the entire road at regular intervals to relieve the stresses that occur. They can likewise form more frequently during spring thaw, as the asphalt is much weaker (Doré 2004, Zeinali et al. 2016). Another possibility is that cracks develop in the center of the road, which is caused by frost heave. In winter, snow is removed, allowing frost to penetrate the road more easily than on the shoulders, which are insulated by snow. In addition, cracking can occur on the side of the road, usually caused by heavy vehicles that are forced to drive close to the edge due to narrow roads and thus the load cannot be distributed well. Thaw consolidation within the roadbed soil under the embankment causes longitudinal and road shoulder cracks (Figure 4) (Chai et al. 2018, Wang et al. 2009, Wang 2017). Shoulder rotation occurs when the snow cover insulates the area next to the road (Figure 4) and thus keep the ground at warmer temperatures compared to the surrounding terrain. The permafrost table tilts and forces the shoulder to rotate and crack. Fatigue cracking is problematic as well, as it allows water to penetrate and cause further damage.

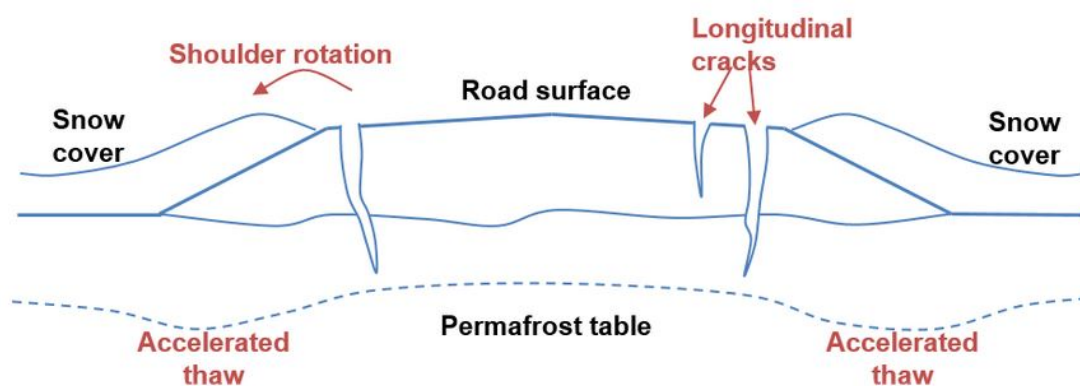


Figure 4: Selected damages of a road cross section in permafrost environment (Ingeman-Nielsen 2022)

### 1.2.2 Solutions

To avoid or prevent possible damage, there are some approaches that are used especially in regions with permafrost. A distinction is made between active and passive methods (Andersland & Ladanyi 2004). Both methods aim to keep the structure in a frozen state throughout its lifetime, with passive methods requiring no energy and active methods such as artificial cooling consuming energy to maintain or cool the thermal regime. Passive methods maintain the existing ground thermal regime whereas active methods accept changes (e.g. cooling). With regard to drainage, the natural flow path should not be blocked, but kept clear with bridges or culverts.

The design guidelines from Grønlands Hjemmestyre & Rambøll (2008), Andersland & Ladanyi (2004), Esch (1996) recommend practices to avoid permafrost degradation. Thermal protection should be provided to limit thaw penetration (Andersland & Ladanyi 2004). A layer of gravel of sufficient thickness is ideally used to isolate the in-situ frozen ground. In areas with massive ground ice, the road should be designed with a thicker layer of gravel and ditches should be avoided (Andersland & Ladanyi 2004). Esch (1996) makes several suggestions to minimise problems associated with ice-rich permafrost. These include reflective surfaces, insulation and embankments, and other measures to counteract the insulating effect of snow. There are several options for introducing cold air into the embankment in winter (Andersland & Ladanyi 2004).

A first measure is the appropriate choice of materials, whereby these should be frost-resistant and rather coarse according to Schaible's criterion<sup>1</sup> (Villumsen et al. 2007). It is also possible to choose the grain size and shape to ensure airflow. Furthermore, there is the possibility to use Air Convection Embankments (ACE), heat drains (Jørgensen et al. 2008), air convection culverts (Connor et al. 2020, Malenfant-Lepage et al. 2012), snow/sun sheds or light coloured aggregates (Malenfant-Lepage et al. 2012) to cool the embankment. A further measure is the use of an insulating layer in the road structure to reduce the amount of subbase material (Andersland & Ladanyi 2004). In addition, geotextiles can be used to reinforce the embankment and thus minimize differential settlement, cracking and shoulder rotation, or as a separator of different materials to ensure drainage (Connor et al. 2020). Finally, thermo-syphons can be used, which contain a gas and extract heat from the soil like a refrigeration system (Connor et al. 2020).

### 1.2.3 Thermal modeling through and under embankments

Information about the permafrost underneath transportation infrastructure is very valuable. A Canadian test site provides long-term thermal response for such a scenario to examine the disturbance on permafrost induced by the construction and climate change (Kong et al. 2018). Temperature data is used to calibrate the thermal model and gives information about the sensitivity of the ground thermal regime. For a better accuracy input parameters such as near surface air temperature, soil properties and embankment dimensions are used.

The study of Schneider von Deimling et al. (2021) investigates the thermal regime and permafrost degradation under climate warming beneath a road with embankment in Alaska by using the laterally coupled one dimensional heat conduction model CryoGrid3. Their study served as a basis for me and I first reproduce the results for the Dalton Highway in the CryoGrid community

---

<sup>1</sup>Method to assess the frost-risk of material by comparing it's grain size distribution with Schaible's boundary sieving-curves divided into three areas: frost dangerous, frost susceptible and frost safe (Villumsen et al. 2007)

model (see Appendix A). The study of Schneider von Deimling et al. (2021) focusses on ice-rich grounds and its melting of excess ice and following subsidence. A prediction about the time frame when failure might occur is given, wherein the design of the road plays a major role. Built infrastructure on permafrost significantly influences the ground thermal regime. Within 30 years – which is a typical lifespan of those structures – the predicted permafrost thaw would negatively affect serviceability (Schneider von Deimling et al. 2021). During winter snow usually accumulates at the shoulders and toes of the embankment (O’Neill & Burn 2017), which leads to the insulation of these area and accordingly cannot be cooled by the cold air. Furthermore, the plowing of snow causes cooling of the surface and subsurface. Embankments can also have a damming effect, which results in ponding next to the infrastructure.

In addition, there is a relatively new modelling study by Chen et al. (2023) on the railway embankment on the Tibetan Plateau, which also investigates the thermal conditions of embankments under various influencing factors, such as time of the year, sunny and shady side as well as distance to the center.

## 2 Methods

As described in the previous section, my thesis is about a road as a small scale feature. However, climate data are of much larger scale, which is why I address the challenges of different model scales. Furthermore, I describe the background to the climate forcing data used for reanalysis and projection. I briefly discuss the ground thermal regime with observational data, which was used primarily as input to the model via borehole thermistor data and iButton sensors for validation. Afterwards I describe the structure of the CryoGrid community model with focus on the configuration I used and an overview of the classes I applied. Finally, I describe how I handle possible bias in the initialization of the model.

### 2.1 Model scales and challenges

For the different influencing parameters, different temporal and spacial scales are common (Figure 5). Accordingly, climate and its changes are rather considered on a long-term scale (about 100 years) and infrastructure life time on a shorter time scale of about 30 years. In terms of spatial scales, global climate change tends to be applied on a large scale to the Arctic or to grid cells of several kilometers, whereas infrastructure is applied on a scale of a few meters.

Geotechnical models (GTMs) are used for engineering tasks when specific conditions should be met and complex processes are described mainly on fine scales (Schneider von Deimling et al. 2021). Those models are very good for simulating the construction phases, but can only map long-term effects to a limited amount. The input of exact boundary conditions is necessary to get reliable results. GTMs often do not take the insulating effect of snow into account, which is important for permafrost modeling (Schneider von Deimling et al. 2021).

For more complex problems, thermo-hydro-mechanical (THM) models are used to couple the three components: thermal, hydrological and mechanical properties. A THM is typically implemented in a software like Plaxis or GeoStudio. Its advantage is the ability to couple processes and obtain information about stability, deformation and failure. The challenge of THM models is, that they have high computational costs limiting the use for long-term climate-warming models or parameter testing (Schneider von Deimling et al. 2021). Furthermore, the models are limited to a small scale.

To project future climate change Earth system models (ESMs) are used

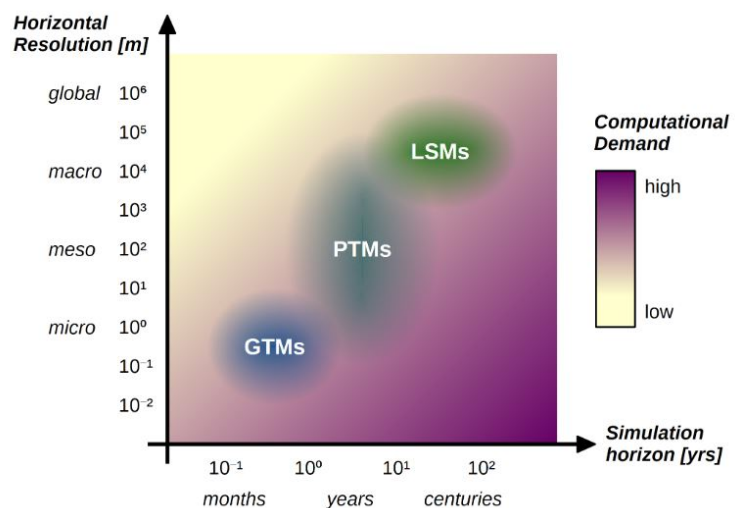


Figure 5: Classification of model classes with their temporal and spatial scale (Schneider von Deimling et al. 2021)

as a primary tool (Aas et al. 2019). ESMs simulate globally averaged land carbon sinks within the range of observation-based estimates with a high confidence (Pörtner et al. 2022). A globally fitted model often masks large regional disagreements, especially in permafrost landscapes where melting of ground ice and ensuing subsidence impact the lateral processes. These changes can significantly alter soil conditions and lead to fluxes of heat, water, and carbon to the atmosphere (Aas et al. 2019).

With a changing topography on smaller scales and related fluxes of heat, and water a two-tile model approach is possible. For different ice-rich ground dominated permafrost landscapes these two-tile simulations give a realistic response (Aas et al. 2019). In general, lateral fluxes and changing microtopography have a strong impact on simulated permafrost conditions in the current state and for future projections. In several studies it was demonstrated that laterally coupled tiles from existing methods enable a simple and effective first-order representation for observed degradation processes in ice-rich permafrost regions (Aas et al. 2019, Nitzbon et al. 2019).

Furthermore, Land surface models (LSMs) as a component of ESMs simulate the exchange of water and energy fluxes with quantitative methods at the interface of atmosphere and Earth surface. LSMs are important tools to investigate the sensitivity of the terrestrial Cryosphere under complex environmental and climatic conditions (Westermann et al. 2023). LSMs are able to project climate change impact. Within the last decade, LSMs improved a lot with regards to permafrost changes and degradation (Schneider von Deimling et al. 2021). The focus of the developments is on the description of physical thaw processes and biogeochemical cycles of soil carbon release, but does not include impacts on infrastructure (Schneider von Deimling et al. 2021). In several studies LSMs predict large-scale degradation of near-surface permafrost within the next 80 years (Lawrence et al. 2008, 2012, McGuire et al. 2018). But LSMs are very simplistic with only one dimension to simulate top-down thawing. They disregard lateral processes (e.g. snow redistribution, soil erosion, water flow,...), which are common in many permafrost regions. The spatial grid of LSMs is very coarse with a horizontal resolution of approximately 100 km (Schneider von Deimling et al. 2021). That is why it is not practical to use LSMs for permafrost related small-scale problems.

Additionally, Process-based tiling models (PTMs) combine the detailed, small-scale GTMs and the long-term, large-scale LSMs to model interaction between climate warming, permafrost degradation and infrastructure (Schneider von Deimling et al. 2021). Those models are reduced in complexity while keeping the most important processes related to infrastructure-affected permafrost thaw. In contrast to LSMs lateral interactions between individual tiles are considered. In addition, it has a much faster time integration due to a reduced order representation compared to GTMs. Therefore, they reach the same spin-up, long-term simulation and uncertainties. The PTMs have a high vertical resolution, which allows them to solve time-sensitive problems and complex problems on a scale not comparable with GTMs (Schneider von Deimling et al. 2021). PTMs have a modular structure and are scalable to a particular problem. In my thesis I use a PTM, more precisely the CryoGrid community model, which links small-scale GTMs and large-scale LSMs. CryoGrid is a 1D heat-diffusion model, developed using the PTMs background. It has been used already successfully in several studies related to permafrost processes of taliks (Langer et al. 2016), thermokarst (Westermann et al. 2016, Martin et al. 2021, Nitzbon et al. 2021) or ice-wedge polygons (Nitzbon et al. 2019, 2020).

## 2.2 Climate

Freezing and thawing indices are used to estimate whether cold or warm a site is and how it develops over time. They can be calculated based on the temperature records. For this purpose, I used the daily mean value of the temperature over one year, with February 29th being ignored in leap years. Those indices can be described with integrals of the temperature over the time  $t$  [days]. Due to the fact that the daily average temperature is used, it can be simplified with a sum. I added up all negative temperatures  $T_n$  of all days of a year for the freezing index  $I_f$  and all positive temperatures  $T_p$  for the thawing index  $I_t$ . Equation 1 explains the calculation of the indices, where  $\theta$  denotes the duration of freezing or thawing in days.

$$\begin{aligned} \text{Freezing index : } I_f &= \int_0^\theta T_n dt = \sum_0^\theta T_n \Delta t = \sum_0^\theta T_n \\ \text{Thawing index : } I_t &= \int_0^\theta T_p dt = \sum_0^\theta T_p \Delta t = \sum_0^\theta T_p \end{aligned} \tag{1}$$

## 2.3 Forcing data

Climate projections for the 21st century indicate a pronounced warming and permafrost degradation in the Arctic and sub-arctic regions (Jafarov et al. 2012, Pörtner et al. 2022). Models need input data that gives information about the climatic and meteorological conditions of the selected location. This input data can be observations from weather stations or climatic reanalyses and projections. Climate forcing data provides continuous information about the way volcanic eruptions, solar variability, trace gases and aerosols, Milankovitch orbital variations and other factors can affect the climate (National Centers for Environmental Information (NCEI) 2022). These parameters change the way how energy is distributed in the atmosphere and therefore contributing to climatic cooling or warming. Volcanic eruptions tend to cool the climate because the particles partly reflect the incoming solar radiation. Greenhouse gases on the other hand have the opposite effect and warm the climate. Furthermore, the intensity of incoming radiation varies due to changing orbits and solar intensity itself (National Centers for Environmental Information (NCEI) 2022). In this work, I use reanalysis data as historical data. For projections into the future until 2100, I apply the Max-Planck Institute - Earth System Model (MPI-ESM) with the most drastic representative concentration pathways (RCP) scenario. I furthermore discuss the Norwegian Earth System Model (NorESM).

### 2.3.1 Reanalysis data

The European Centre for Medium-Range Weather Forecasts (ECMWF) provides a series of ECMWF reanalysis (ERA) data sets. For my thesis, I use the fifth generation ECMWF atmospheric reanalysis (ERA5) reanalysis data set. It covers a period from January 1950 to present and is produced by the Copernicus Climate Change Service (C3S) at ECMWF (ECMWF 2022a). ERA5 provides hourly estimates of a large number of atmospheric, land and oceanic climate variables (ECMWF 2022b). Each grid has a size of 30 km and resolves the atmosphere by using 137 levels from the surface up to 80 km of height. Information about uncertainties are given in the data as well (ECMWF 2022b). The ERA5 data is available on single levels, 37 pressure levels, 16 potential

temperature levels, one potential vorticity level and 137 model levels (ECMWF 2022a). Furthermore, there are daily and monthly aggregates of the hourly field available. I use the data provided on a daily basis. Quality-assured monthly updates of ERA5 (1959 to present) are published within three months of real time and preliminary daily updates of the data set are available to users within five days of real time (ECMWF 2022b). ERA5 combines the enormous amount of historical observations (satellite and in-situ) into global estimates by using advanced modelling and data assimilation systems (ECMWF 2022a).

The ERA5 data can be downloaded from C3S with a web interface<sup>2</sup> or a Python-based application to get the Network Common Data Format (netCDF) files. This is prepared by Thomas Ingeman-Nielsen because the download process is very time consuming. I process the netCDF-files to get the forcing data in a format that is used by the Matlab based CryoGrid community model (see paragraph 2.5.1). I first extract the individual variables and then perform the downscaling algorithm. To check if the forcing data is applicable to the region of interest, I plot the variables to make a first order estimate to see whether the amplitudes and annual cycles match the observations from the weather station (Haagmans 2021). The forcing variables, which do not match with the observations, need to be bias-corrected.

### 2.3.2 Projection models

In 2008, the Working Group on Coupled Modelling (WGCM) of the World Climate Research Programme (WCRP) produced a protocol for Coupled Model Intercomparison Project (CMIP) Phase 5, which summarises 35 climate model experiments from 20 climate modelling groups (Taylor et al. 2012). These models are utilized, among other things, to investigate mechanisms for differences due to feedbacks with the carbon cycle and clouds (PCMDI 2023). In addition, the predictability of climate from models are investigated, as well as the reasons why similar models produce a range of results (PCMDI 2023). The results from the international climate model comparison project CMIP serve as a basis for the Intergovernmental Panel on Climate Change (IPCC) reports. By now, the newer updated version CMIP Phase 6 is publicly available, which has a higher spatial grid resolution (Martel et al. 2022). All climate models with their different scenarios can be downloaded from the Copernicus repository. For my thesis, I download the MPI-ESM and NorESM. Depending on the model, daily or monthly data for single level and pressure level of different variables (2m temperature, 10m wind speed, near-surface specific humidity, geopotential height, etc.) are available. I download all available parameters for each model. In addition, the models in CMIP5 provide the RCP scenarios 2.6, 4.5, 6.0 and 8.5, which estimate the climate of the future based on an increase in the volume of greenhouse gases. The number represents the expected radiative forcing in 2100 (2.6 W m<sup>-2</sup>, 4.5 W m<sup>-2</sup> etc.). For more recent models of CMIP6, the Shared Socioeconomic Pathways (SSP) scenarios 1-1.9, 1-2.6, 2-3.4, 5-3.4, 2-4.5, 4-6.0, 3-7.0 and 5-8.5 are used. In my thesis I use the SSP5-8.5 scenario. They are based on the RCP with a stronger focus on global societal, demographic and economic changes (Riahi et al. 2017).

MPI-ESM is a model developed by the Max Planck Institute for Meteorology in Germany, which is provided for CMIP6 in low (LR) and high resolution (HR). MPI-ESM is also available for earlier CMIP phases, but I focus on CMIP6 here, which I use for my forcing data set. The models are released in 2017 and include the following components: aerosol, atmosphere, land, hydrology,

---

<sup>2</sup><https://cds.climate.copernicus.eu/cdsapp#!/dataset/reanalysis-era5-single-levels> and <https://cds.climate.copernicus.eu/cdsapp#!/dataset/reanalysis-era5-pressure-levels>

dynamic vegetation, land ice, ocean dynamics, ocean biogeochemistry and sea ice with resolutions between 50 km and 100 km (HR) and 250 km (LR) (Fiedler et al. 2019, Schupfner et al. 2019). For daily data, the HR model provides only historical data, whereas the LR model provides air temperature, specific humidity, pressure, wind speed and precipitation for the projection scenarios SSP1-2.6, SSP2-4.5, SSP3-7.0 and SSP5-8.5 (Copernicus Climate Change Service 2021). For monthly data, significantly more parameters and pressure levels can be selected. I download the projection for MPI-ESM1-2-LR raw data up to 2100 for my thesis from Copernicus and use SSP5-8.5.

Another model introduced with CMIP5 is the NorESM1 (medium resolution) described by Bentsen et al. (2013) (Taylor et al. 2012). The NorESM2 model, which has been extended for CMIP6, is described in more detail by Seland et al. (2020) with new developments from Guo et al. (2019). The model is divided into the components atmosphere, sea, sea ice, land with vegetation, etc. and includes interaction with atmosphere chemistry and biogeochemical cycles (NorESM 2016). The development has been taking place since 2007. I discuss the comparison of available parameters and scenarios to MPI-ESM (Copernicus Climate Change Service 2021). For Greenland, NorESM is known in other contexts to give good results compared to observations (Bezeau et al. 2015, Plach et al. 2018). I download the data for NorESM1 from Copernicus `pressure level` and Copernicus `single level` via CMIP5. For NorESM2, however, only surface level data is available. As downscaling with TopoSCALE (see below) would therefore not be feasible with NorESM2, I use CMIP5 instead.

### 2.3.3 Connection and downscaling algorithm

I combine the reanalysis data from ERA5 and the MPI-ESM projections following a two-step approach developed and performed by Alexander Oehme at AWI. First, a reference period is defined for which both models (ERA5 and projection MPI-ESM) have data. For this overlap, the anomalies of the projections are considered and applied to the ERA5 forcing data. Depending on the length of the reference period, this results in a periodicity for the future projections. By using only the anomalies and not the values themselves, it is ensured that there is no gap between the reanalysis data and the projections. If the reanalysis period shows only small anomalies, however, I applied these also for the future.

The grid cells of the reanalysis data as well as the forcing are generally not very dense and usually not at the location the user is interested in. A downscaling to the point of interest is therefore needed. One option is the realisation of downscaling using the distance of the grid points to the point of interest (POI). I determine the number of points to be included based on the distance to the POI. The distances are weighted differently, the closer they are to the POI, the greater their weight, and the further away, the less their influence. I then interpolate the values of the grid cells according to the weighting. Possible topographical differences do not play a role. This procedure is provided by Alexander Oehme (AWI).

Alternatively, the algorithm TopoSCALE from Fiddes & Gruber (2014) is used for downscaling. TopoSCALE is optimised for difficult, hilly and remote terrain. Climate models usually have a high vertical resolution of the atmospheric column with pressure level data between 1 and 1000 hPa (ECMWF 2023). Furthermore, a well resolved digital elevation model (DEM) is required to perform the downscaling algorithm. I used the Copernicus GLO-30 Digital Elevation Model from OpenTopography with a resolution of 30 m. Based on this, the coarse-grid climate variables were

subdivided to a finer scale (Fiddes & Gruber 2014). In TopoSCALE, I interpolate the pressure level data according to their topographic height. The short-wave radiation is provided with an elevation and topography correction. For long-wave radiation, however, the cloud component of the emissivity is used in the TopoSCALE algorithm, as well as temperature and relative humidity. Precipitation is decomposed with a simple non-linear lapse and optionally with a climatology approach (Fiddes & Gruber 2014). The TopoSCALE approach has already been successfully applied to complex terrain in the Alps with good results, so I applying it to Ilulissat in West Greenland. The coding base is provided to me by Thomas Ingeman-Nielsen (DTU).

## 2.4 Ground thermal regime

There are several ways to investigate the ground thermal regime using measured and non-modelled data. On the one hand, boreholes can be created and their soil analysed over the depth. Then, it becomes accessible to equip these boreholes with a thermistor string, facilitating the recording of temperatures. Secondly, iButton sensors can be installed to record near-surface temperatures.

### 2.4.1 Boreholes

In permafrost regions, it has been a common practice for many decades to establish boreholes in order to test the soil for specific parameters in the laboratory. These include bulk density, grain density, water content, void ratio, porosity, ice saturation and loss on ignition for organic matter (Scheer & Ingeman-Nielsen 2022). Furthermore, salinity and grain size distribution can be determined. For some of these investigations it is necessary that the core is stored or transported in a frozen state in order to be examined in the laboratory afterwards. The cores provide information on the stratigraphy of the soil and the properties of the individual layers. In the context of my thesis, the soil type with the corresponding depth as well as the presence and depth of possible ice lenses and excess ice layer are of particular interest.

Once the borehole has been drilled, it can be equipped with a thermistor (thermal + resistor) string to measure temperatures over depth. The sensor changes resistance depending on the temperature. This is converted to temperatures using a calibration cable (beadedstream inc. 2022). The thermistors are installed on a cable with a certain distance between them. The temperature sensors are closer together near the surface (10 cm to 25 cm), because greater fluctuations are to be expected there due to the influence of the air temperature. At depth, the fluctuations become smaller, so that the sensors can be spaced further apart (50 cm to 2 m). The thermistor string is installed in a hollow tube which is inserted into the borehole and surrounded by a filling material (grout or sand) (Noetzli et al. 2021). The tube can either not be filled and air convection is neglected due to the narrow diameter and small temperature gradients (Zotikov 1986, Haerberli & Funk 1991) or it can be filled with a compensating liquid. Nowadays it is common for such thermistor strings to record the data and be read out from time to time, whereas in the past it was necessary to visit the borehole and measure the temperatures on site. I use the DTU borehole temperature data to generate trumpet plots, that are based on monthly maximum, mean and minimum temperatures (see Figure 2).

### 2.4.2 iButtons

For ground surface temperatures, iButton sensors are used, which are installed on the surface and automatically record the temperatures. Before the sensors are installed, they must be calibrated

in the laboratory (Scheer 2020). After the appropriate location has been chosen, the surface must be prepared and cleaned a little to place the sensor. Surface temperatures with different distances to the road are of particular interest for my thesis. To get the logged data, the user has to come back at a later time to retrieve and read it. To make the iButtons easier to find, coloured wires can be attached (Scheer 2020). The whole process of calibration, choice of location, installation and retrieval is done by Johanna Scheer from DTU. The iButton sensors used, model DS1922L, have a temperature range of  $-40^{\circ}\text{C}$  to  $85^{\circ}\text{C}$  with an accuracy of  $\pm 0.5^{\circ}\text{C}$  in the range of  $-10^{\circ}\text{C}$  to  $65^{\circ}\text{C}$  and a user-defined logging rate of 1 s to 273 h and are resistant to dirt and moisture (iButtonLink 2023).

The processing of the ground surface temperature data starts with a calibration process for each iButton sensor according to Ingeman-Nielsen (2016), where the calibration value is added to the measured temperature of the sensor. It is then possible to plot the temperature comparatively over time.

## 2.5 CryoGrid community model

The newest version of the CryoGrid family is the CryoGrid community model, which should combine the functionalities of CryoGrid 1 to 3 and go beyond their limitations. The whole section is based on the preprint Westermann et al. (2022) and the final version Westermann et al. (2023) and describes the mode of operation of the model and its functionality. For the numerical modeling of the road as well as the surrounding tundra described below (subsection 3.4), I use the CryoGrid community model, which is suitable due to its modular structure and functional representation of the processes in the permafrost. This has already been confirmed for a similar setup in Alaska with CryoGrid 3 (Schneider von Deimling et al. 2021). My comparison between CryoGrid 3 by Schneider von Deimling et al. (2021) and the community model for the setup on the Dalton Highway can be seen in Appendix A.

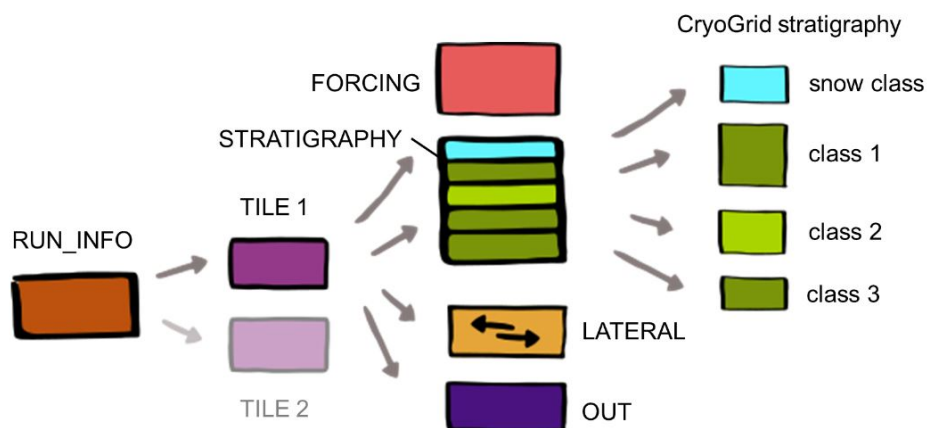


Figure 6: Hierarchy of the types of CryoGrid classes required for multi-physics simulations within the CryoGrid community model (Westermann et al. 2023)

The CryoGrid community model is modular structured (Figure 6) with different functionalities. I combined several modules to build up the model. The model is a flexible toolbox to simulate the

ground thermal regime as well as the ice/water balance for permafrost and glaciers. By using fully modular structures through object-oriented programming it can be applied to many scenarios. The model is implemented in the programming language Matlab. Each object/class contains variables and functions which can modify those and point to other classes in a tree-like structure (Figure 6). The best-fitting class-type including their parameters needs to be selected by the user depending on the use. My specific setup is explained later in this section. RUN\_INFO is the only mandatory class type. The class type TILE in the second level (Figure 6) performs a one-dimensional simulation like CryoGrid 2 and 3. RUN\_INFO organizes the simulation and selects how many TILES are launched including their execution modes. I implement most of my model runs with five TILES. Hierarchy level 3 employs specialized class types, which control different aspects of the simulation (state variables, forcing and output classes). Different FORCING classes are available to provide the required model forcing (see subsection 2.3) at a specific time step. OUT classes decide which kind of data and how the output is stored. The STRATIGRAPHY classes calculate depth profiles of different model variables to determine the initial state. LATERAL controls lateral interactions with the external environment. The classes I use are explained in more detail in subsection 2.5.1.

Different stratigraphy classes with their specific model physics and state variables are stacked vertically to realize a one-dimensional model simulation (Figure 7). The boundary conditions are applied to the upper- and lowermost classes and interaction classes compute fluxes across the boundaries between adjoining stratigraphy classes.

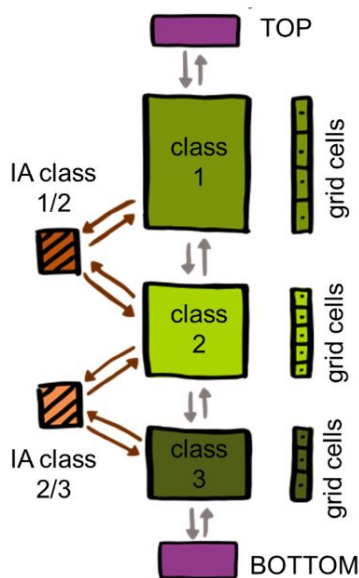


Figure 7: Example of a CryoGrid stratigraphy in a one-dimensional tile class with three stratigraphy classes coupled by interaction (IA) classes (Westermann et al. 2022)

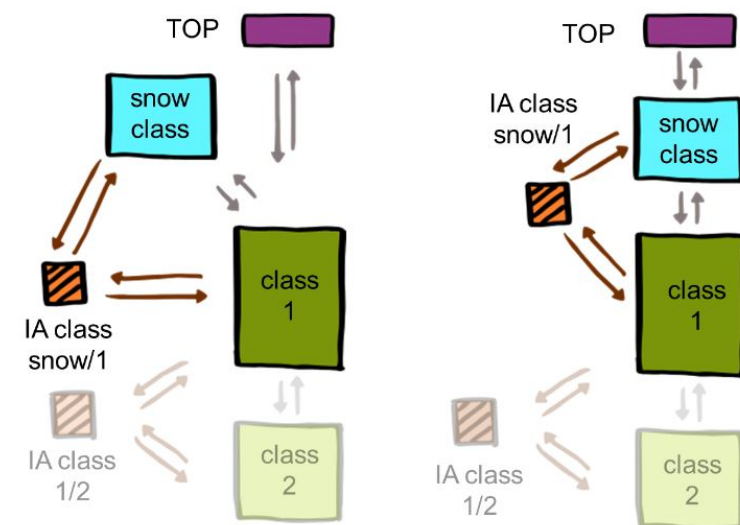


Figure 8: Schematic representation of the CryoGrid stratigraphy when a snow cover is present. Left: snow initially added as CHILD to the uppermost surface class and covers surface area only partially. Right: snow water equivalent exceeds user-defined threshold and snow class becomes uppermost class of regular stratigraphy. The process reverses when snow melts. (Westermann et al. 2022)

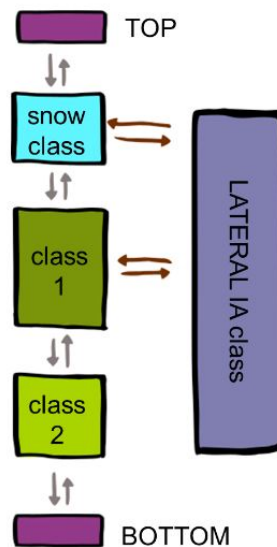


Figure 9: Schematic representation of the CryoGrid stratigraphy interacting with a lateral interaction (IA) class. (Westermann et al. 2023)

Another feature of the stratigraphy classes is the ability to modify and rearrange the stratigraphy itself if a certain condition is met. This can be the case for ponding or seasonal snow cover (Figure 8). When the user-defined threshold is reached the class will be inserted/removed automatically. This can in some cases be handled with a CHILD stage where the new class evolves as part of the uppermost stratigraphy class when the surface is only partially covered. This procedure is done to prevent numerical issues. When this is not a problem anymore the class is added as the uppermost one in the stratigraphy.

In the CryoGrid community model a standardized interface is used to implement a variety of lateral interactions (Figure 9). Lateral classes and lateral interaction classes can be selected. It can be chosen whether the stratigraphy should interact with external reservoirs or with another 1D stratigraphy, which corresponds to laterally coupled tiling. For external reservoirs, the lateral fluxes are added or subtracted after a fixed, user-determined interaction time step and should be small compared to vertical fluxes within the stratigraphy. For my model runs, there is lateral interaction between the adjacent tiles and only the outer tiles interact with the environment, e.g. through runoff water.

Regarding the thermal conditions, the initial temperature profile is often unknown in reality and must be estimated by a model spin-up. When the model runs for a certain time period, the temperature profile becomes independent of the initialization. In the CryoGrid community model there is the opportunity to accelerate the model spin-up by estimating the equilibrium temperature profile. For my case, I use the borehole temperature data and assume it to be the initial temperature profile including the geothermal heat flux. To avoid initialization bias, I apply the procedure described in subsection 2.6.

Concerning the lateral interactions there is a standardized way to implement a one-dimensional model column with its environment to account in some extent for the influence of topography. This

is important when water accumulates in or flows towards terrain depressions to simulate the soil moisture conditions. The lateral interaction class (Figure 9) realizes the inflow from external water or heat reservoirs as well as continuous drainage at slopes.

### 2.5.1 CryoGrid classes

#### FORCING classes

FORCING classes belong to the classes required in order to run the model. They serve to include the necessary model forcing for a certain time step. There are different FORCING classes available in CryoGrid, for example to easily interpolate the raw data or to reproject the radiative components based on slope and aspect. For forcing, the class FORCING\_seb\_mat is used, which uses the surface energy balance (SEB) and allows reading the data in a .mat file. The necessary parameters in the forcing data are: incoming shortwave and longwave radiation  $S_{in}$  and  $L_{in}$  [ $\text{W m}^{-2}$ ], precipitation  $P_s$  (solid) and  $P_l$  (liquid) [ $\text{mm d}^{-1}$ ], air pressure  $p$  [Pa], air temperature  $T_{air}$ , wind speed  $U$  [ $\text{m s}^{-1}$ ] and specific humidity  $q_{air}$  [ $\text{kg water vapor kg}^{-1}$  air] at height above ground  $h$  [m] as well as time stamp. The time must be equally spaced and really exact. The energy flux into the first grid cell  $F_{ub}$  can be determined by a constant temperature or, alternatively and more realistically, by the SEB, which is defined by the incoming and outgoing short and long wave radiation ( $S_{in}$ ,  $S_{out}$ ,  $L_{in}$  and  $L_{out}$ ) and the sensible and latent heat flux ( $Q_h$  and  $Q_e$ ) as a function of time  $t$  (see equation 2).

$$F_{ub}(t) = S_{in}(t) - S_{out}(t) + L_{in}(t) - L_{out}(t) - Q_h(t) - Q_e(t) \quad (2)$$

The model forcing I use is created by downscaling the ERA5 reanalysis data with projection of the model MPI-ESM with measured data as reference (see subsection 2.3).

#### STRATIGRAPHY classes

The stratigraphy of state variables (STRAT\_STATVAR) classes are used to calculate profiles over the depth for different parameters and thus the initial state of the model grid. Depending on the class in use, layers with constant values or interpolation of different values over the depth are utilized. The different defined classes are stacked vertically by means of TILE\_1D\_standard, with lateral interactions (paragraph 2.5.1) between the classes ensuring the exchange (Figure 7). Each class is defined by its specific model physics and state variables. Stratigraphy classes include ground columns with and without water balance, water bodies, glaciers and snow with different levels of process representation. Each class occupies a specific vertical domain via its grid cells with boundary conditions applied to the top and bottom class (Figure 10). Within each class, the evolution over time is calculated, such as ground temperature and water-ice content. In addition, prognostic state variables (time-derivative calculated and integrated) and diagnostic state variables (not time-integrated) are used.

An important property of stratigraphy classes is that they can be modified and rearranged in the course of the model if certain conditions are met. Classes can disappear or be created when, for example, ponds are formed and then dry up again. If water collects on previously dry ground, a water body class is created at a user-defined threshold. If the water level subsequently falls below the threshold again, the stratigraphy class disappears. In the case of seasonal snow cover, a snow class is also triggered and created. For very low snow depths, however, numerical issues arise due to small grid cells, which is why the snow class is introduced in steps (Figure 8). It is initially created in a CHILD environment and is thus not part of the stratigraphy, but develops as part

of the top stratigraphy class as a water equivalent in the vertical direction. This keeps the snow volume correct and as soon as the snow volume is large enough, the classes are rearranged and the snow class becomes part of the stratigraphy as an independent class (Figure 8). With snowmelt, this happens in reverse order.

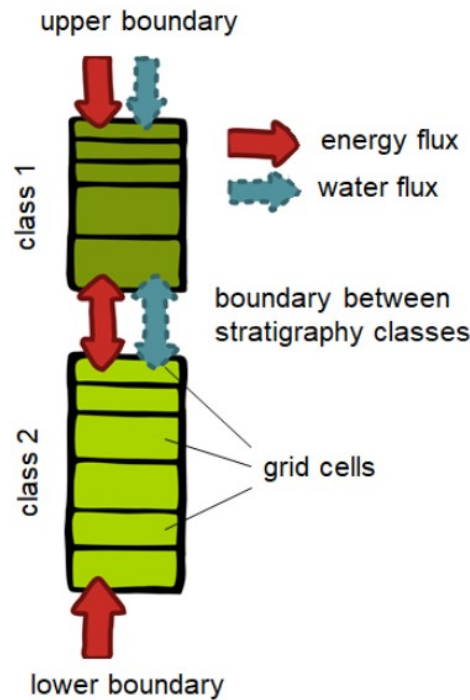


Figure 10: CryoGrid stratigraphy in the tile class `TILE_1D_standard` with two stratigraphy classes. Each stratigraphy class has its own state variables and model grid, and energy and water are exchanged between stratigraphy classes. At the upper boundary, energy and water are exchanged, while a heat flux is typically applied at the lower boundary. (Westermann et al. 2023)

For the simulations in this thesis, the ground classes `GROUND_freezeC_bucketW_Xice_seb_snow` and `GROUND_freeW_seb` are used. These classes describe the proportions of ground material consisting of mineral  $\theta_m$ , organic  $\theta_o$ , water  $\theta_w$ , ice  $\theta_i$  and air fraction  $\theta_a$ . The porosity of the respective layer is calculated with the following equation:  $\phi = 1 - \theta_m - \theta_o$ . For the realisation of seasonal snow, for each ground class there is an identical class with `CLASSNAME_snow`, which realises the CHILD processes. The class `GROUND_freeW_seb` contains the SEB with evapotranspiration, free water freezing characteristics and no flow water balance. This is applied to all deeper layers, i.e. depending on the composition of the tiles from 7 m depth or more. For this reason, no interaction with snow is required. The class `GROUND_freezeC_bucketW_Xice_seb_snow` is applied from the surface to the transition towards `GROUND_freeW_seb` and considers the CHILD environment for snow. In addition, the SEB is used with evapotranspiration, Painter & Karra (2014) freezing characteristics, excess ice representation, bucket scheme water balance with representation of standing surface water.

`LAKE_simple_bucketW_seb_snow` is used as the LAKE class for ponding. This applies SEB with evapotranspiration, free water characteristic, glacier mass balance scheme with surface melt-

water automatically removed. For snow, the class `SNOW_crocus2_bucketW_seb` is used, which utilises snow microphysics, SEB, bucket scheme snow hydrology. Meltwater is retained and allowed to pool up above the snow surface. The class is designed to be used with `GROUND_freezeC_bucketW_seb_Xice` to ensure the transfer of snowmelt.

### Interaction classes

In the lateral classes, lateral interactions with external environments/reservoirs are considered. The interaction classes determine fluxes between two stratigraphy classes across the boundaries (Figure 9). This ensures their compatibility. If both classes have different state variables in terms of time integration, the code must ensure the calculation of the correct fluxes. For example, if only one class is hydrologically active and the sum of water and ice is static for the other, a zero water flux boundary condition must be used. In the initialisation of the CryoGrid stratigraphy, the correct interaction class is automatically selected for the two adjacent stratigraphy classes.

In my simulation, the lateral coupling to a heat reservoir `LAT3D_HEAT` is used across all tiles. I use the lateral flow class `LAT3D_WATER_UNCONFINED_AQUIFER_OVERLAND_FLOW` for all tiles and `LAT3D_WATER_OVERLAND_FLOW` for the overland flow of the tundra tile at the "margin" of the simulation boundaries. Further interaction classes are `LAT_REMOVE_SURFACE_WATER` for surface water removal, `LAT_SEEPAGE_FACE_WATER` for the seepage face and `LAT_WATER_RESERVOIR` for the use of a water reservoir by an adjacent lake, river or pond.

### OUT classes

The OUT class determines which and how the results are stored. In the test and development phase, it makes sense to save many variables, whereas the user can only save variables that are of interest. Furthermore, the full model state can be saved after the simulation is finished in order to start a new simulation at the same state. For the simulation in my thesis I choose the class `OUT_all_lateral`, which stores the stratigraphy classes in a cell array for each timestep. This includes the raw model state with parameters and temporary variables as well as the variables of the lateral interaction classes. After the CryoGrid community model has been run, the user receives an annual OUT file, which provides information on the time stamp, the lateral interaction and the results according to the stratigraphy in the selected grid. This includes constants, selected parameters as well as the distribution of the shares over the depth per tile as well as results of the temperature course, water or ice distribution and numerous other results. I read them out with the help of a Matlab script to finally obtain the distribution over the depth with time.

## 2.6 Initialization bias

The result must reflect and inherit the error since simulations rely on assumptions rather than exact initial conditions. In the CryoGrid community model, one of the initial values is the temperature profile of the ground. This is difficult to estimate in general and especially at great depths, but is approximated by boreholes and temperature measurements there as well as the thermal gradient based on the geothermal heat flux  $Q_{geo}$ . Borehole data are assumed based on observations from thermistor strings at the beginning of the simulation in 1980 (more in subsection 3.2.1). I take the temperature profile from the new established boreholes because they have a finer spatial grid. That gives a rough estimate but does not represent the reality. To determine how large the deviations are and when the influence of the initialization bias is small enough, the simulated soil

temperatures are considered and evaluated using statistical methods. I discarded the first 20 years due to initialisation bias and conducted the following experiment to demonstrate that this period is sufficiently long and the error caused by initialisation is negligible. First, the forcing data set is adjusted so that for all parameters (air temperature, rainfall, snowfall, specific humidity, pressure, shortwave radiation, longwave radiation and wind) the values of the first year considered are repeated for 10 years. In case the first year is a leap year, the 29th of February is deleted in common years and if the first year is a common year, the values of the 28th of February are repeated for all future leap years. This adjusted forcing data set is used to ensure that temperature fluctuations come from the simulation and are not influenced by fluctuating input values. For any point in time during the year, the simulated soil temperature can be observed and compared to the same point in time in the following year. The signals oscillate around a mean value (see Figure 11) and if the variations are sufficiently small, I assumed that there is no or a very small influence of the initialization. To put this on a statistical base, the standard deviation for the temperatures at any time of the year is compared over several years. These should become very small and tend towards zero. For my thesis, I assumed a maximum standard deviation of  $0.1\text{ }^{\circ}\text{C}$ . For the evaluation of the simulation, only results that are not in the initialization period are finally considered.

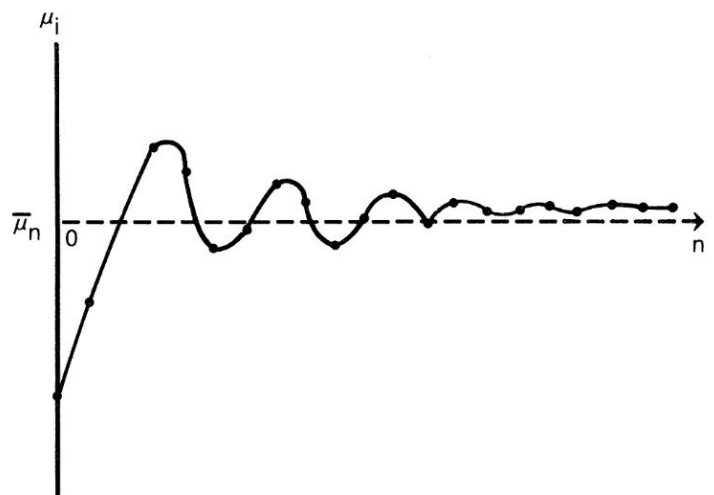


Figure 11: Example of a transient mean function due to initialization of a simulation program (Schruben 1982)

### 3 Case - Ilulissat, West Greenland

In my thesis I focus on Ilulissat, the third biggest town in Greenland (Figure 12). It is located at the west coast at approximately 69°13' N and 51°6' W and has about 4700 inhabitants (City population 2022). The city is located in the continuous permafrost zone. Permafrost and related freeze-thaw processes affects infrastructure in the area (Ingeman-Nielsen, Scheer & Tomašková 2022).

In the further course of the paper, I discuss the conditions of the ground thermal regime (subsection 3.2) and climate forcing (subsubsection 3.1.2 and subsection 5.1) in Ilulissat. Likewise, road construction in Greenland in general is considered and applied to Ilulissat (subsection 3.3 and subsection 3.4).



Figure 12: Map of the Ilulissat area with inserted small map of Greenland with selected place names. (Geological Survey of Denmark and Greenland (GEUS) 2022)

### 3.1 Climate

In this section, I provide insight into various parameters measured by the weather station in Ilulissat to better understand local conditions. In addition, I show the grid points of the different forcing data sets, which highlights the problem of using unrealistic data for the projections.

#### 3.1.1 Weather station

Looking at climate and weather data for the region around Ilulissat, there is a weather station in the city (since 1961) and another at the airport (since 1991). The data for temperature, humidity, air pressure, wind, precipitation, sunshine, drought index, lightning and maximum snow depth are partially incomplete provided by Danmarks Meteorologiske Institut (DMI) (DMI 2022c). In addition, the new report from 2022 has changed data in a new format back to 1991 for the full observation cycle at the airport (DMI 2022b). Using the new data from 1991 to 2021, I determined the temperature profile of a standard year (see Figure 13). Compared to the temperature records for a single year, some fluctuations have already been reduced. When viewed over a longer period of time, the curve smooths further and resembles a harmonic function. Using the temperature recordings over 30 years (1991-2020) from DMI, I set up a climate diagram which shows the monthly mean average temperature as well as the mean maximum and minimum temperature (see Figure 13). Continuous negative temperatures<sup>3</sup> are to be expected between October and April. May and September represent a transition period and positive temperatures can be assumed between June and August. As a result, permafrost occurs with an AL in the summertime. In addition, precipitation in the form of snow or hail must be expected. This is mainly important for maintenance of the roads and insulating effect and thus permafrost thaw or ponding.

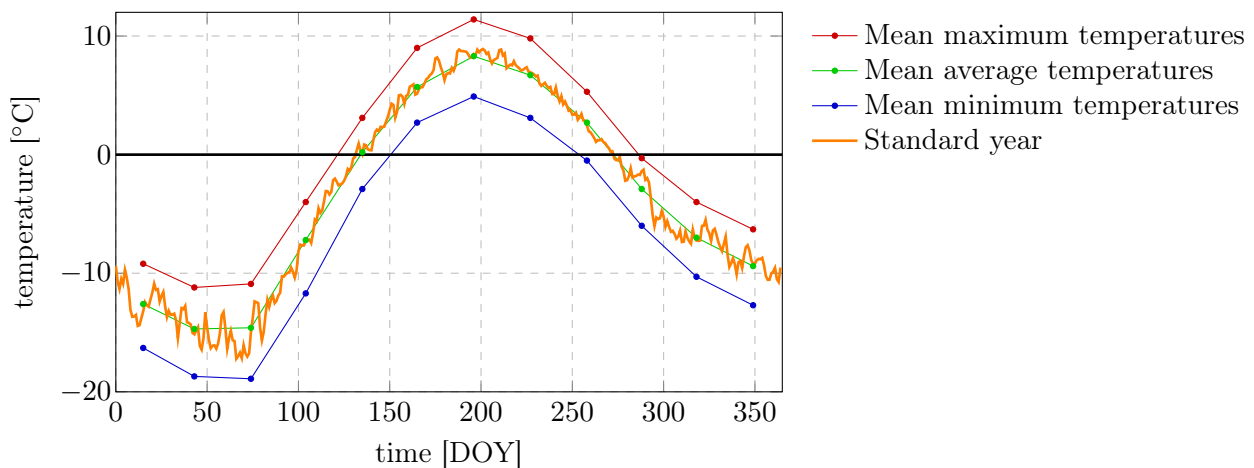


Figure 13: Monthly mean (green), maximum (red) and minimum (blue) air temperatures in Ilulissat between 1991 and 2020 (data provided by DMI (2022a)) as well as daily air temperature for a standard year (determined based on data between 1991 and 2021 from DMI (2022b))

The relative humidity is fluctuating between 62.0% and 67.5% within the last decade (DMI 2022c). I consider Ilulissat therefore as a place with rather stable and comfortable air humidity. The weather station is located at the airport and is thus largely unaffected by the city Ilulissat.

<sup>3</sup>as average of one month

The airport is located at approximately the same topographical height and distance from the sea as the city. The temperatures are relatively low all year round, hence less moisture can be stored in the air than at warmer temperatures (Figure 13).

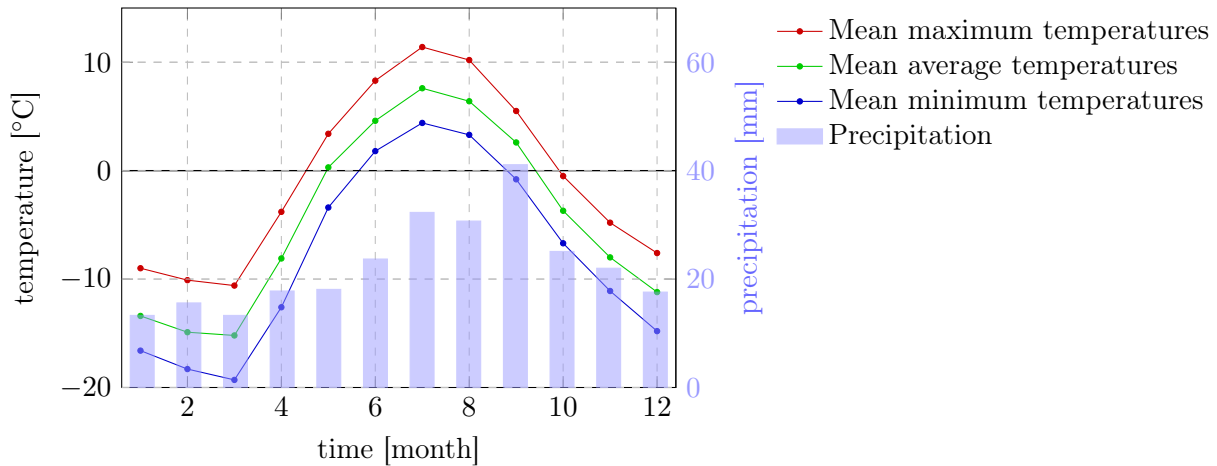


Figure 14: Climate graph with air temperature (1961-1990) and precipitation (1961-1984) for the weather station in the town Ilulissat (data provided by DMI (2022a))

The climate diagram with data from DMI shows a 30 years period between 1961 and 1990 for air temperature and a 24 years period for precipitation (Figure 14). Apart from minor deviations, the behavior of the air temperature curves are comparable to that in Figure 13, which represents the same data for a different period. In addition, the monthly sums of precipitation between 1961 and 1984 are recorded. The more recent data appear to have problems with recording precipitation. The maximum monthly precipitation does not rise above 45 mm on average in any month. This amount of precipitation with an annual total of about 270 mm is not particularly high. Due to the temperature distribution, it is mostly rain in summer (May to September) and snow in winter (September to May). The snow must be cleared for the maintenance of the roads. This snow is redistributed and accumulated at the shoulders and toes, which insulates the ground beneath and affects the thermal regime. The warmest months do not rise above 12 °C, so that Ilulissat can be classified as a tundra climate.

Wind speed and direction are important in relation to the redistribution of snow. I created a wind rose using the data from DMI since 1992 that shows the frequency [%] with which the wind blows from a certain direction. In Ilulissat, the prevailing wind is from the west over north-west and north to north-east (Figure 15). In addition, the windrose shows how often wind occurs at what speed [m/s] (Figure 15). Most of the year the speed stays below 40 km/h (blue to turquoise) and often also below 30 km/h (blue). Only in the yellow-green area more than 50 km/h occur. Snow drift caused by wind, leads to a significant amount of snow particularly on the eastern and south-eastern sides of roads when they are aligned in a NE-SW direction. Thus accumulation of snow around embankments is expected. Since the snow has an insulating effect, the temperature of the ground rises or it cannot be cooled as well, which favors the thawing processes in the permafrost. Accordingly, great importance must be attached to keep the area snow free during maintenance. The simulations later in my thesis emphasize the insulating effect of snow and its impact on the ground temperatures (see section 4 and subsection 5.2).

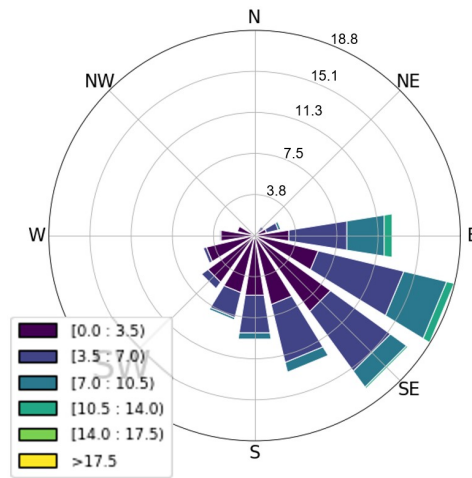


Figure 15: Wind rose of Ilulissat with frequency of wind direction [%] and wind speed [m/s] (determined based on data between 1992 and 2021 from DMI (2022b))

### 3.1.2 Climate forcing

For climate forcing, the reanalysis data ERA5 and the projection MPI-ESM in scenario SSP5-8.5 are used. The coordinates for Ilulissat are  $\text{lat} = 69.2167^\circ$  and  $\text{lon} = -51.1000^\circ$ , which is located in the centre of the town. The problem with Ilulissat is that it is a coastal town and therefore the nearest grid cells for the forcing data are on the sea, the ice sheet or in the ice fjord (Figure 16). This underestimates the temperature data for forcing in particular. Further estimates with coordinates slightly further inland at  $\text{lat} = 69.28^\circ$  and  $\text{lon} = -50.2^\circ$  or  $\text{lat} = 69.28^\circ$  and  $\text{lon} = -50.73^\circ$  show similar forcing data sets.

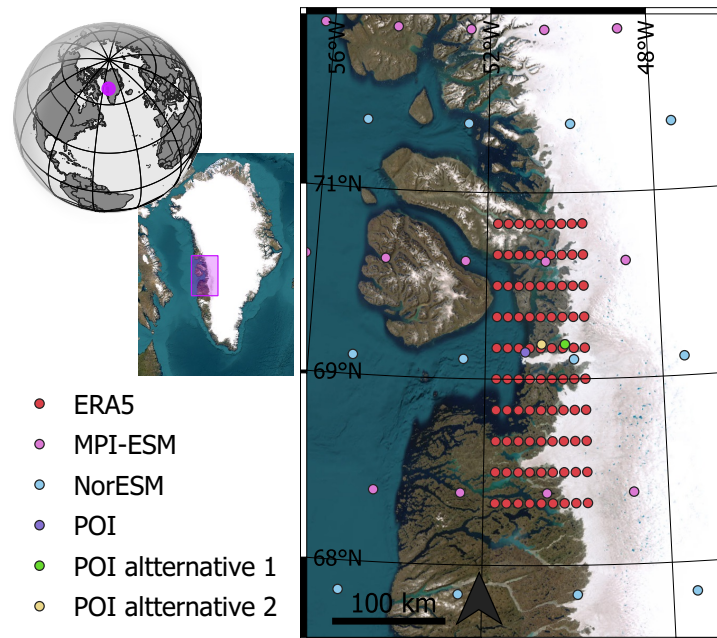


Figure 16: Map with grid points of ERA5, MPI-ESM, NorESM and the points of interest in the West Greenland region around Ilulissat. (Created with the support of Jennika Hammar from AWI.)

### 3.2 Ground thermal regime

Now that the climatic conditions are known, I discuss the ground thermal regime for Ilulissat in this section, showing the boreholes with their temperatures and properties, and their locations. I also show some near road iButton sensors with their respective problems.

#### 3.2.1 Borehole data

To investigate the ground thermal regime typically boreholes are equipped with a pipe and a string with temperature sensors at various depths. The thermistor string is connected to a data logger, which stores the temperature information at regular intervals. Someone needs to go back to the boreholes and read the logger because it can store approximately three years of temperature data and the battery has a limited lifespan. Newer, more expensive loggers are capable of transmitting data remotely. Based on the monthly averaged temperature, I create trumpet plots, which indicate the maximum and minimum temperatures within a year. The DTU boreholes, that I use to investigate the ground thermal regime, are from 2007, 2016, 2018 and 2021 (see Appendix C). Later, I compare the temperature profiles with the simulation results (see subsection 4.2.1). Their locations can be seen in Table 2, Figure 17 and Figure 18. In addition, investigations of the old airport are carried out by the Greenland surveying authority ASIAQ around 1980. These hand-read data are valuable, but I will not focus on them because they are not particularly high in both the spacing of the depth of the measured temperatures and in temporal resolution.

Using the ILU boreholes of DTU, I generate a temperature profile over the depth, which I use as input data at the beginning of the modelling with CryoGrid (see Table 1). Up to a depth of about 10 m, sufficient information is available from the thermistor measurements and the mean values are used. For greater depths, I make an estimate using the study of Schneider von Deimling et al. (2021) and the influence of the thermal gradient.

Table 1: Initial temperature profile for the CryoGrid Community Model in Ilulissat

Depth [m]	Temperature [°C]
0	0.4
0.5	-1.5
1	-1.8
2	-1.7
5	-2
10	-2.3
100	-2.5
1100	10.20

Table 2: Overview of DTU-boreholes from 2016, 2018 and 2021 in the Ilulissat area (based on Ingeman-Nielsen, Kaas, Lorentzen, Scheer & Tomaškovičová (2022) and Ingeman-Nielsen, Scheer & Tomaškovičová (2022))

Borehole	Drilled	Easting [m]	Northing [m]	Elevation [m a.s.l.]	Depth [m]	Thermistor string			Length [m]	Comments
						Type	S/N	Code		
ILU16001T	22-Aug-2016	498178	7681781	18.5	9.3	FG2	A521DD	EAB9	8	String broke in April 2019
ILU16002T	24-Aug-2016	498173	7681843	18.4	13.0	FG2	A521CC	E679	12	String broke in September 2020
ILU16005T	17-Sep-2016	497709	7681684	16.4	9.1	GP5W	A521E5	38B8	8	
ILU16009T	1-Sep-2016	498790	7682699	26.0	9.0	GP5W	A521DE	EBF9	8	
ILU16010T	2-Sep-2016	498816	7682840	23.6	8.7	GP5W	A521E1	FBB9	8	
ILU16011T	15-Sep-2016	498957	7682877	38.4	14.2	GP5W	A521DF	2B38	14	
ILU16013T	9-Sep-2016	499233	7683526	43.6	8.0	GP5W	A521E3	3A38	7	Defective from first season
ILU16015T	5-Sep-2016	499051	7683404	44.4	8.1	GP5W	A521E4	F879	8	
ILU16019T	12-Sep-2016	499073	7683696		12.0	GP5W	A521E0	3B78	10	
ILU16022T	16-Sep-2016	498261	7682614	2.6	11.2	GP5W	A521E2	FAF9	10	
ILU2018-01	14-Aug-2018	496974.61	7679928.26		1.28					
ILU2018-02	14-Aug-2018	497378.11	7680109.31		1.52					
ILU2018-03	15-Aug-2018	495778.00	7678265.00		6.60	GP5W	A5395F	8B33	6	
ILU2018-04	18-Aug-2018	497536.27	7681010.33	49.464	4.15	GP5W	A522BC	F278	4	
ILU2021-01	8-Apr-2021	497326.55	7678361.18	64.743	6.20					
ILU2021-02	9-Apr-2021	497826.56	7678810.92	63.867	6.50	FG2	A53CE4	4AFE	6	
ILU2021-03	10-Apr-2021	496915.72	7679420.24	60.768	2.88					
ILU2021-04	15-Apr-2021	498599.44	7678459.76		1.50					
ILU2021-05	15-Apr-2021	498536.52	7678424.18		2.00					

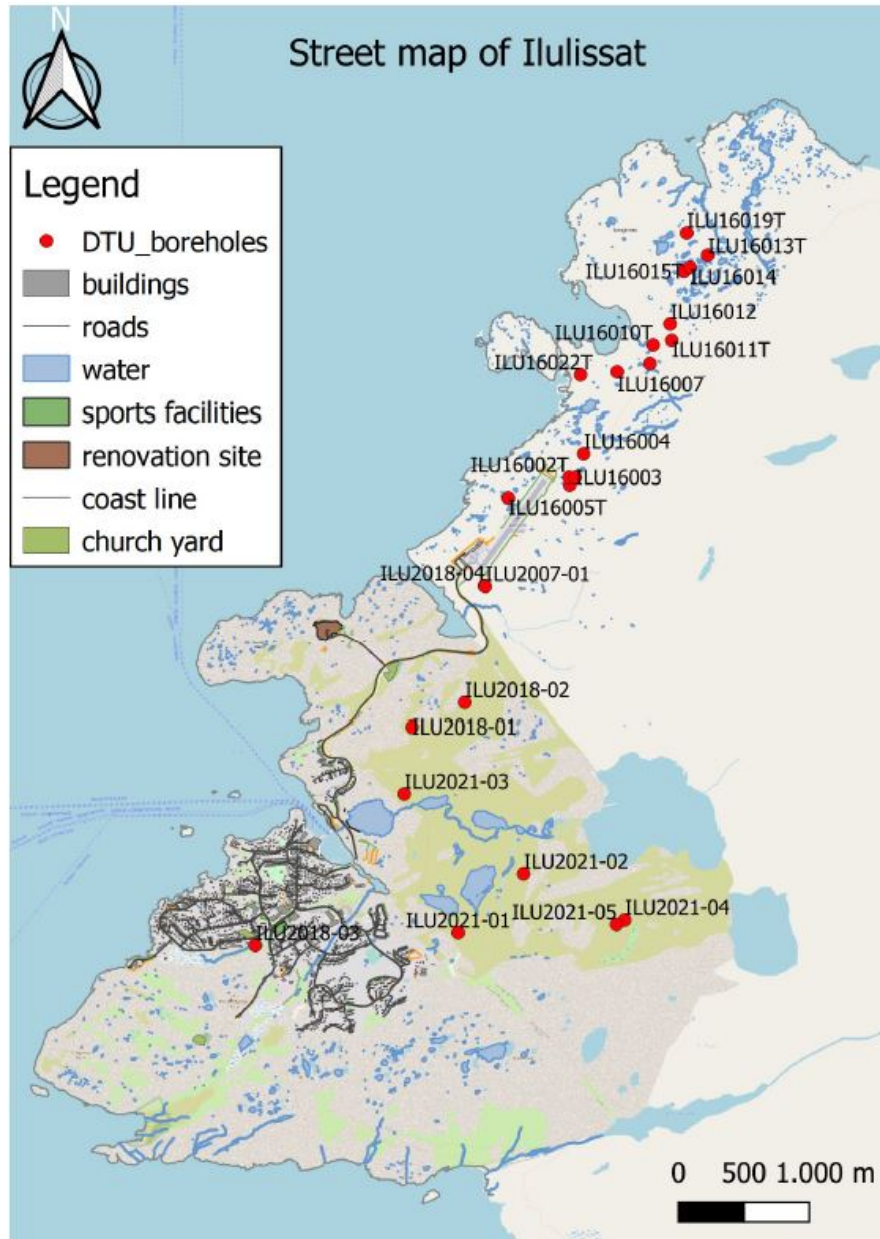


Figure 17: Street map of Ilulissat with locations of the boreholes

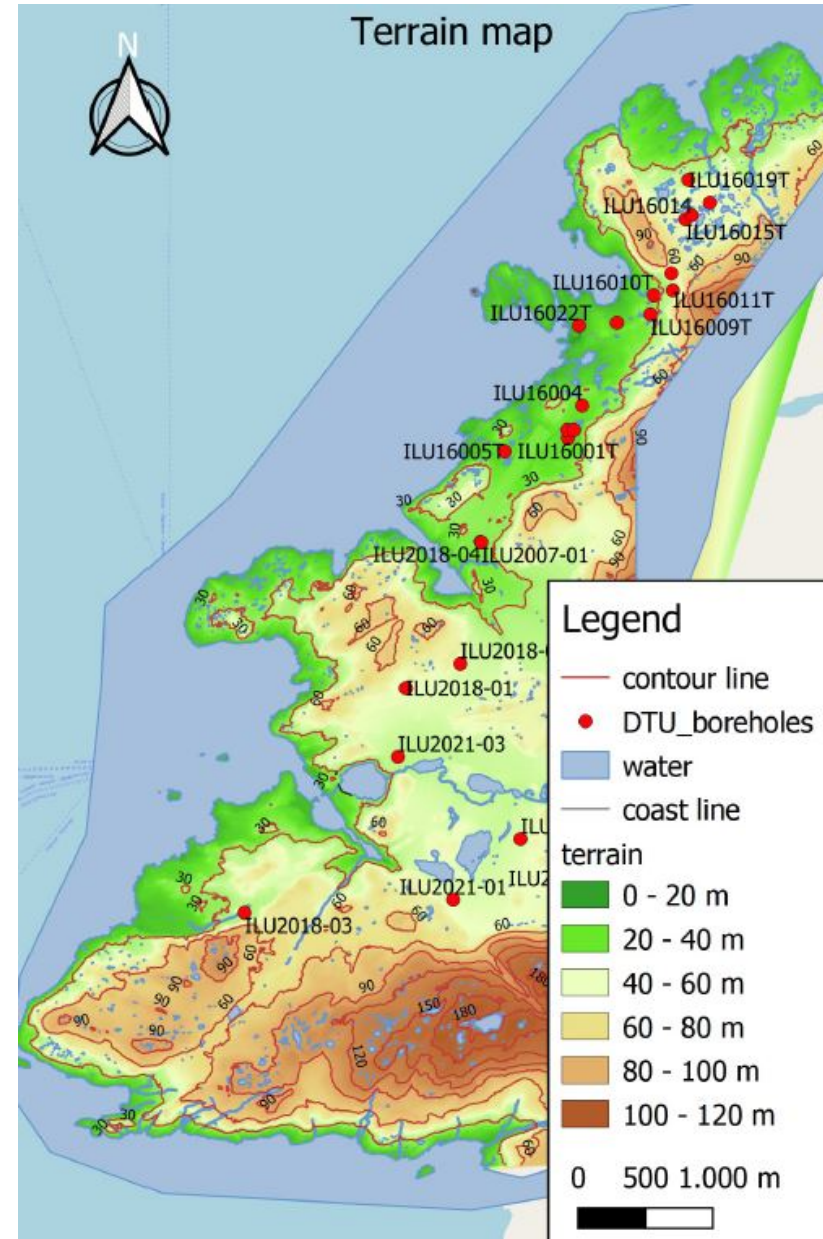


Figure 18: Terrain map of Ilulissat with locations of the boreholes

With regard to the thermal regime in the Ilulissat region, it should be noted that the sea level was historically significantly higher and thus marine clay and silt deposits can be found in the basins up to around 50 m above sea level (Foged & Bæk-Madsen 1980, Weidick & Bennike 2007) to 70-100 m above sea level Rasch (2000). This affects almost the entire infrastructure in Ilulissat. Nearly all roads are below 50 m altitude (see Figure 18 and 17). Accordingly, these layers had a higher salinity, which has already been washed out in many places by the groundwater flow. The increased salinity in the soil and thus also in the pore water leads to freezing-point depressions, which shift the dew point into the negative temperature range. As a result, the soil may not or only partly freeze despite negative temperatures, which in turn has an influence on the stability. According to Foged & Bæk-Madsen (1980), this leads to a very unstable limit between the frozen and partly frozen soil. Thus, even small changes in the external thermal conditions can trigger large changes in the frost balance. Due to the permafrost temperature between 0°C and -4°C (see Appendix C) and the high salinity of up to 38.2% (Geo 2017), an unstable ratio is established between the thawed saline soil and the overburden frozen soil. Especially the large sediment basins with partly frozen clay and silt at greater depths (cf. Foged & Bæk-Madsen (1980)) harbor the risk of thaw.

### 3.2.2 iButton data

Due to their comparatively low price and simple installation, the iButtons are used over a much wider area and serve as a supplement to thermistor strings in boreholes. They measure the temperature in the near-surface area and are well suited for the investigation of local small-scale differences. For my thesis I use the iButton data as validation for temperature differences due to the influence of plowed snow from the road on the embankment. In Ilulissat, iButtons have been placed, replaced and read at over 50 locations in Ilulissat in different field campaigns between 2018 and 2021, with 26 located close to the road. This work was carried out and provided by Johanna Scheer, PhD candidate at DTU. For my thesis, I select three suitable locations where the sensors were retrieved, read out and replaced and where an influence of the road can be investigated (Figure 20). These are located on the road from the city to the airport and in the center close to the borehole ILU2018-03. The iButton model used in Ilulissat is DS1922L (Thermochron8k) (Scheer 2020).

Table 3: Overview of the locations of the iButton sensors for the three selected locations

Location 1			Location 2			Location 3		
Sensor	Latitude [°]	Longitude [°]	Sensor	Latitude [°]	Longitude [°]	Sensor	Latitude [°]	Longitude [°]
4C-D46	69.22952	-51.08878	ED-3D0	69.22868	-51.09225	75-D11	69.214880	-51.103830
DE-814	69.22963	-51.08858	96-B21	69.22867	-51.09221	64-42F	69.215190	-51.104920
61-ACF	69.22969	-51.08848	D9-B8F	69.22588	-51.08847	7F-080	69.214850	-51.106390
15-838	69.22977	-51.08808	47-FAE	69.22583	-51.08849	1F-643	69.215230	-51.103690
B2-044	69.22980	-51.10000	B1-116	69.22603	-51.08917	<b>ILU2018-03</b>	<b>69.214331</b>	<b>-51.106604</b>
D4-0D7	69.22970	-51.08858						

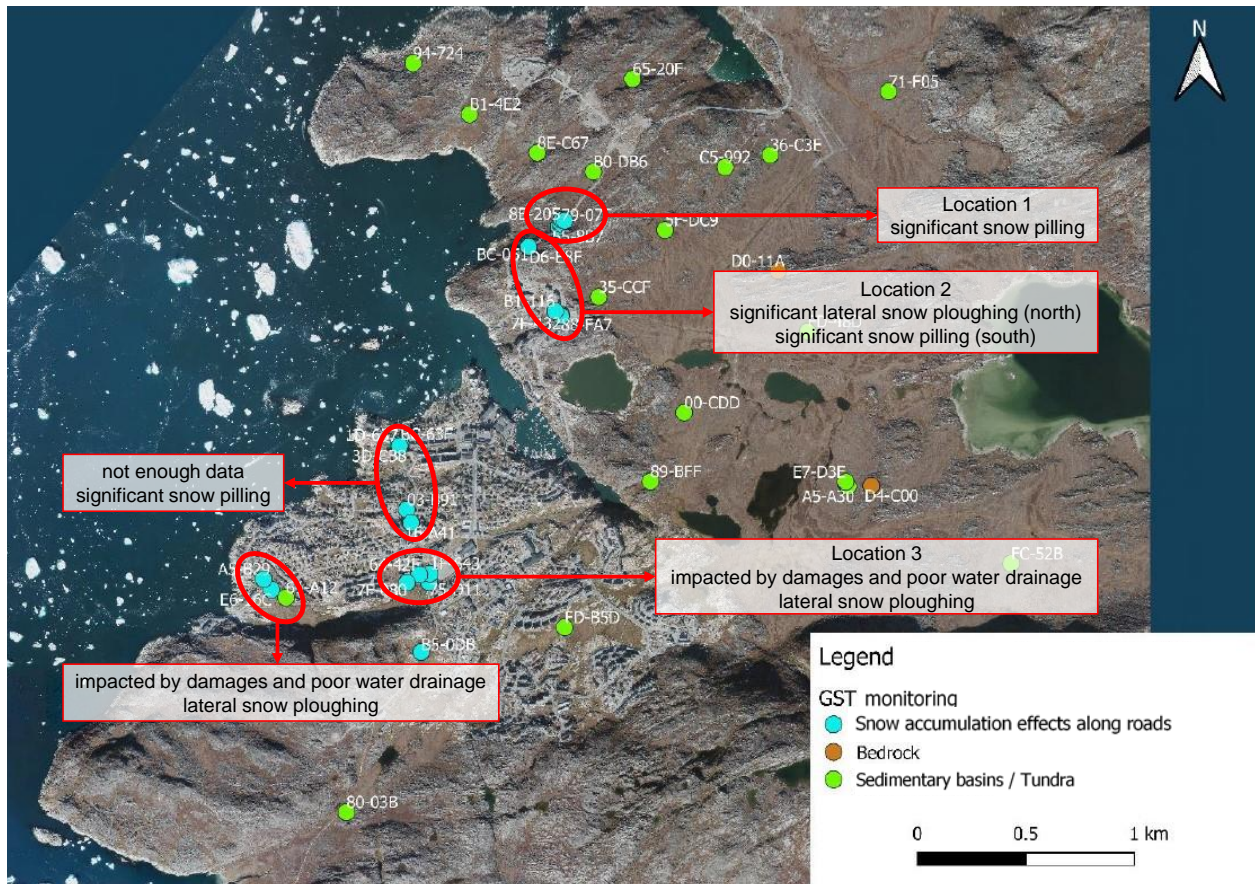


Figure 19: iButton network deployed in Ilulissat for the year 2020-2021 with information regarding some sensors (Adapted from Scheer (2020)).

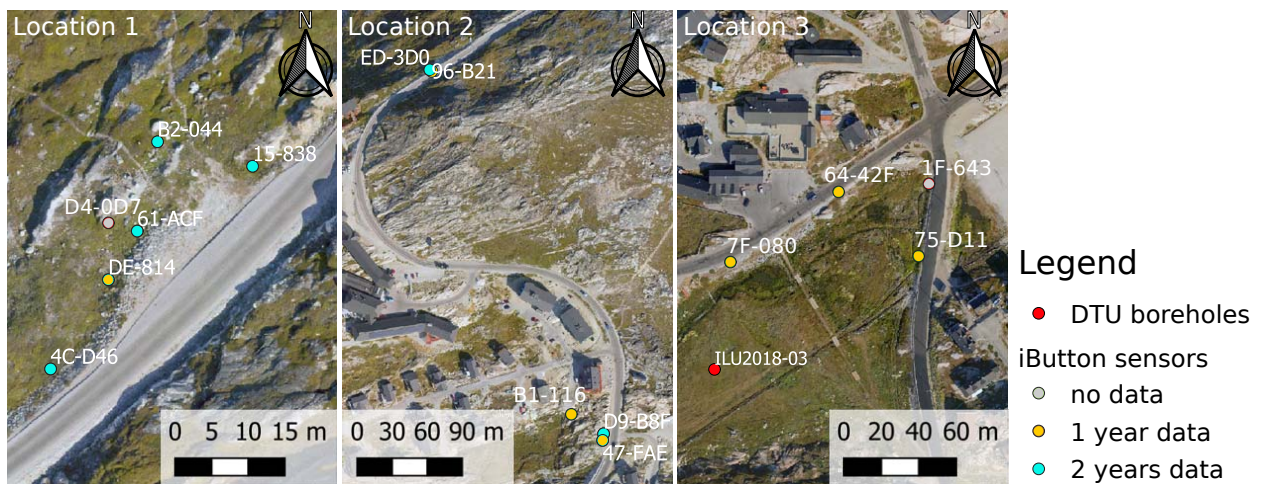


Figure 20: Close-up of the location of the iButtons sensors that are close to the road with their data recording period

### 3.3 Road construction

In this section, I introduce some special features and regulations concerning road construction in Greenland. In Greenland in general roads have the following speed limits according to their mode of operation: 60 km/h on the limited rural roads, 40 km/h on urban roads, 30 to 40 km/h on local roads and 15 to 30 km/h on residential roads (Grønlands Hjemmestyre & Rambøll 2008). Those limitations influence the design of the road and embankment. In the guidance for roads in Greenland (Grønlands Hjemmestyre & Rambøll 2008) there are defined regulations regarding the radius of horizontal curves and the road inclination in curves depending on the speed factor and visibility. Furthermore, the maximum elevation differences and the minimum radius of curvature in longitudinal direction are regulated.

For permafrost related problems the Greenlandic rules (Grønlands Hjemmestyre & Rambøll 2008) are showing how to excavate to the permafrost and fill it afterwards to avoid issues originating from the AL. Concerning the drainage and water in the soil body, permafrost is neglected in the regulations. But from other studies it is known, that it can cause stability problems (Connor et al. 2020, Hjort et al. 2022, Wang 2017).

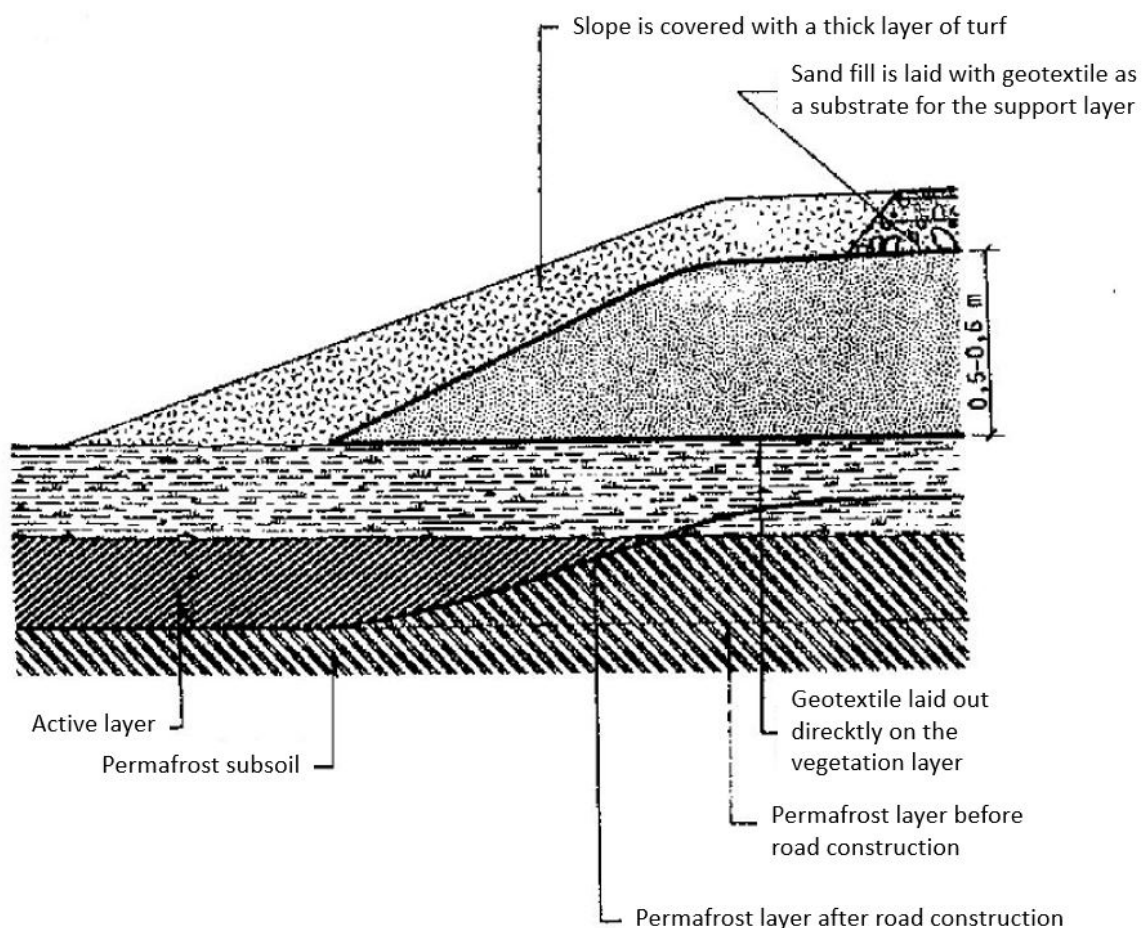


Figure 21: Schematic standardised cross section of a road on permafrost subsoil (Bigum and Steenfos 1984)

The general guidelines from 1984 for road construction in Greenland suggest to built the embankment with non-frost susceptible material (Bigum and Steenfos 1984). Furthermore, it should have a sufficient thickness to allow seasonal thawing and an AL only within the embankment. The soil beneath should stay in a frozen state. This approach can be costly. The report refers briefly to the use of peat and organic layers to protect and insulate the natural soil beneath which is likely to cause other issues like a reduced bearing capacity (Bigum and Steenfos 1984). Another concept is the use of geotextiles between the natural soil and the embankment, which should avoid longitudinal cracks but allow drainage. Several cross sections for different situations are presented in Bigum and Steenfos (1984) and the one with permafrost containing a geotextile can be seen in Figure 21. However, those cross sections are almost 40 years old, which might need some reevaluation when using it for new road construction. Furthermore, the measures from subsection 1.2 can be implemented in road construction in Greenland.

### 3.4 Model setup

For the model setup with the CryoGrid community model, I use a basic road setup adapted to the Greenlandic rules according to Grønlands Hjemmestyre & Rambøll (2008) (Figure 22). I assume that the roads are rather narrow with a total width of 6 m and thus a width of 1.8 m has to be kept available to store the snow there. Furthermore, I assume a slope of 1:2 for the shoulder. Subsequently, I simulate different scenarios, which vary in the distribution of snow, the albedo of the road surface, the properties of the gravel and the excess ice content. The corresponding setups with their configurations can be found in Table 4.

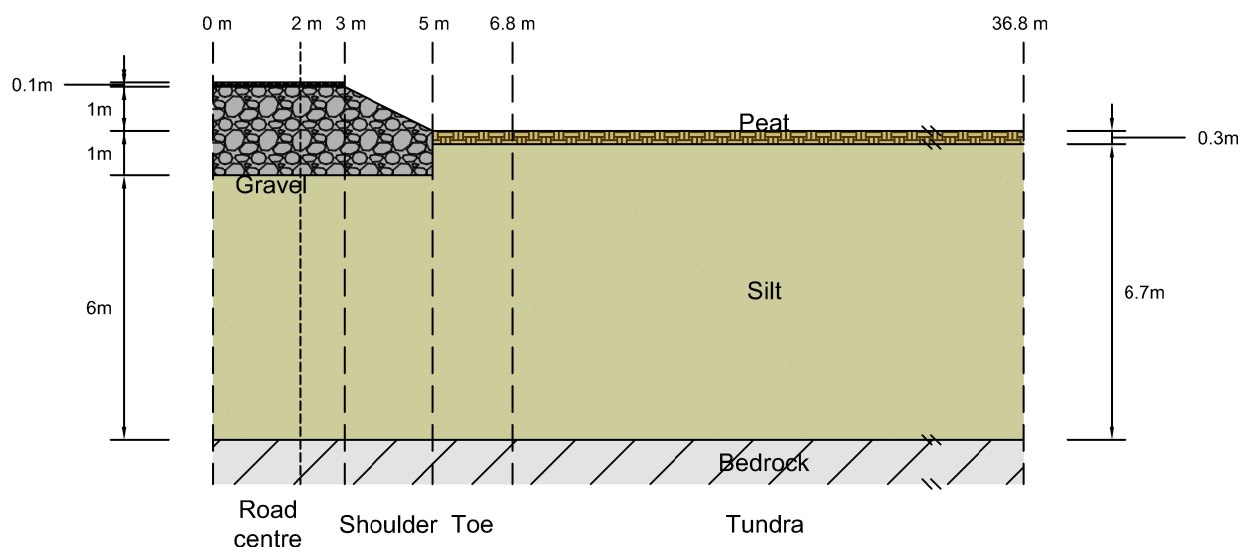


Figure 22: Schematic half cross section showing the modelled road center to adjacent tundra in Ilulissat. The dimensions of the five tiles are indicated in the horizontal and vertical directions.

The parameters used are listed in Table 5, with the respective scenarios added for variable values.

Table 4: Overview of the modelled scenarios and their characteristic properties with regard to the distribution of snow, the composition and surface of the road, and the presence of excess ice, including references to the respective figures and parameters.

ID	description	snow	road	excess ice	figure
a)	Standard scenario	2x shoulder and toe 1x tundra	gravel road	not present	Figure 23
b)	Scenario with low road albedo	2x shoulder and toe 1x tundra	dark gravel road	not present	Figure 23
c)	Scenario with low road albedo and cleared embankment	no snow on shoulder 2x toe 1x tundra	dark gravel road	not present	Figure 24
d)	Scenario with cleared embankment	no snow on shoulder 2x toe 1x tundra	gravel road	not present	Figure 24
e)	Scenario with changed gravel layer properties	2x shoulder and toe 1x tundra	gravel road with changed properties	not present	Figure 23
f)	Scenario with excess ice	2x shoulder and toe 1x tundra	gravel road	excess ice -1m ... -2m	Figure 25

Table 5: Model parameters in the CryoGrid Community model used in the thesis

Albedo	Snow-free surface tundra	0.2	Langer et al. (2011)
Albedo	Pond	0.07	Burt (1954)
Albedo	Snow-free surface gravel road cases a) and d) to f)	0.3	Andersland & Ladanyi (1994)
Albedo	Snow-free surface dark gravel road cases b) and c)	0.1	Rosenfeld et al. (1995) Lima et al. (2023)
Density	Snow cover	250 kg/m <sup>3</sup>	Sturm et al. (2010)
Thermal conductivity	Mineral soil and gravel fraction cases a) to d) and f)	3.0 W/(m K)	Farouki (1982) Langer et al. (2013) Côté & Konrad (2005)
Thermal conductivity	Mineral soil and gravel fraction case e)	1.5 W/(m K)	Hassn et al. (2016) Adam et al. (2023)
Thermal conductivity	Organic soil fraction	0.25 W/(m K)	Hillel (1982)
Hydraulic conductivity	Below surface ground	10 <sup>-5</sup> m/s	Boike et al. (2019)
Volumetric heat capacity	Mineral soil and gravel fraction cases a) to d) and f)	2 · 10 <sup>6</sup> J/(K m <sup>3</sup> )	Farouki (1982)
Volumetric heat capacity	Mineral soil and gravel fraction case e)	1.7 · 10 <sup>6</sup> J/(K m <sup>3</sup> )	Hassn et al. (2016) Andersland & Ladanyi (1994) Adam et al. (2023)
Volumetric heat capacity	Organic soil fraction	2.5 · 10 <sup>6</sup> J/(K m <sup>3</sup> )	Hillel (1982)
Geothermal heat flux	Lower model boundary	44 mW/m <sup>2</sup>	Colgan et al. (2022)

### Scenarios a) to e)

The scenarios a) to e) from Table 4 describe different combinations of snow distribution, road albedo and road parameters. I make a distinction between gravel road and dark gravel road with different albedo values,  $\alpha = 0.3$  for gravel and  $\alpha = 0.1$  for dark gravel (Table 5). Furthermore, I

change the parameters thermal conductivity  $k$  and volumetric heat capacity  $c$  of the mineral soil and gravel fraction in scenario e) from  $k = 2 \cdot 10^6 \text{ J}/(\text{K m}^3)$  to  $k = 1.5 \cdot 10^6 \text{ J}/(\text{K m}^3)$  and  $c = 3.0 \text{ W}/(\text{m K})$  to  $c = 1.5 \text{ W}/(\text{m K})$ . Another adjusted variable within the scenarios is the distribution of snow next to the road. Scenario a), b) and e) have the single amount of snow on the tundra tile and the double amount on shoulder and toe. The road itself has no snow, as it is assumed that the snow is ploughed from the road to the side onto the embankment. This case can be seen in Figure 23. Scenarios c) and d) represent the situation when the snow is also cleared from the shoulder and is pushed further away from the road onto the toe (doubled amount of snow) or is transported by trucks to another location. This situation can be seen in Figure 24.

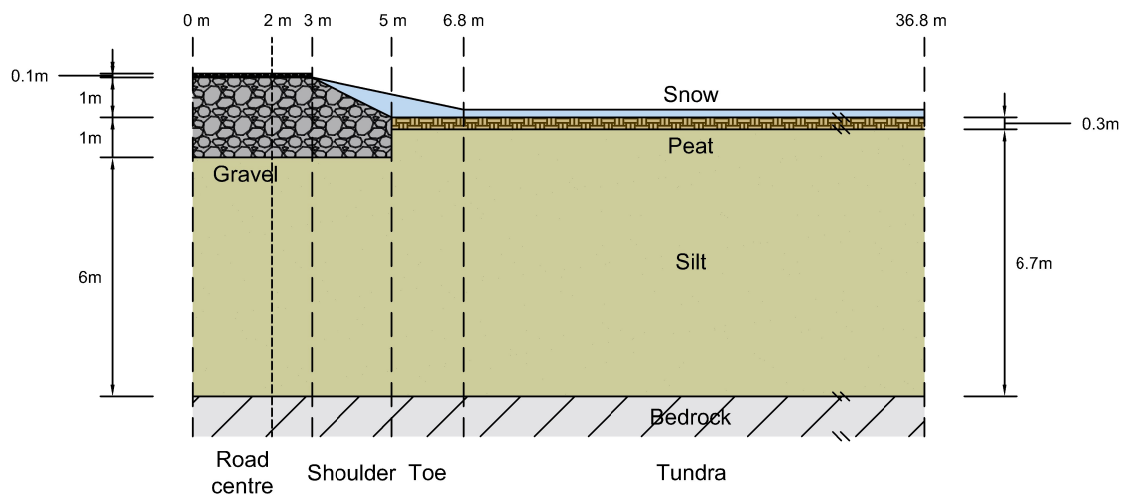


Figure 23: Schematic half cross section showing the modelled road center to adjacent tundra in Ilulissat with double amount of snow on shoulder and toe and single amount of snow on the tundra. The dimensions of the five tiles are indicated in the horizontal and vertical directions.

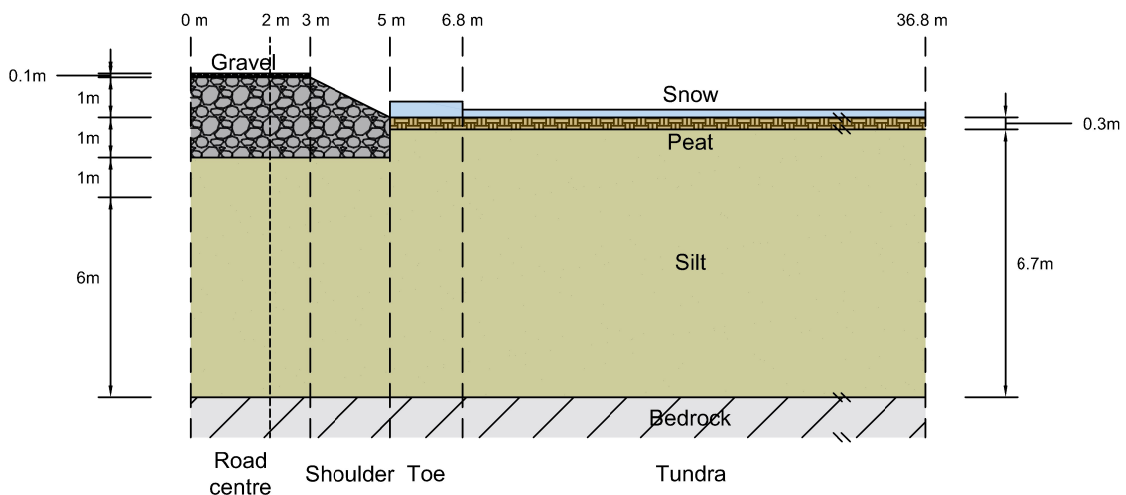


Figure 24: Schematic half cross section showing the modelled road center to adjacent tundra in Ilulissat with shoulder cleared from snow, toe with double amount of snow and tundra single amount of snow. The dimensions of the five tiles are indicated in the horizontal and vertical directions.

What unites all these scenarios is the structure of their ground stratigraphy. For my setup, I use the volumetric fractions of water and ice  $\theta_{wi}$ , minerals  $\theta_m$ , organic content  $\theta_o$  and field capacity  $\theta_{fc}$  that are shown in Table 6. The soil type and saturated hydraulic conductivity are also indicated. In Table 6 only the tiles for road and tundra are described. For the other tiles the depth coordinates differs, but the composition remains the same. To avoid large gradients for the slope of the shoulder, I set the surface level for the shoulder at +0.5 m as an approximate intermediate between road and toe. The Figure 22 to 25 is in this case an idealised representation. With more tiles it would be possible to refine this further.

Table 6: Ground stratigraphies with volumetric fractions of the ground constituents for the standard scenario

Depth [m]	water and ice $\theta_{wi} = \theta_w + \theta_i$ [-]	mineral $\theta_m$ [-]	organic $\theta_o$ [-]	excess ice $\theta_{\chi i}$ [-]	field capacity $\theta_{fc}$ [-]	soil type	saturated hydraulic conductivity $K_{w,sat}$ [m/s]
Road							
1.1 ... 1.0	0.2	0.8	0	0	0.1	gravel	1.00E-05
1.0 ... -1	0.3	0.7	0	0	0.1	gravel	1.00E-05
-1 ... -7	0.4	0.55	0.05	0	0.25	silt	1.00E-06
< -7	0.3	0.7	0	0	0.03	bedrock	1.00E-10
Tundra							
0 ... -0.3	0.75	0.05	0.2	0	0.5	peat	1.00E-07
-0.3 ... -7	0.4	0.55	0.05	0	0.25	silt	1.00E-06
< -7	0.3	0.7	0	0	0.03	bedrock	1.00E-10

### Scenario f)

Scenario f) includes the presence of excess ice from 1 m to 2 m depth across all tiles (Figure 25). The excess ice is located below the gravel in the upper part of the permafrost, which is assumed to average 1 m (Ingeman-Nielsen, Kaas, Lorentzen, Scheer & Tomaškovičová 2022). The massive ice in this area is assumed to be 50 % in addition to the total volume of soil (Table 7). The Table 7 is comparable with Table 6, but with the excess ice layer in the silt in the modelled stratigraphy.

Table 7: Ground stratigraphies with volumetric fractions of the ground constituents for the szenario with excess ice

Depth [m]	water and ice $\theta_{wi} = \theta_w + \theta_i$ [-]	mineral $\theta_m$ [-]	organic $\theta_o$ [-]	excess ice $\theta_{\chi i}$ [-]	field capacity $\theta_{fc}$ [-]	soil type	saturated hydraulic conductivity $K_{w,sat}$ [m/s]
Road							
1.1 ... 1.0	0.2	0.8	0	0	0.1	gravel	1.00E-05
1.0 ... -1	0.3	0.7	0	0	0.1	gravel	1.00E-05
-1 ... -2	0.4	0.55	0.05	0.5	0.25	silt	1.00E-06
-2 ... -7	0.4	0.55	0.05	0	0.25	silt	1.00E-06
< -7	0.3	0.7	0	0	0.03	bedrock	1.00E-10
Tundra							
0 ... -0.3	0.75	0.05	0.2	0	0.5	peat	1.00E-07
-0.3 ... -1	0.4	0.55	0.05	0	0.25	silt	1.00E-06
-1 ... -2	0.4	0.55	0.05	0.5	0.25	silt	1.00E-06
-2 ... -7	0.4	0.55	0.05	0	0.25	silt	1.00E-06
< -7	0.3	0.7	0	0	0.03	bedrock	1.00E-10

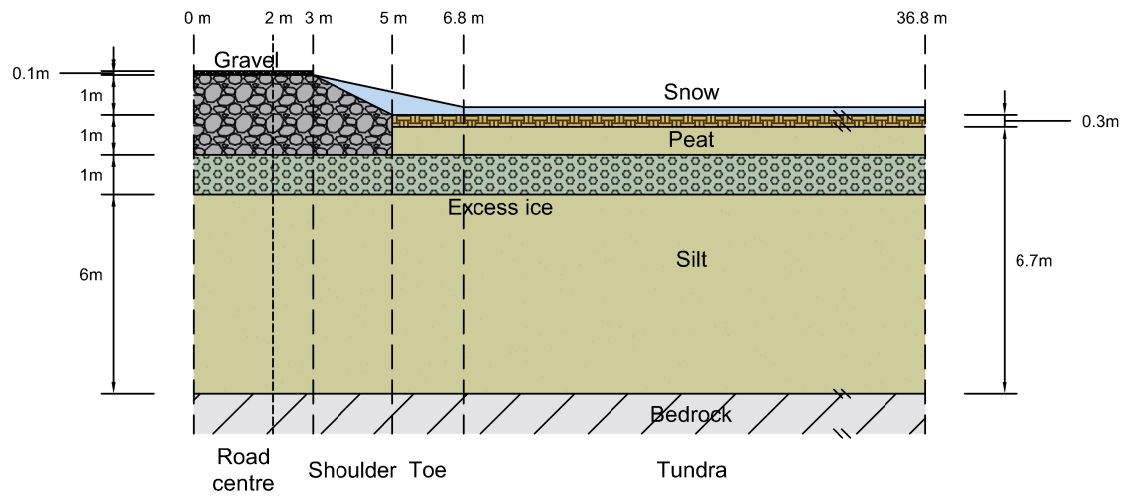


Figure 25: Schematic half cross section from the road centre to the adjacent tundra in Ilulissat with excess ice layer between 1 m and 2 m depth. The dimensions of the five tiles are indicated in the horizontal and vertical directions.

## 4 Results

In this section, I present the results generated using the methods described earlier. First, I discuss the forcing data and the validation with observation data. This is followed by the validation of ground temperatures from the model to the boreholes and the variation in the iButton results. Finally, I present the results of the initialization of the model and the different scenarios I simulated with CryoGrid.

### 4.1 Forcing data

Using the forcing data set and the weather station data, I perform a comparison for the temperature and snowfall parameters in this section. For the reanalysis data the direct comparison is possible, for the future projection I use trends.

#### 4.1.1 Temperature

One of the resulting quantities from the forcing data, consisting of the reanalysis data from ERA5 and the projections from MPI-ESM in scenario SSP5-8.5, is the temperature at 2 m altitude. I compared reanalysis data with data from DMI's weather station, which has recorded air temperature for Ilulissat since 1991 (Figure 26). The correlation between the data from the weather station and the forcing is evident and can be better assessed by zooming in (Figure 27). For this purpose, I choose an arbitrary period of the length of a year. However, the optical control is not quantifiable, which is why the correlation of the two temperatures to each other is also shown for the period from June 2014 to June 2015 (Figure 28). The correlation shows that the comparison points are predominantly close to the axis of symmetry. For the positive temperatures, the deviations of DMI and ERA5 are a maximum of  $10^{\circ}\text{C}$ . For temperatures below  $-10^{\circ}\text{C}$ , this deviation can be a maximum of  $15^{\circ}\text{C}$ . For the temperature range below the freezing point down to  $-10^{\circ}\text{C}$ , larger deviations of maximum  $20^{\circ}\text{C}$  are observed (Figure 28). However, it should be emphasised that

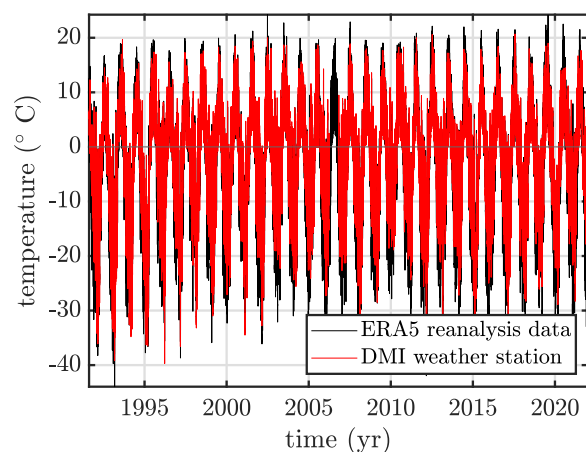


Figure 26: Comparison of 2 m temperature from ERA5 reanalysis data with measured 2 m air temperature data from DMI's weather station in Ilulissat for the period from 1992 to 2022. 3 hourly data 1991-1996; hourly data 1997-today

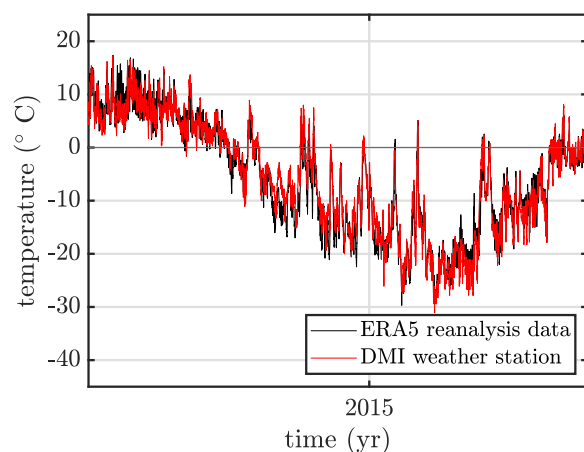


Figure 27: Closeup for the comparison of 2 m temperature from ERA5 reanalysis data with measured 2 m air temperature data from DMI's weather station in Ilulissat for the period 22.06.2014 to 21.06.2015.

these are single values for hourly temperature readings. The large amount of values are close to the red straight line with deviations of maximum  $5^{\circ}\text{C}$  and correlate well with each other. The correlation factor is  $R=0.82$ . The temperatures of the ERA5 data thus give a good agreement with the measured values of the DMI weather station.

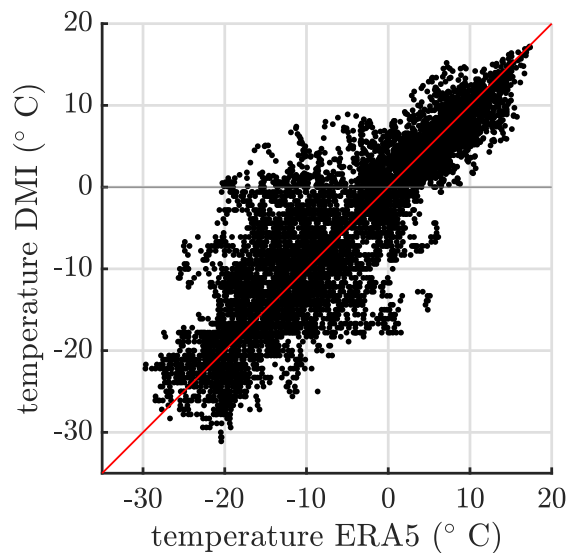


Figure 28: Correlation of the 2m temperature of ERA5 reanalysis data with measured 2m air temperature data from DMI's weather station in Ilulissat for the period 22.06.2014 to 21.06.2015. The correlation factor is 0.82

Another way of comparing temperature data and their development is to use the freezing and thawing index (Figure 29). This is done for the DMI data from 1992 to 2021. My analysis includes only data sets with a complete year cycle, thus excluding 1991 because it starts in August and excluding 2006 due to missing data from April to October. The results are summarized in Figure 29. The thawing index is quite stable, whereas the freezing index fluctuates strongly. Based on the indices, I determined the linear trend (Table 8), where the thawing index is slightly rising but the freezing index indicates an eight times stronger increasing behaviour. This means that the periods of cold sub-zero temperatures are warming. Due to the characteristic of the calculation (Equation 1) no statement can be made as to whether the number of days with positive/negative temperatures changes. Comparing the indices of the weather station and the forcing for the comparable period, the thawing index is just under  $1000^{\circ}\text{d}$  and the freezing index is slightly below  $-2000^{\circ}\text{d}$ . The exact values and the linear trends of the individual indices can be found in Table 8. Both freezing index  $I_f$  and thawing index  $I_t$  tend to increase, indicating a warming of the study site Ilulissat. The exact trend for individual sections can be found in Table 8.

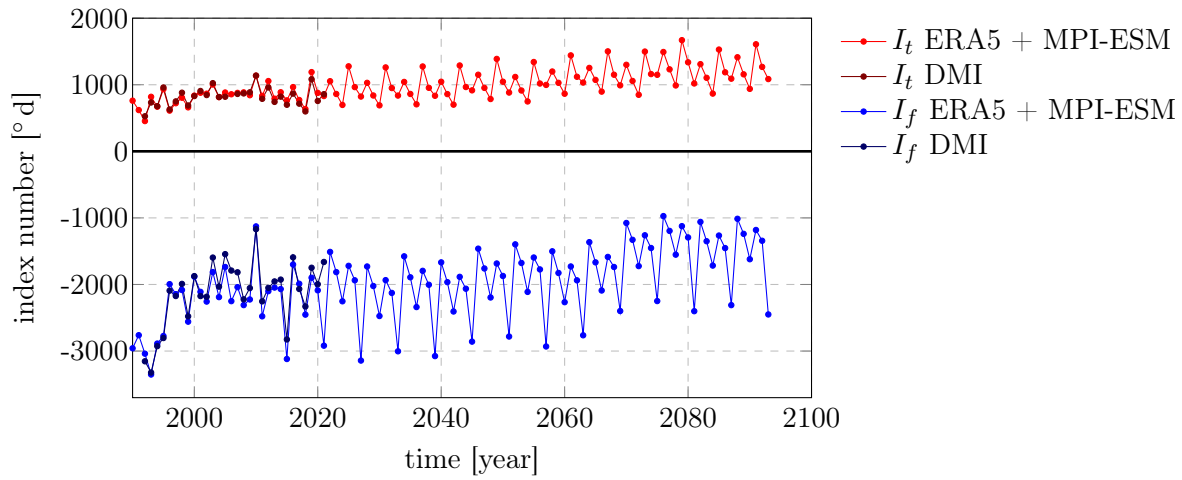


Figure 29: Freezing and thawing degree indices for the climate forcing ERA5, MPI-ESM and the weather station from DMI.

Table 8: Freezing and thawing indices  $I_f$  and  $I_t$  from DMI weather station and ERA5 reanalysis data with their trend over 30 years (1992-2021).

	Period	$I_t$		$I_f$	
		Average	Trend	Average	Trend
DMI	1992 - 2021	818 ° d	+3.4 °d/yr	-2127 ° d	+27.9 °d/yr
ERA5	1992 - 2021	839 ° d	+7.0 °d/yr	-2170 ° d	+14.9 °d/yr
MPI-ESM	2022 - 2093	1082 ° d	+5.4 °d/yr	-1846 ° d	+10.9 °d/yr

For the consideration of the MPI-ESM projections, the MAAT are first plotted to assess the development (Figure 30). A slight trend of warming with an inclination of 0.045 K/yr can be seen for the period from 2022 to 2093. A cyclic behaviour is clearly recognisable. This is due to the process of linking the data series (ERA5 + MPI-ESM), as only the trend within the overlap period was used and transferred to the future. This reflects the cyclical nature of the overlap period. In addition to the trend, the changes from the previous year are also shown (Figure 30), which fluctuate between 5 °C and -5 °C, but tend to be in the slightly positive range as shown by the trend.

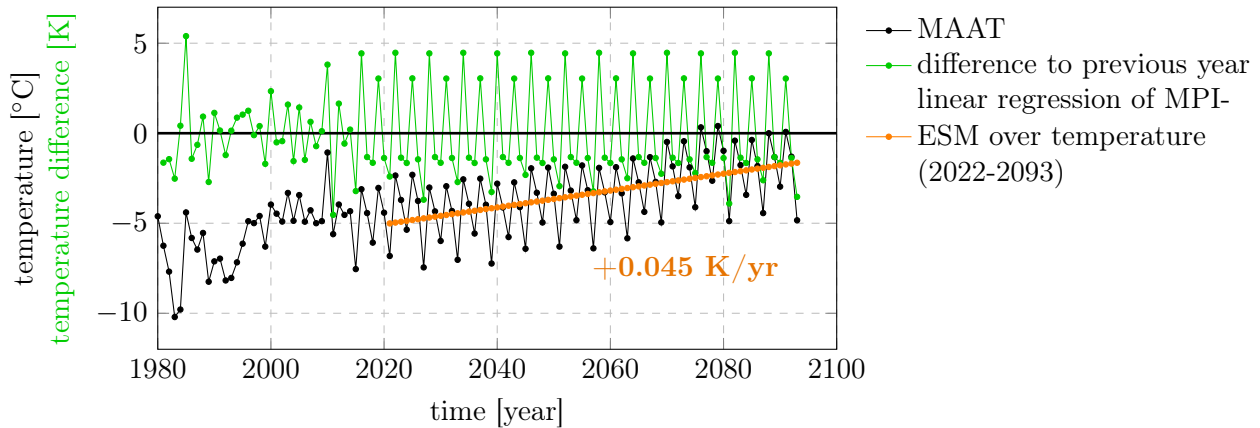


Figure 30: Mean annual air temperature for Ilulissat from ERA5 and MPI-ESM with the corresponding temperature differences from one year to another.

Furthermore, I calculate the mean value of the temperatures of each week, illustrating examples of the first week in January and the 20<sup>th</sup> week of the year in May (Figure 31). For each week, I determine the minimum, mean, and maximum temperatures, with the slope as a linear regression over the mean value. These plots also show the cyclical behaviour of the temperatures with a periodicity of six years. In winter the fluctuations are  $\pm 10$  K with a few exceptions and a steeper slope of  $+0.0833$  K/yr. In the beginning of summer, on the other hand, the fluctuations are somewhat smaller at  $\pm 8$  K and the slope approximately half as flat at  $+0.0408$  K/yr.

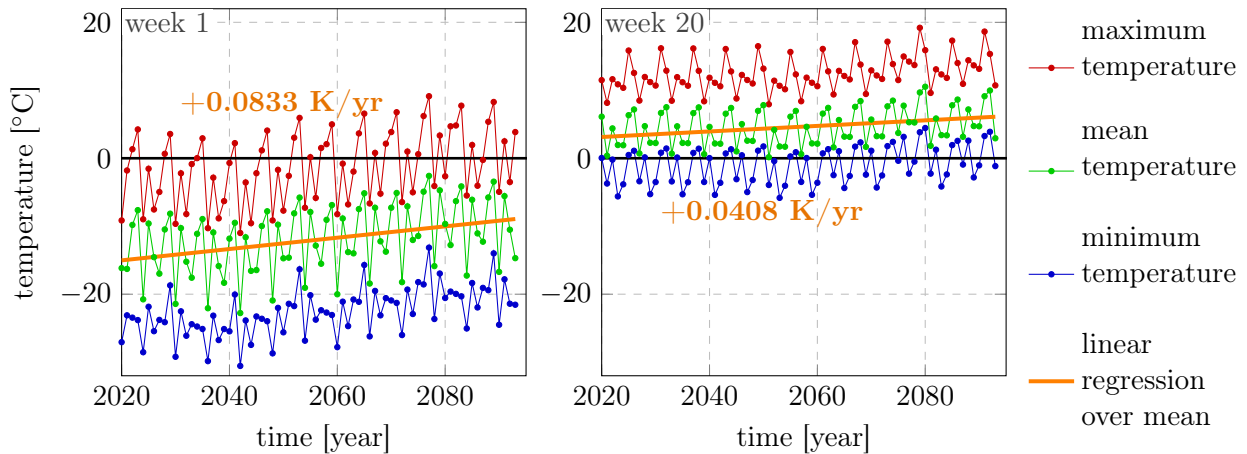


Figure 31: Weekly averaged maximum, mean and minimum 2 m air temperature for the first week for each year (early January) and the 20<sup>th</sup> week for each year (mid-May) including the slope based on MPI-ESM projection with scenario SSP5-8.5.

To better understand the temperature changes within a year, the weekly slope described above are viewed either over individual shorter periods (Figure 32) or over the entire period (Figure 33). In Figure 32, the period of observation is chosen to be six years, which corresponds exactly to the cyclical repetition period. For this reason, the graphs are very close together, almost non-distinctive. However, tendencies can be recognised. Accordingly, the year begins in winter with a positive slope and thus warming, which is replaced in calendar week 11-13 with the starting spring

by a sudden cooling. This is followed over the summer by an alternation of cooling and warming with a predominant tendency towards warming. In fall and winter there are again stronger fluctuations with two cooling phases in weeks 42-43 and 49-50 (Figure 32).

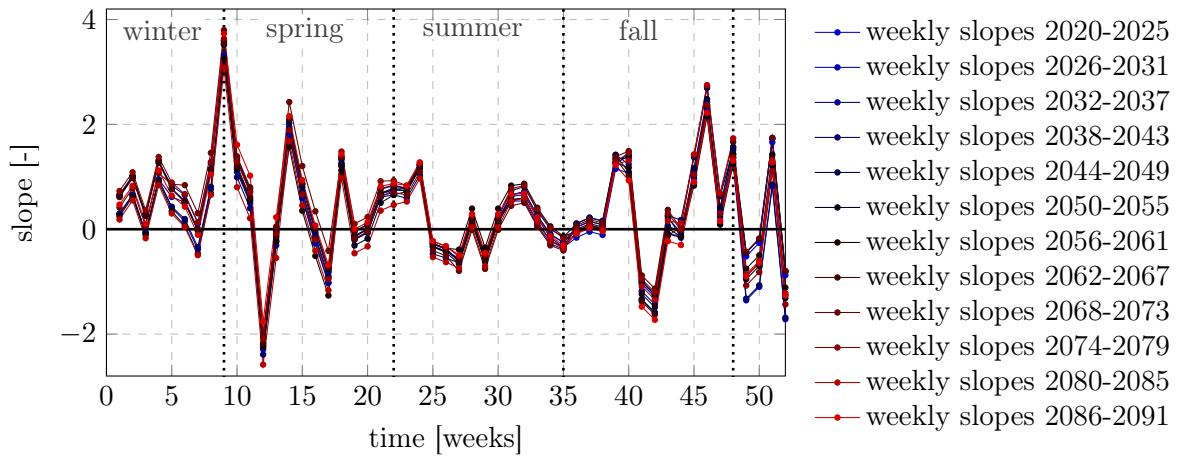


Figure 32: Weekly averaged changes in slope of the mean 2 m air temperature for 12 projection intervals (6 years each) for the period 2020-2093 based on the MPI-ESM projection with scenario SSP5-8.5. The vertical lines indicate the transition between the seasons.

Looking at the weekly slopes over the entire period of the 2020-2093 projection, a warming can be observed over the entire year with 0.046 K/yr (Figure 33). The warming is greater in winter than in summer, with a drop in warming at the end of the year at the time of the polar night. It seems to be a clear distinction between the different seasons: summer has the lowest slope, followed by fall, spring and winter (Figure 33).

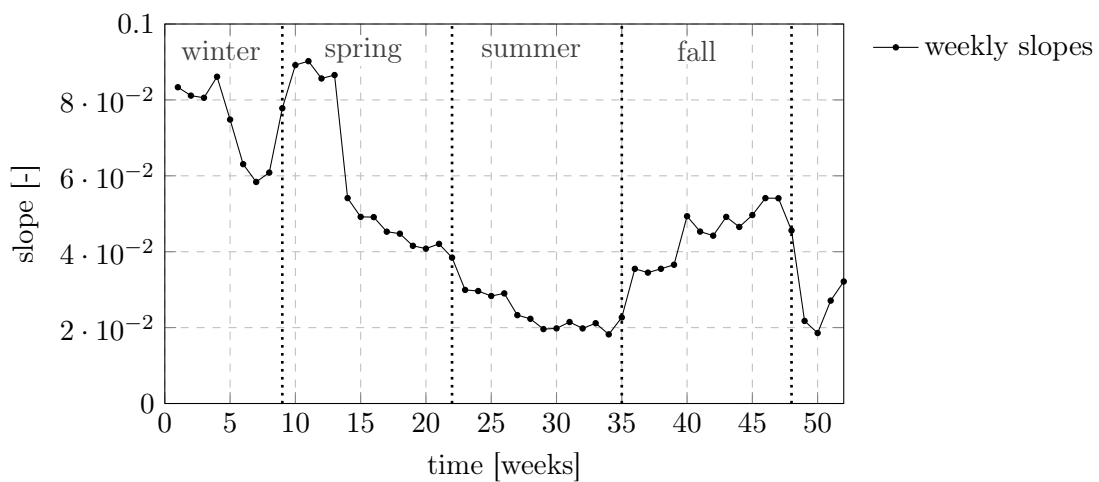


Figure 33: Weekly averaged changes in slope of the mean 2 m air temperature for projection period 2020-2093 based on the MPI-ESM projection with scenario SSP5-8.5. The vertical lines indicate the transition between the seasons.

### 4.1.2 Snowfall

To investigate snowfall, I examine the accumulated snowfall over one season (Figure 34), whereby the season between 1<sup>st</sup> of August and 31<sup>st</sup> of July of the following year is considered. The accumulated snowfall is the sum of the snowfall over one season which represents the positive changes in snow depth since snow depth contains also portions of compression, compaction, sublimation, evaporation and blowing. The forcing data set with ERA5 and MPI-ESM extends from 1980 to 2093, whereas the DMI data is only available for nine seasons between 2012 and 2020. First, I standardise the units, as the forcing data are provided as snowfall rate in  $[\text{kg m}^{-2} \text{s}^{-1}]$  and the weather station data as snow depth  $[\text{m}]$ . Accordingly, I sum the forcing data and take the sum of the positive changes of the measured snow depth data. In Figure 34 I observe that the data for the short comparison period fit each other well. The forcing data show an decreasing trend, i.e. the amount of snow per winter is decreasing during the 21<sup>st</sup> century with variations in the ERA5 reanalysis data of over 3 m and up to 1.5 m in the MPI-ESM projections.

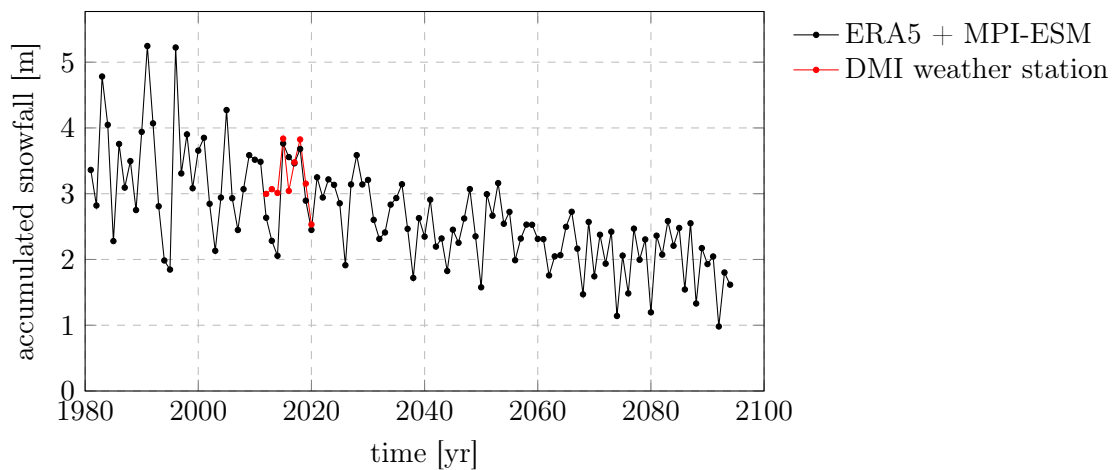
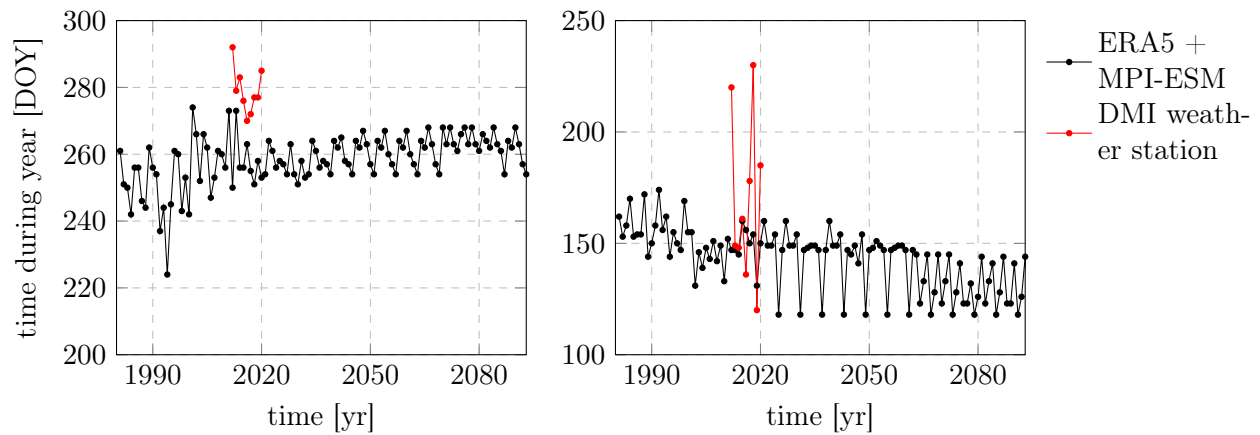


Figure 34: Accumulated snowfall per season from August, 01<sup>st</sup> to July, 31<sup>st</sup> for the climate forcing ERA5 + MPI-ESM and the weather station from DMI.

To look at the snowfall period per winter, I analyse the first and last day of snowfall within a season (01<sup>st</sup> of August - 31<sup>st</sup> of July). For the comparable period of the DMI and ERA data, the forcing data are only subject to minor fluctuations (Figure 35a). For the years between 2012 and 2020, the first snowfall is recorded in September, whereas the DMI data fluctuate between 3<sup>rd</sup> of August and 19<sup>th</sup> of October. Snow depths as shallow as 1 cm are recorded as the start of the season, even if it is a singular event and no snow falls for four weeks afterwards. In the projection period I observe that the first day of snowfall is always in September and is subject to fluctuations of a maximum of three weeks (Figure 35a). There is no discernible trend towards a later snowfall period.

For the last day of the season, DMI records show data between 30<sup>th</sup> of April and 28<sup>th</sup> of July, but mostly between mid-May and early July (Figure 35b). The ERA reanalysis data for the same period are comparatively stable, fluctuating only between 11<sup>th</sup> of May and 9<sup>th</sup> of June (Figure 35b). The projections, on the other hand, fluctuate strongly between 28<sup>th</sup> of April and 9<sup>th</sup> of June, whereby the six-year cycle with early cuts is recognisable. Overall, I observe a trend towards a shorter snow period due to an earlier date of the last snowfall. As the first day of snowfall is relatively stable and the last day tends to be earlier in the year, the snowfall period is shortened by two to four weeks

within the current century.



(a) First day of snowfall [DOY] for the climate forcing ERA5 + MPI-ESM and the weather station from DMI.

(b) Last day of snowfall [DOY] for the climate forcing ERA5 + MPI-ESM and the weather station from DMI.

Figure 35: First and last day of snowfall [DOY] for the climate forcing ERA5 + MPI-ESM and the weather station from DMI.

## 4.2 Ground thermal regime

In this section, I compare the results of the borehole data with air temperature as well as a simple one-dimensional model run for the tundra tile. Furthermore, I show the temperatures of the iButton sensors and local differences due to their position relative to the road.

### 4.2.1 Boreholes

There are some boreholes from the old airport investigation from the late 70s and early 80s on the existing runway and access road to the airport. Manual temperature profiles are made there (see Appendix B). As expected, these show larger fluctuations in the upper layers. For borehole 79012, for example, the temperature varies between  $-8.3^{\circ}\text{C}$  and  $-0.7^{\circ}\text{C}$  depending on the season. With increasing depth, temperatures become more stable and only fluctuate within one degree. In summer, an AL is present. Comparative borehole ground temperatures are used with air temperatures from ASIAQ for Ilulissat (Figure 36). Here the period between July 1<sup>st</sup>, 1980 and April 30<sup>th</sup>, 1981 is considered. The measurements at 1.5 m depth reflect the air temperatures with strong attenuation by the overlying soil. The seasonal variations of 7.6 K are relatively large for this depth. In addition, a temporal shift within the year can be observed, as the cold temperatures first cool and freeze the upper layers before a depth of 1.5 m is reached. The same effect is observed for the transition from winter to summer. The intervals between measurements are about 15 days and are thus not particularly dense, which leads to further smoothing.

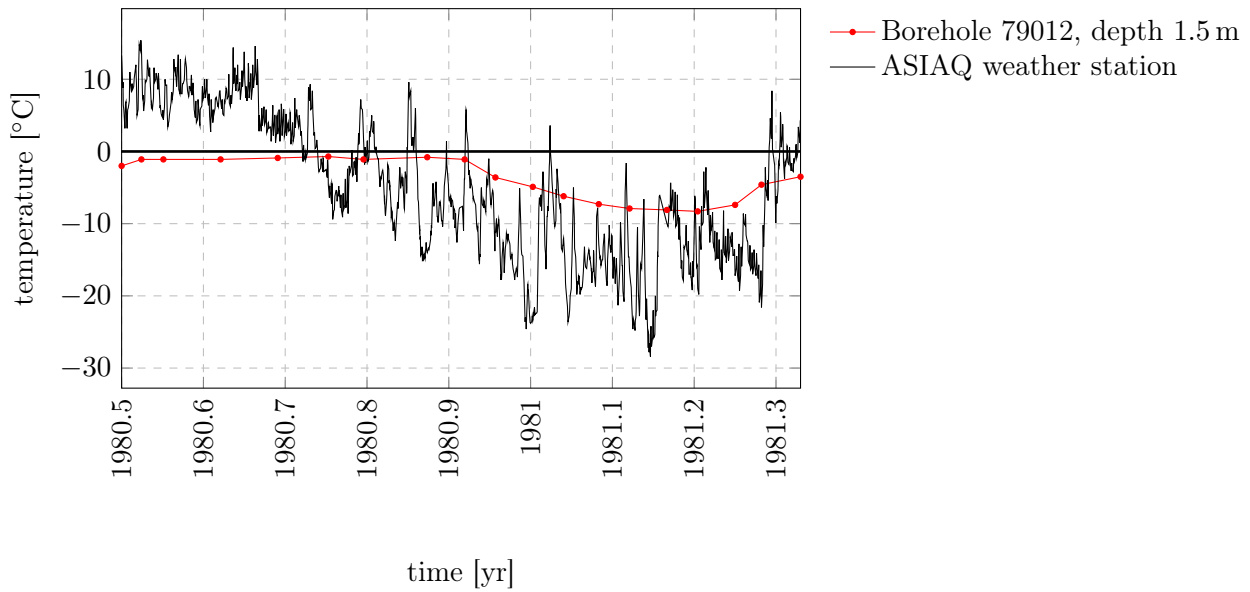


Figure 36: Comparison between the air temperature in Ilulissat and the temperature at 1.5 m depth in borehole 79012 from the ASIAQ database from 1st of July 1980 to 30th of April 1981.

I performed a similar comparison for the newer borehole ILU2018-03, which is located in the city. As with the old borehole, a smoothing of the curve with increasing depth as well as the temporal shift of the ground response to the air temperature is shown (Figure 37).

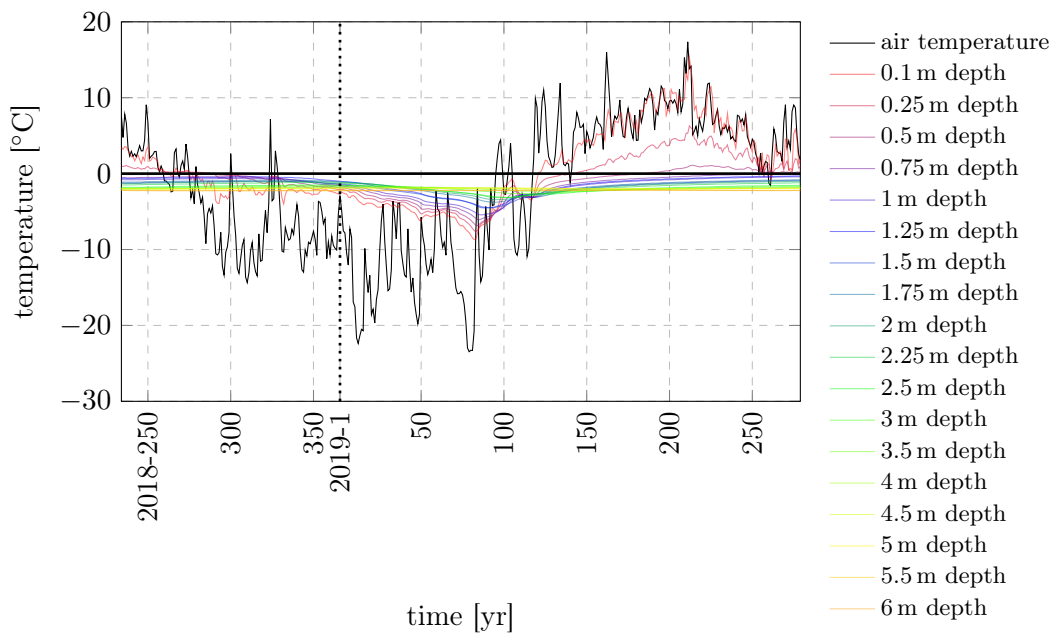


Figure 37: Comparison between the air temperature in Ilulissat and the temperatures per depth in borehole ILU2018-03 from DTU between 22<sup>nd</sup> of August 2018 and 6<sup>th</sup> of October 2019.

The borehole ILU2018-03 is located in the centre of Ilulissat (Figure 17) just a few metres from

the road (Figure 38) and is below  $0^{\circ}\text{C}$  all year round from 80 cm depth, suggesting permafrost at this location (Figure 37). The AL is therefore above that depth. The average temperature shows a clear trend towards positive temperatures and a shift of the entire trumpet curve towards positive temperatures (Figure 38). There is a noticeable anomaly in the temperature curve from 1.2 m to 1.6 m, indicating a layer boundary and the presence of excess ice. Due to the higher proportion of ice or the changed material properties, the transfer of temperature to deeper layers is delayed. The temperature of the ZAA is  $-2^{\circ}\text{C}$  at about 4.5 m depth for this borehole. The permafrost temperature is  $-2.2^{\circ}\text{C}$  in 2018-2019.

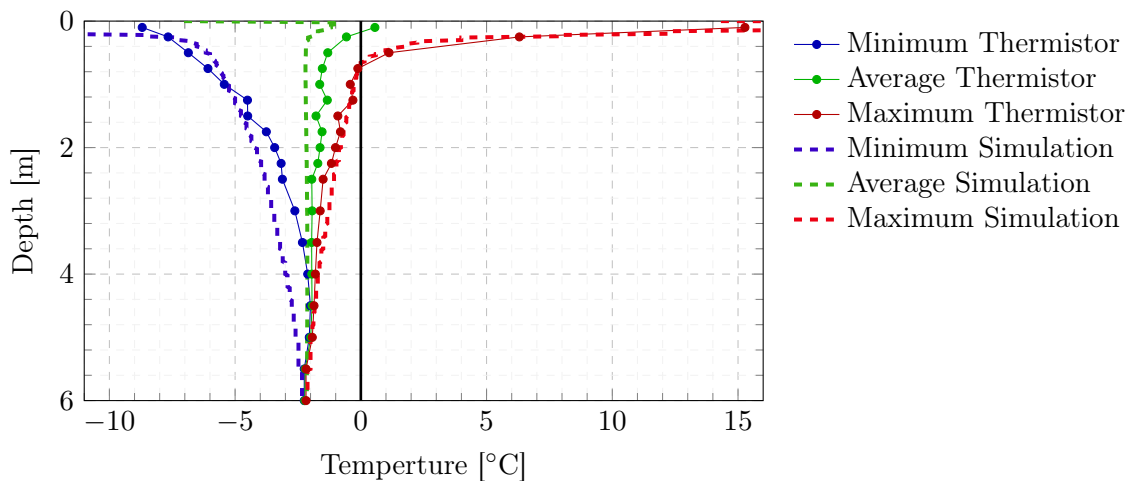


Figure 38: Temperature distribution of borehole ILU2018-03 (conducted by DTU) for the period from October 2018 to September 2019 as well as simulated ground temperatures with CryoGrid based on a single tundra tile with the properties of scenario a)

By looking at the temperature trumpet plots of some other boreholes (see Appendix C) and the layers from the borehole logs, I observe AL variations between 80 and 100 cm in areas with peat and clay (based on borehole logs from Ingeman-Nielsen, Scheer & Tomaškovičová (2022)). In boreholes with sand and moraine silt, the AL ranges between 150 cm and 190 cm, which can be explained by a different behavior in terms of capillarity due to the coarser grain structure. Another reason would be that these layers have lower water content which results in a thicker AL.

These borehole temperatures are used to validate the model. For this purpose, I perform a one-dimensional run with a tundra tile with the properties of the standard scenario and plotted the max., mean and min. temperatures in comparison (Figure 38). It turns out that the maximum temperatures of the trumpet plot match very well. For the min. temperatures, the model estimates them to be slightly too cold and with a stronger gradient, which is much smoother in the measured values. Consequently, the mean values are also a bit too cold, especially in the near-surface region. The bending behavior with the shift to warmer temperatures is comparable, only slightly shifted. Overall, the thermal regime of the model and the borehole in the field agree well with each other.

### 4.2.2 iButtons

From the measurements of the iButton sensors, both the ground surface temperature for Ilulisat and the effect of snow as an insulator for the near-surface soil are determined. The location of the iButtons is shown in subsection 3.2.2. For location 1 on the road towards the airport, where significant snow piling is observed in winter, four sensors measured over two years and one sensor measured over one year. Another sensor did not provide any data (Figure 20). The corresponding temperatures are shown in Figure 39a. In summer there are high fluctuations due to the influence of air temperature. In winter (around November to May), the temperature curve is clearly smoothed, whereby high fluctuations still occur at the beginning of the freezing period and smoothing occurs from around December or January. It can be assumed that initially there is no or only a thin snow cover, so that air temperatures have a large influence. As the snow cover increases due to natural snowfall or ploughing or storage of snow, the sensor becomes isolated and provides a smoothed temperature curve. Despite similar conditions, temperature differences of up to 7 K occur for the snow-insulated months (Figure 39a). The sensors 4C-D46, DE-814 and 61-ACF show a similar course and are located at the toe in close proximity to the road. Sensor B2-044 is located somewhat further away from the road and also shows a different picture in the temperature curve. I observe that all sensors in the thaw zone experience a stagnation at 0 °C, which is the zero curtain effect. With this change of aggregate state from ice to water, the temperature curve is inhibited by latent heat release (Kelley & Weaver 1969). All sensors are correctly calibrated because the correspondence between the zero curtain and the freezing point at 0 °C are overlapping.

For location 2, a similar course is observable. The sensors ED-3D0 and 96-B21 are located in the northern section with lateral snow ploughing near location 1 and the other sensors in the southern section with snow piling (Figure 19). The sensors ED-3D0 (black) and B1-116 (yellow) are further away from the road and thus from the influence of the ploughing than the other sensors (red, blue, cyan) (Figure 39b). This is shown in the temperature data, as these are lower in winter and are subject to greater fluctuations due to the air temperature. Furthermore, summer temperatures of the soil for neighbouring sensors differ greatly (up to 15 K difference). The reason for this lies in the differences in vegetation and the direction of the slope. D9-B8F and 47-FAE are in the toe near the road in the bushes and B1-116 is on the southfacing slope of a parking lot only slightly overgrown with bushes (Scheer 2019, 2020) and thus exposed to a thinner layer of vegetation and snow cover, resulting in temperatures that are more sensitive to external variations. These sensors also show the zero curtain effect at 0 °C (Figure 39b).

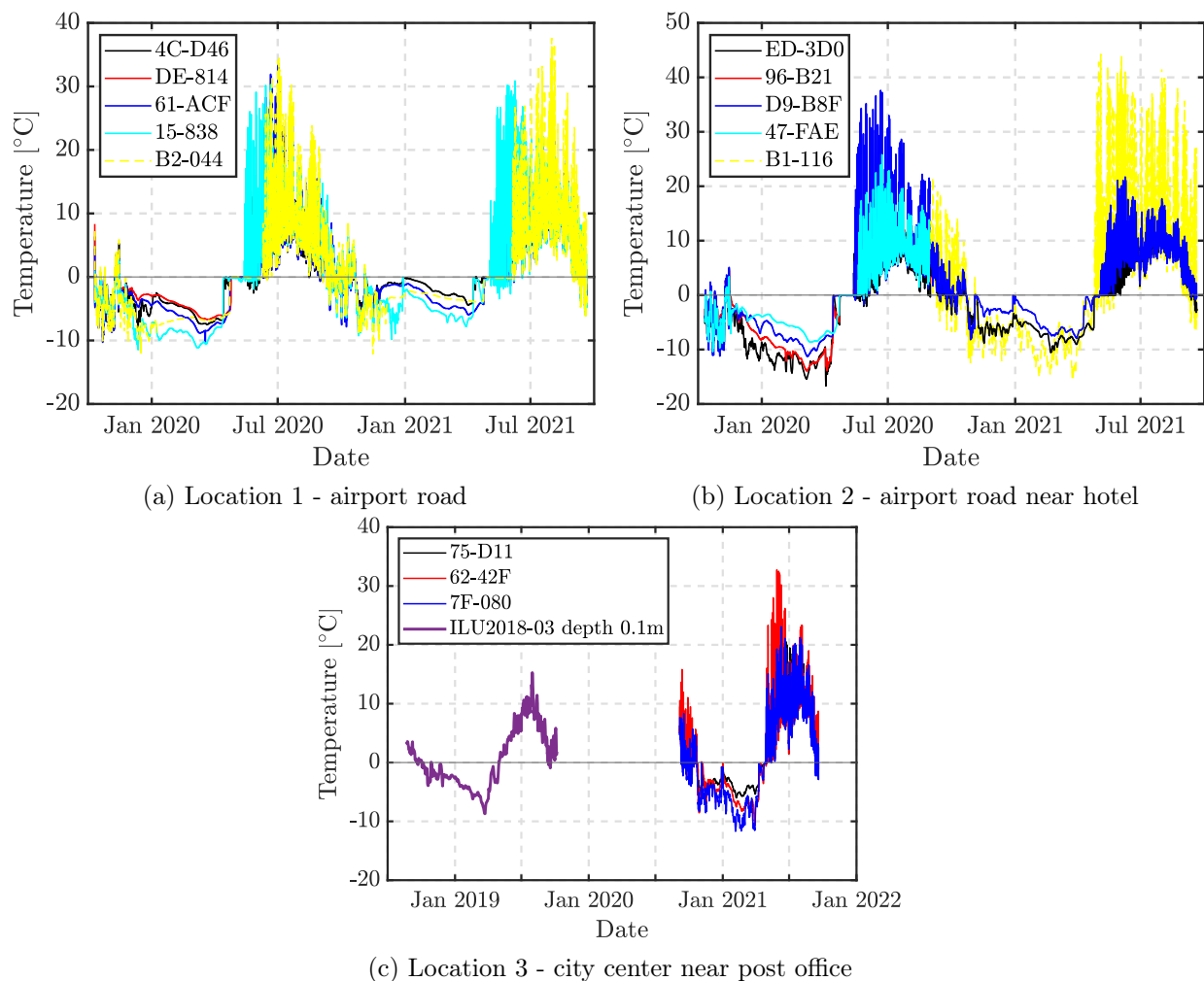


Figure 39: Ground surface temperature of iButton sensors in Ilulissat for three selected roadside locations and their snow accumulation effect.

At the 3<sup>rd</sup> location, three one-year measurements of the iButton sensors are present as well as the borehole ILU2018-03 is located a little further away from the road in the immediate vicinity. This part of the road is affected by damage and poor drainage. Furthermore, lateral snow ploughing is practiced (Figure 19). There is a clear difference between the temperature behaviour in summer and winter for this site (Figure 39c). In summer, almost all variations of air temperature are taken over for the surface of the ground, whereby these sensors are in the bushes, thus showing up to 10 K temperature difference even at a distance of about 60 m. In winter, the smoothing by insulating materials such as snow is shown (Figure 39c). Sensor 75-D11 (black) experiences the strongest influence of snow and sensor 7F-080 (blue) is the least influenced, experiences larger fluctuations and registers colder temperatures. This indicates that there is less snow in winter. Compared to the data from borehole ILU2018-03, the annual pattern strongly resembles the iButton temperatures. However, it should be noted that the borehole data are from a thermistor located 10 cm below the surface and are therefore already somewhat smoothed (Figure 39c). The near-surface temperature of the soil is up to  $-10^{\circ}\text{C}$  in winter and up to  $30^{\circ}\text{C}$  in summer at the southfacing slope.

### 4.3 CryoGrid model runs

Now that the validation of the forcing data as well as the soil temperatures are completed, the model runs are performed with the road structure. First, I show the results of the investigation of the initialization bias and then I present the results of all scenarios described in subsection 3.4. The focus is on the thermal regime with maximum thaw depth (MTD), trumpet plots, and the distribution of simulated ground temperatures.

#### 4.3.1 Initialization bias

I used the 10-year repeating forcing data set of the ERA5 reanalysis data for the Ilulissat site to determine the initialization bias. In addition, the temperature data in Table 1 serve as the ground temperatures at the beginning of the simulation in 1980. The values are based on data from thermistor measurements at different boreholes (Table 2), where I use a mean value and estimate the temperatures at greater depths ( $> 10$  m) respectively taking into account the influence of the thermal gradient.

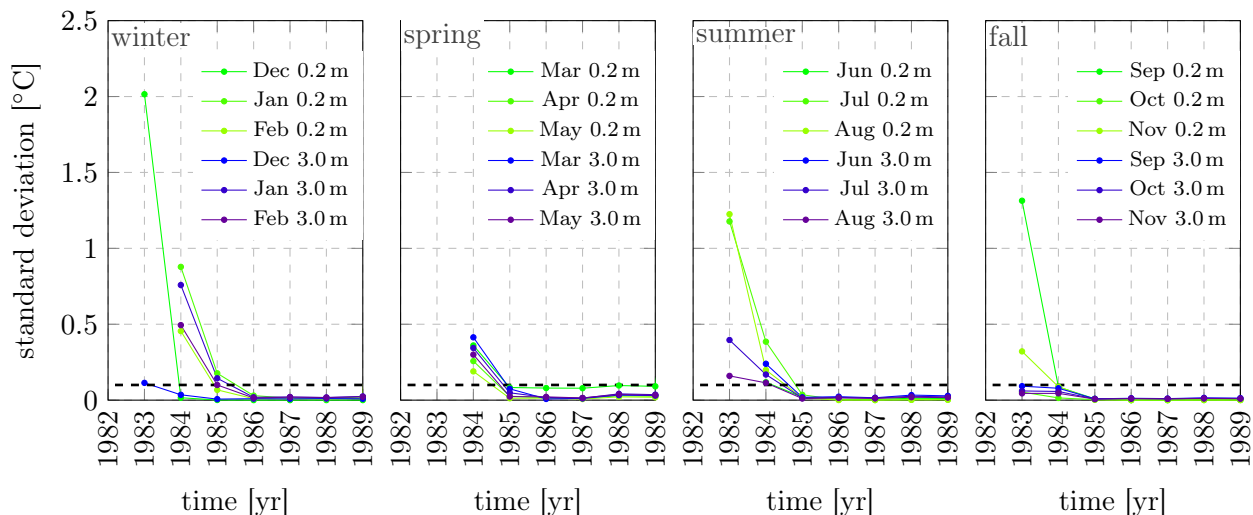


Figure 40: Standard deviation for the initialization bias for the depth 0.2 m (active layer) and depth 3.0 m (permafrost) trough out the year (winter, spring, summer, fall). The dashed line indicates the assumed maximum standard deviation of  $0.1$  °C.

I determine the initialization bias using standard deviation, whereby I use the simulated ground temperatures at two depths: 1. at  $-0.2$  m in the AL and 2. at  $-3.0$  m in the permafrost. In each case, a day at a certain time is compared with the exact same date/time of the following year, with the external influences being identical (at least over 10 years). This is repeated monthly for both depths (Figure 40). I choose the comparison period for the standard deviation to be four years after testing several time spans. The dataset starts in 1980 and the end of the comparison period is given in the Figure 40. Those figures clearly show that the standard deviation starts with different values depending on the season and depth, but at a maximum of  $2.02$  °C. In the following comparison periods, it decreases significantly and ends at below  $0.1$  °C after six years at the latest for all cases examined. This means that the influence of the initialization bias is only very small from about 1986. Since the forcing data set repeats only for the first 10 years, the standard deviation would

again become larger from 1990 onward due to annual fluctuations. For the further investigations, the data from 2000 onwards are considered, so that it can be assumed with a very high degree of probability that only the forcing data have an influence on the simulated development.

#### 4.3.2 Scenario a) Standard scenario

The standard scenario a) has double snow on shoulder and toe, a gravel road and no excess ice (Figure 23). For the visualization of the results, I calculate the MTD for all tiles first. To realize this, I first determine the thaw depths at each point in time (black line in Figure 41). This is the point where the first negative temperatures occur starting from the top of the terrain (Figure 41). Those thaw depths of the structural units are initialized at terrain depth, which means that the additional 1.1 m for the elevated road structure and 0.5 m for the shoulder are neglected and would count on top of the MTD. After analyzing all ground temperatures the maximum value of depth within a yearly cycle is taken (red line in Figure 41). Figure 41 shows a tundra tile from scenario a) and is done equally for all tiles. To smooth the noise of the signal I use a moving mean over a period of five years. The results of the MTD (thin lines) and the corresponding moving means (thick lines) are shown in Figure 42. These are displayed in different colours depending on the tile, whereby the colours are retained for all scenarios. In addition, comparative trumpet plots for road and tundra are created (Figure 43 and 44). These are used for the observation of the ground thermal regime.

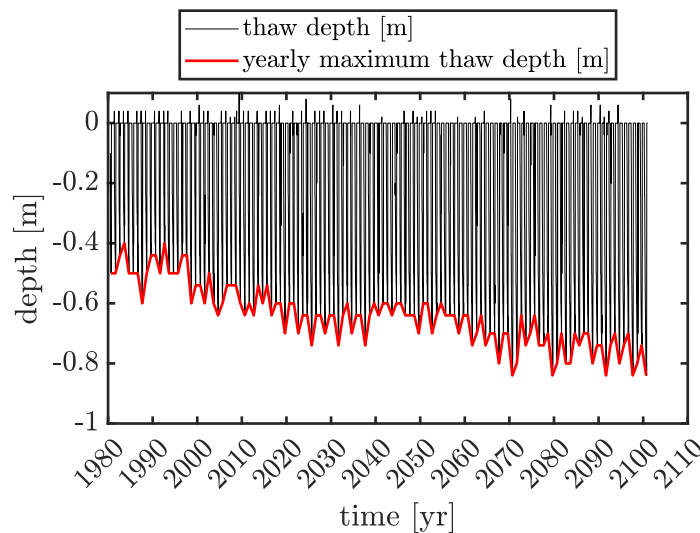


Figure 41: Simulated temporal evolution of thaw depth (black) with the indicated yearly maximum thaw depth (red) for the tundra tile in the scenario a).

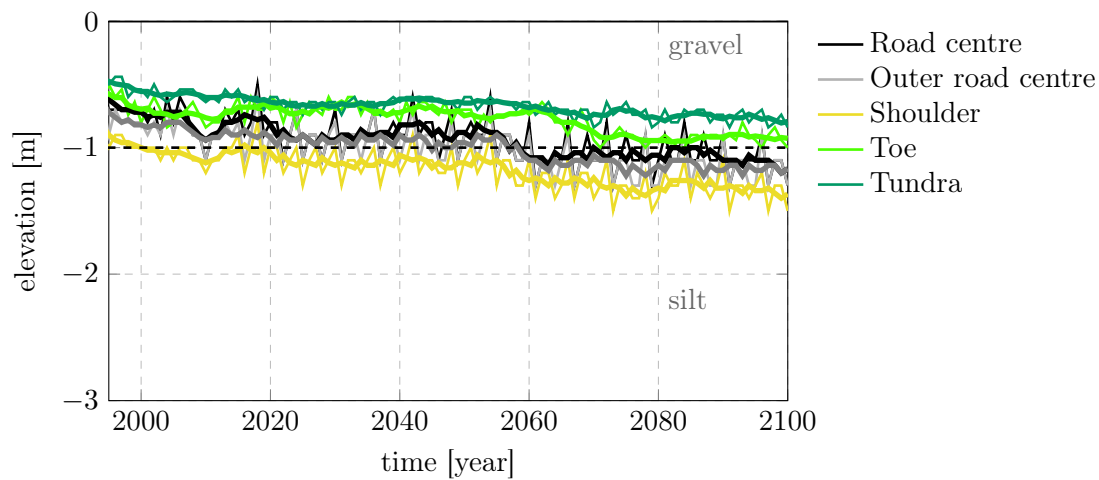


Figure 42: Simulated temporal evolution of maximum thaw depth (MTD) for all structural units with annual means (thin lines) and 5-year moving means (thick lines) for standard scenario a). The dotted line represents the lower boundary of the gravel layer and all elevations are referenced to the tundra surface.

The MTD (Figure 42) for the tiles with gravel on the surface (road and shoulder) increase by 38 cm to 42 cm over the time from 2000 to 2100, thus increasing the AL by this amount. Figure 43 shows the same change in the AL. The other two units toe and tundra indicate a less strong thaw process with about 25 cm increase of the AL for the same period. The temperature of the permafrost varies between  $-2.6^{\circ}\text{C}$  and  $-3.6^{\circ}\text{C}$  for the tiles road and tundra respectively at a depth of 10 m in 2000 (Figure 43 and Figure 44). A warming of 1 K to  $-1.6^{\circ}\text{C}$  to  $-2.6^{\circ}\text{C}$  over the period until 2090 is simulated. The trumpet plots (Figure 43 and 44) over the course of the depth mainly show a shift of the minimum temperatures towards warmer temperatures, whereas the maximum values change only minimally. The mean temperatures tend towards warmer conditions in the upper few metres. At the layer boundaries (dashed lines) the curves are not smooth but show anomalies, especially obvious from peat to silt (Figure 44, which are connected to the change of thermal properties (Figure 22, Table 6).

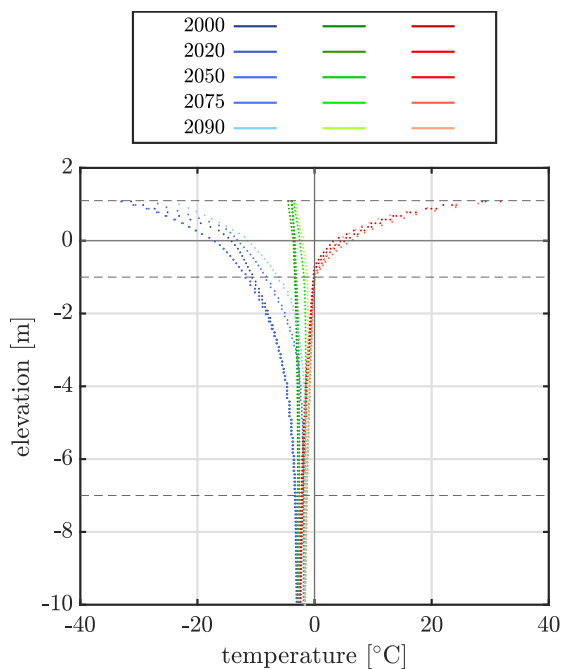


Figure 43: Modelled trumpet curve for road tile with max. (red), mean (green), and min. (blue) temperatures within the specified years 2000, 2020, 2050, 2075, and 2090 for standard scenario a). The dashed lines show the layer boundaries surface-gravel, gravel-silt, and silt-bedrock. The solid line refers to the tundra surface, thus the road is elevated above.

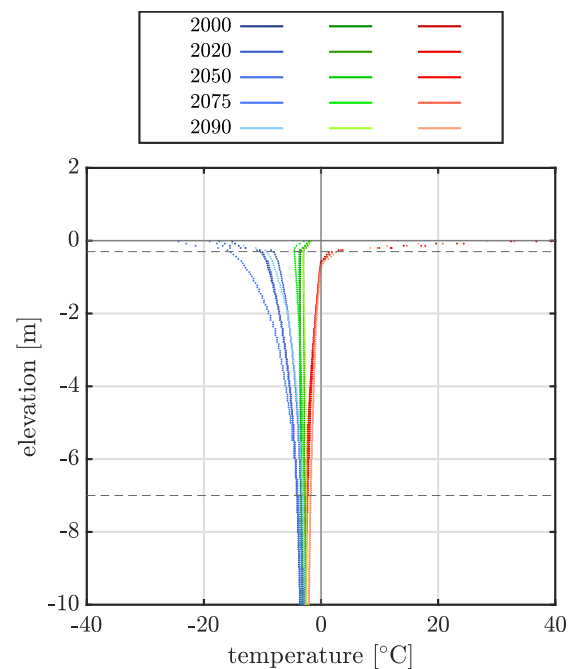


Figure 44: Modelled trumpet curve for tundra tile with max. (red), mean (green), and min. (blue) temperatures within the specified years 2000, 2020, 2050, 2075, and 2090 for the standard scenario a). The dashed lines show the layer boundaries peat-silt and silt-bedrock. The solid line refers to the tundra surface.

A further way of illustrating the thermal situation of the soil is presented in Figure 45, where I plot the temperatures per tile over depth at a given time. Here, the temperature distribution at the end of winter (March 1<sup>st</sup>) and summer (September 1<sup>st</sup>) is displayed for the years 2000, 2020, 2050, 2075 and 2090, respectively. The maximum and minimum temperatures near the surface show a warming of +2.5 K from 2000 to 2090 in winter, with an intermediate cooling by the middle of the 21<sup>st</sup> century. The opposite phenomenon is observed for summer. The simulation suggests a cooling of -1.5 K for the same period, with an intermediate warming here. The winter situations predict a decrease of the amount of snow during the current century, which is especially evident on the shoulder and toe units, since they received twice the amount of snow. Furthermore, the tiles shoulder and toe are warmer than the road and tundra for all observed dates in winter (Figure 45). Same tiles are below 1 m depth at nearly 0 °C for 2075 and 2090, this area is thus in the thaw process. The near-surface areas tend to be colder in winter, 2075 being a particularly cold year, and in 2090 a significant warming of the tundra tile is observed. For the situations at the end of summer, the AL can be clearly identified, with a growth over all tiles and an enhanced increase for road and shoulder observed over time. Initially, the thawed area remains within the gravel layer, but from 2050 onwards, especially the shoulder tile thaws slightly into the silt layer or is in the thawing process.

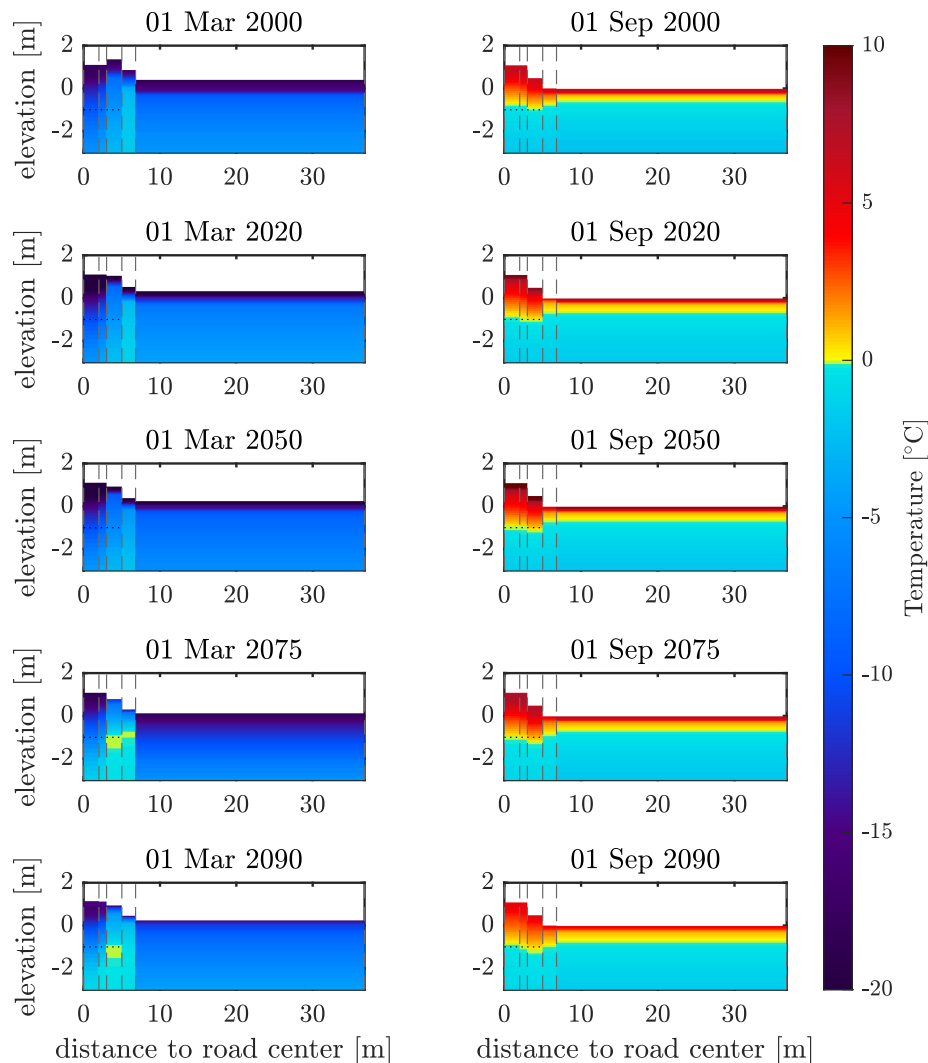


Figure 45: Simulated ground temperatures in the road, shoulder, toe, and adjacent tundra at the end of winter (left) and summer (right) for past (2000), present (2020), and future (2050, 2075, and 2090) climate conditions for the standard scenario a). The dotted line represents the lower boundary of the gravel layer.

### 4.3.3 Scenario b) Low road albedo

Scenario b) is identical in all parameters to scenario a) with the only difference that I change the albedo of the gravel for the two tiles of the road from  $\alpha = 0.3$  to  $\alpha = 0.1$  (Table 5). That represents a darkening of the surface. The AL has a starting depth in 2000 between 94 cm and 102 cm for the three tiles with gravel at the surface. The total thaw depth including the construction is simulated with 204 cm for the road and 152 cm for the shoulder. The toe starts at 70 cm and the tundra at 57 cm depth. By the year 2100, the increase of the AL is between 29 cm (toe) and 22 cm (tundra) for the area next to the road and between 39 cm (road) and 43 cm (outer road) for the tiles with gravel

on the surface (Figure 46). The permafrost temperature in 2000 is between  $-2.6^{\circ}\text{C}$  and  $-3.6^{\circ}\text{C}$  for the tile road and tundra respectively. It warms up by 1 K to  $-1.6^{\circ}\text{C}$  to  $-2.6^{\circ}\text{C}$  for the year 2090. A delayed/regressive trend as in the standard scenario a) (subsubsection 4.3.2) is observable for the middle of the 21<sup>st</sup> century (Figure 47 and 48). The trumpet plots show a similar behaviour with regard to the shifting and the anomalies at the layer boundaries as already described in scenario a).

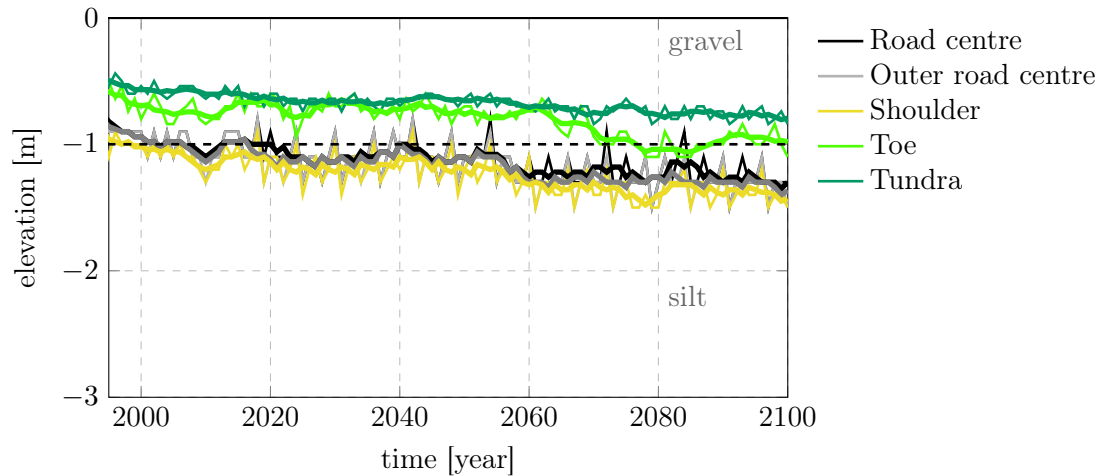


Figure 46: Simulated temporal evolution of maximum thaw depth (MTD) for all structural units with annual means (thin lines) and 5-year moving means (thick lines) for scenario b) with low road albedo ( $\alpha = 0.1$ ). The dotted line represents the layer boundary gravel-silt.

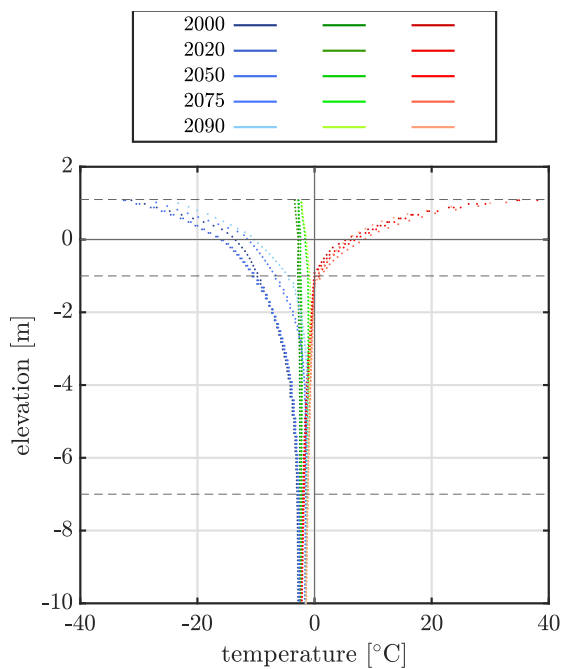


Figure 47: Modelled trumpet curve for road tile with max. (red), mean (green), and min. (blue) temperatures within the specified years 2000, 2020, 2050, 2075, and 2090 for scenario b) with low road albedo ( $\alpha = 0.1$ ). The dashed lines show the layer boundaries gravel-silt and silt-bedrock. The solid line refers to the tundra surface, thus the road is elevated above.

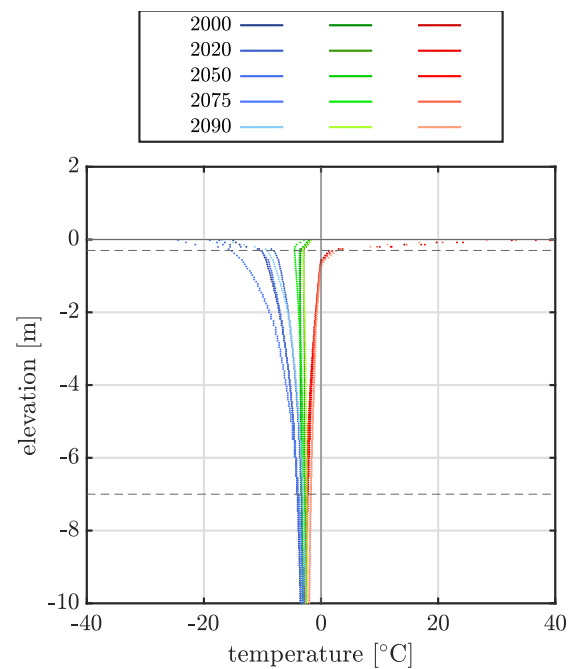


Figure 48: Trumpet curve for tundra tile with max. (red), mean (green), and min. (blue) temperatures within the specified years 2000, 2020, 2050, 2075, and 2090 for scenario b) with low road albedo ( $\alpha = 0.1$ ). The dashed lines show the layer boundaries peat-silt and silt-bedrock. The solid line refers to the tundra surface.

For the scenario with lower road albedo  $\alpha = 0.1$ , the ground temperatures at different times are plotted with the same resolution and time steps than the standard scenario a) (Figure 49). For the situations at the end of winter (March 1<sup>st</sup>), the surface is very cold due to the air temperature. For the year 2090, I observe a clear warming of these near-surface layers. This is consistent with the shifting of the minimum temperatures in the trumpet plot (Figure 47 and 48). For scenario b) a reduction in the amount of snow is observed mainly on shoulder and toe as well. These two tiles are the units that deliver the warmest temperatures. From 2075 onwards, the beginning of a talik formation is observed, whereby the ground is still in the thaw process, i.e. temperatures are a few hundredths below  $0^\circ\text{C}$ . This is localised between 1 m and 1.5 m depth and thus in the silt layer. An intensification is simulated from 2075 to 2090. The situations at the end of the summer (September 1<sup>st</sup>) show the AL and its increase over time. The gravel body of the road warms up a few  $^\circ\text{C}$  more due to the dark road, so that the thawing of the soil extends into the silt layer from 2050 onward. The gravel body thaws completely in summer and influences the adjacent soil layers. The silt layer underneath is slightly thawed and the adjacent toe tile is warmer with a deeper AL exceeding 1 m depth.

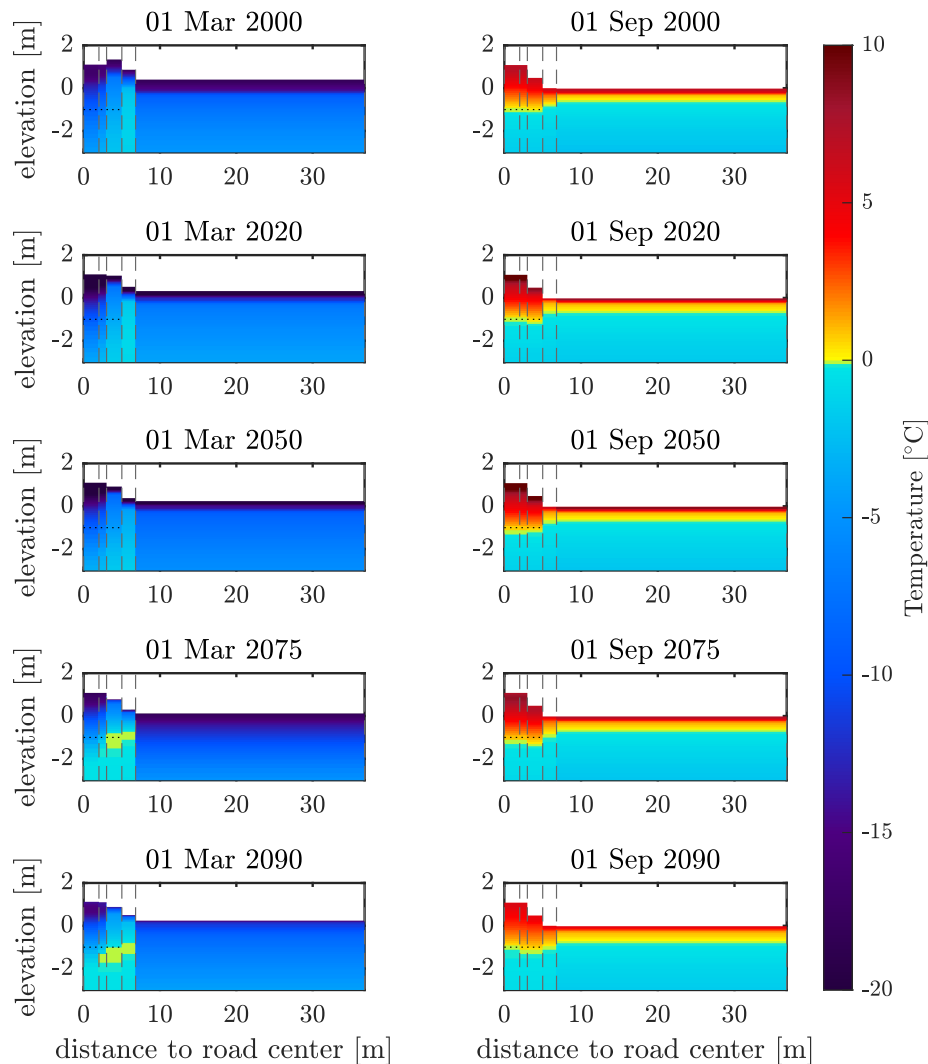


Figure 49: Simulated ground temperatures in the road, shoulder, toe, and adjacent tundra at the end of winter (left) and summer (right) for past (2000), present (2020), and future (2050, 2075, and 2090) climate conditions for scenario b) with low road albedo  $\alpha = 0.1$ . The dotted line represents the lower boundary of the gravel layer.

#### 4.3.4 Scenario c) Low road albedo and cleared embankment

In scenario c), clearing the shoulder from snow is added to the low road albedo  $\alpha = 0.1$  scenario b). The initial depth of the AL after initialisation in 2000 is between 84 cm (road) and 102 cm (shoulder) for the tiles with gravel. The two adjacent units have 60 cm (toe) and 52 cm (tundra) respectively (Figure 50). By the year 2100, an increase of about 25 cm is modeled for these tiles. The three tiles with gravel range between 32 cm and 40 cm increase in AL thickness. The temperature of the permafrost in 2000 is between  $-3.2^{\circ}\text{C}$  and  $-4.2^{\circ}\text{C}$  for road and tundra respectively. 100 years later, this has increased by about 1.2 K to a range of  $-2.0^{\circ}\text{C}$  to  $-3.0^{\circ}\text{C}$ .

The trumpet plots in Figure 51 and 52 show very similar behaviour in terms of branch shifting and the anomalies at the layer boundaries.

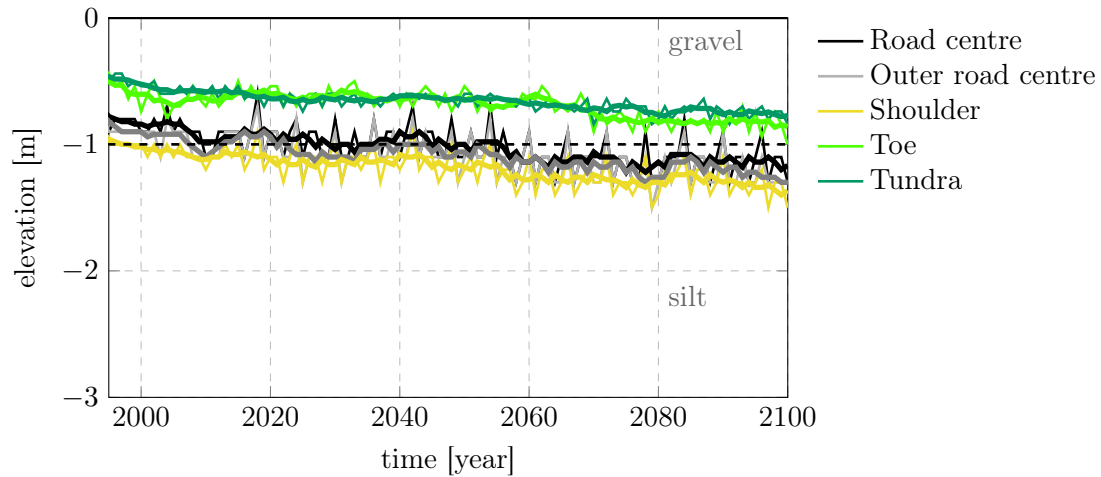


Figure 50: Simulated temporal evolution of maximum thaw depth (MTD) for all structural units with annual means (thin lines) and 5-year moving means (thick lines) for scenario c) with low road albedo ( $\alpha = 0.1$ ) and cleared shoulder. The dotted line represents the lower boundary of the gravel layer (0 to -1 m) and all elevations are referenced to the tundra surface.

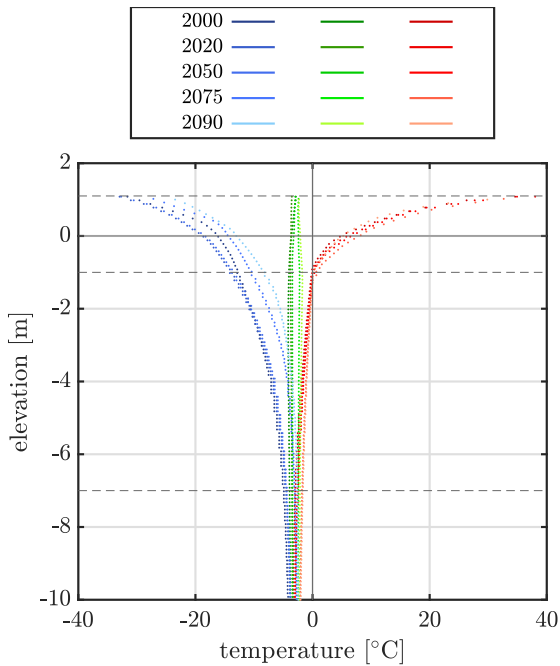


Figure 51: Modelled trumpet curve for road tile with max. (red), mean (green), and min. (blue) temperatures within the specified years 2000, 2020, 2050, 2075, and 2090 for scenario c) with low road albedo ( $\alpha = 0.1$ ) and cleared shoulder. The dashed lines show the layer boundaries gravel–silt and silt–bedrock. The solid line refers to the tundra surface, thus the road is elevated above.

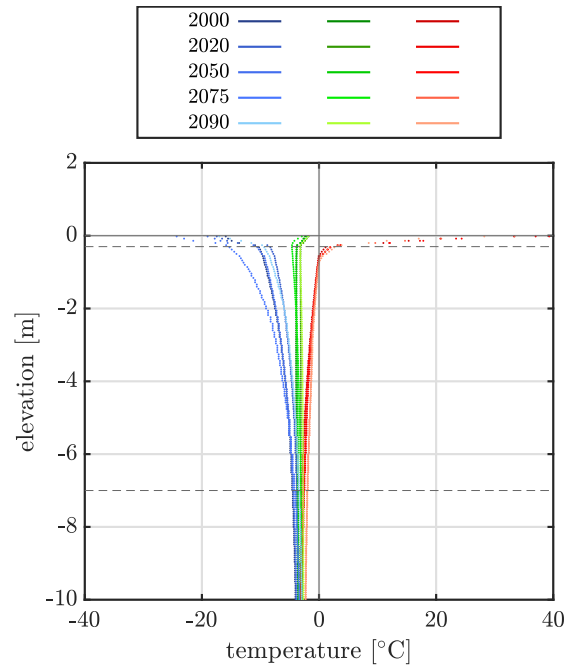


Figure 52: Modelled trumpet curve for tundra tile with max. (red), mean (green), and min. (blue) temperatures within the specified years 2000, 2020, 2050, 2075, and 2090 for scenario c) with low road albedo ( $\alpha = 0.1$ ) and cleared shoulder. The dashed lines show the layer boundaries peat–silt and silt–bedrock. The solid line refers to the tundra surface.

Figure 53 shows a changed behaviour compared to scenario b), especially in the winter time. The temperatures in the ground are almost constantly cold with below  $-15^{\circ}\text{C}$  until 2090 and especially for the units road and shoulder colder than the previous scenarios. For these tiles, the temperature is below  $-15^{\circ}\text{C}$  down to 70 cm depth. The surface reaches up to  $-32.9^{\circ}\text{C}$ . In contrast, the influence of snow is particularly evident as the toe tile receives twice the amount of snow and thus temperatures do not decrease as much in winter (Figure 53). The surface temperature of the toe tile decreases from  $-23.4^{\circ}\text{C}$  to  $-17.6^{\circ}\text{C}$  throughout the century. There, already after 26 cm, the temperature will no longer fall below  $-15^{\circ}\text{C}$ . As in the previous scenarios, the amount of snow decreases over time. No incipient talik formation is visible. The situation at the end of summer (September 01<sup>st</sup>) shows a slight increase in the AL thickness, although this is for all tiles a few centimeter less than in scenario b). Toe and tundra show almost the same behaviour and the area of the gravel body reaches the silt layer and leads to slightly positive temperatures up to a depth of 22 cm. Overall, the scenario with cleared embankment and lower albedo ( $\alpha = 0.1$ ) results in the ground remaining colder in winter. In summer, however, the AL still extends beyond the gravel layer into the silt layer.

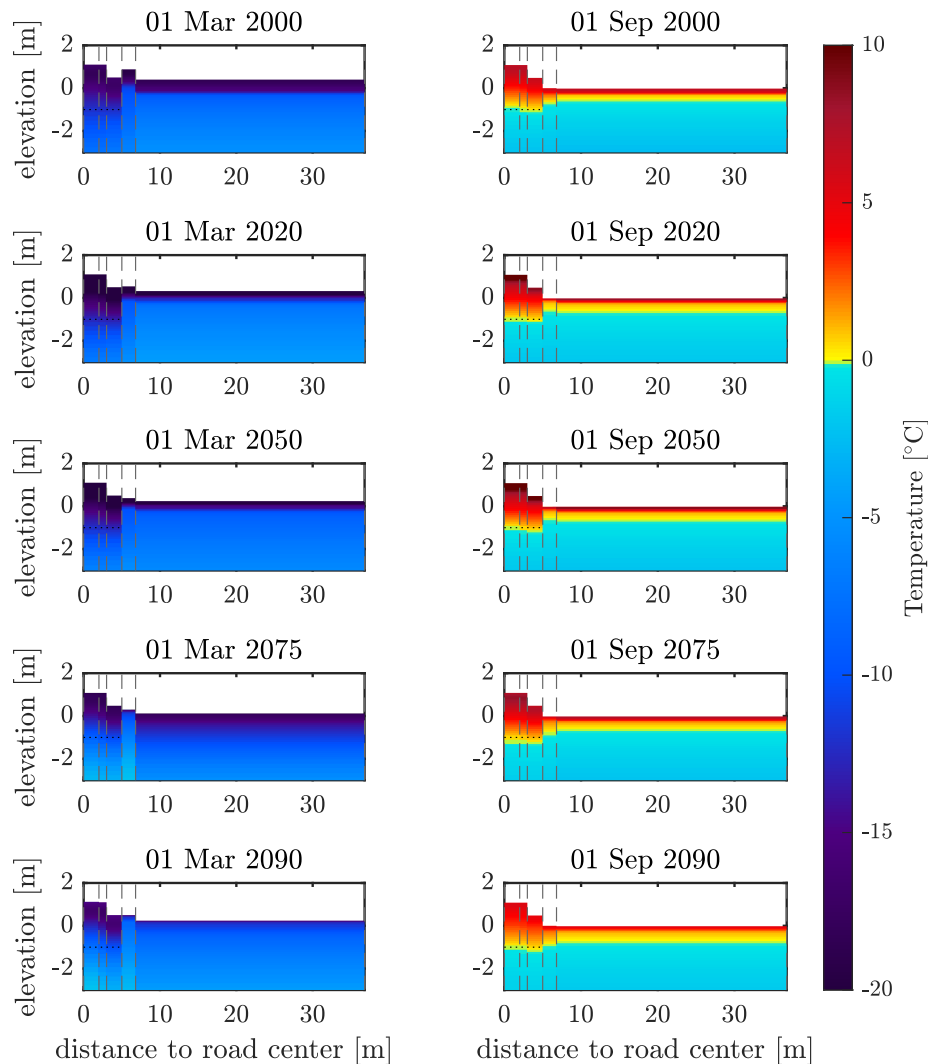


Figure 53: Simulated ground temperatures in the road, shoulder, toe, and adjacent tundra at the end of winter (left) and summer (right) for past (2000), present (2020), and future (2050, 2075, and 2090) climate conditions for scenario c) with low road albedo  $\alpha = 0.1$  and cleared shoulder. The dotted line represents the lower boundary of the gravel layer.

#### 4.3.5 Scenario d) Embankment cleared from snow

Scenario d) investigates the case when only the snow is removed from the shoulder compared to the standard scenario a) (Figure 24). The AL thickness after initialisation for the road is 64 cm (road centre) to 78 cm (outer road centre) (Figure 54). The shoulders AL thickness is at 102 cm and the adjacent units toe with 62 cm and tundra with 52 cm. Like in the previous scenarios the road structure would count on top of this. After 100 years of simulation, the road experiences about 40 cm AL increase, the shoulder 31 cm and toe and tundra with about 25 cm. The permafrost temperature in 2000 is between  $-3.3^{\circ}\text{C}$  and  $-4.4^{\circ}\text{C}$  for the road and tundra respectively. It increases

to a range between  $-2.2^{\circ}\text{C}$  and  $-3.0^{\circ}\text{C}$  by 2090.

The trumpet plots in Figure 55 and 56 are again strongly spread out for the minimum temperatures and staggered gradually warmer temperatures are simulated until 2090. The mean temperature tends towards positive temperatures. The maximum values change only minimally. The anomalies in the temperature curve are present at the layer boundaries (Figure 56).

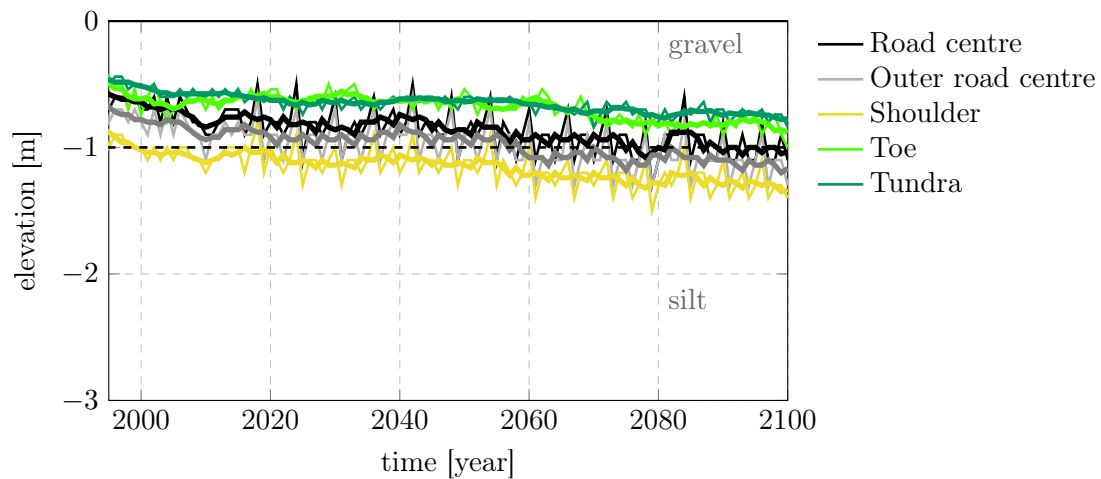


Figure 54: Simulated temporal evolution of maximum thaw depth (MTD) for all structural units with annual means (thin lines) and 5-year moving means (thick lines) for scenario d) with embankment cleared from snow. The dotted line represents the layer boundary gravel–silt and all elevations are referenced to the tundra surface.

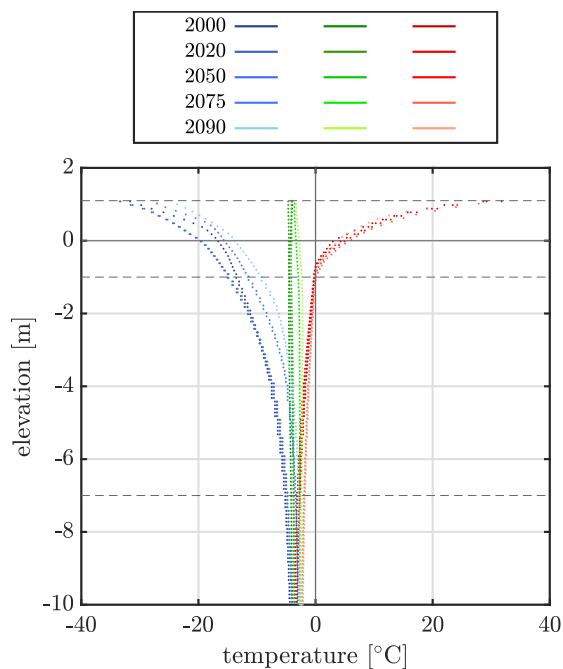


Figure 55: Modelled trumpet curve for road tile with max. (red), mean (green), and min. (blue) temperatures within the specified years 2000, 2020, 2050, 2075, and 2090 for scenario d) with shoulder cleared from snow. The dashed lines show the layer boundaries air–gravel, gravel–silt, and silt–bedrock. The solid line refers to the tundra surface, thus the road is elevated above.

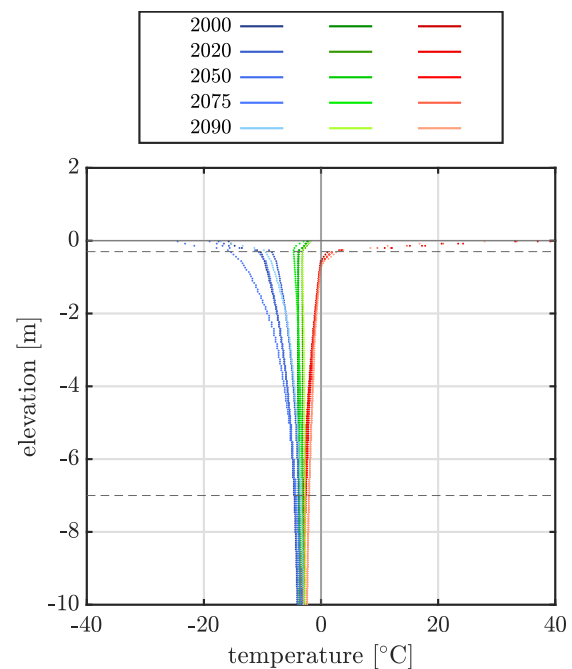


Figure 56: Modelled trumpet curve for tundra tile with max. (red), mean (green), and min. (blue) temperatures within the specified years 2000, 2020, 2050, 2075, and 2090 for scenario d) with shoulder cleared from snow. The dashed lines show the layer boundaries peat–silt, and silt–bedrock. The solid line refers to the tundra surface.

The simulated ground temperatures for this scenario are shown in Figure 57. At the end of winter (March 01<sup>st</sup>), the temperatures are predominantly very cold and especially in the road body they reach significantly deeper than in the adjacent silt layers of toe and tundra. A temperature of  $-15\text{ }^{\circ}\text{C}$  is ensured until the year 2090 for a depth of 86 cm (road) and 12 cm (tundra). The decrease in snow is observable for this scenario, although only for the tiles with snow (toe and tundra). I do not observe talik formations in this scenario until 2090. The situation at the end of summer (September 01<sup>st</sup>) in Figure 57 models an increase in AL thickness until 2090. That is similar to the previous scenarios. Here, the temperatures in the AL are several  $^{\circ}\text{C}$  cooler per depth compared to the previous scenarios. For the road, the ground thaws only in the gravel area up to 1 m below terrain level and just slightly touches the silt layer. For the shoulder unit, the ground thaws about 30 cm into the silt layer.

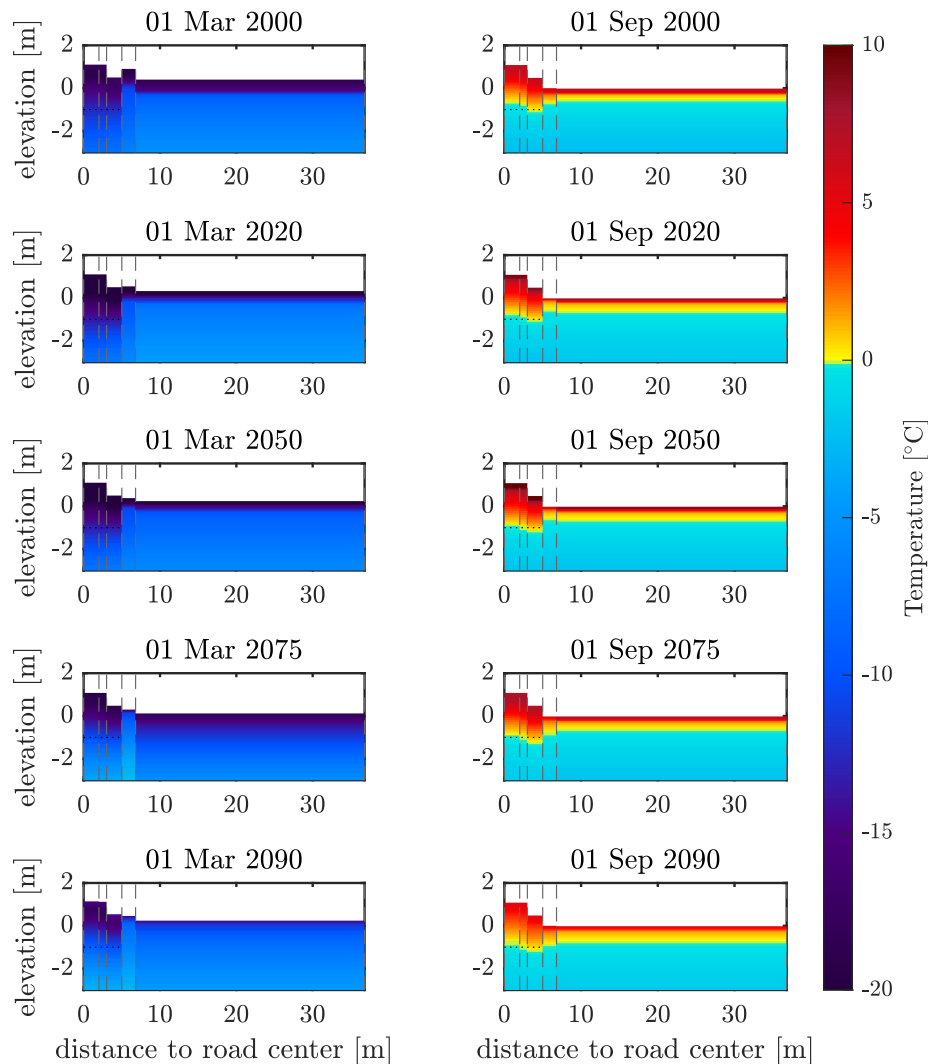


Figure 57: Simulated ground temperatures in the road, shoulder, toe, and adjacent tundra at the end of winter (left) and summer (right) for past (2000), present (2020), and future (2050, 2075, and 2090) climate conditions for scenario d) with the shoulder cleared from snow. The dotted line represents the lower boundary of the gravel layer.

#### 4.3.6 Scenario e) Changed gravel layer properties

In scenario e) the parameters thermal conductivity  $k_m = 1.5 \text{ W}/(\text{mK})$  and volumetric heat capacity  $c_m = 1.7 \times 10^6 \text{ J}/(\text{Km}^3)$  are adjusted for the mineral fraction, i.e. mainly gravel (Table 5). However, this changes the properties of silt and bedrock somewhat, since these have mineral components. The depth of the AL below terrain level after initialisation in 2000 is between 43 cm and 46 cm for the road, about 65 cm for shoulder and toe and 52 cm for the tundra (Figure 58). Road and shoulder have additional 1.1 m and 0.5 m respectively for the structure. By the year 2100, toe and tundra experience an increase of 19 cm. The gravel influenced areas are deepening between

34 cm (road) and 37 cm (shoulder). The permafrost temperature in 2000 for this scenario is between  $-2.7^{\circ}\text{C}$  and  $-3.9^{\circ}\text{C}$  for road and tundra respectively (Figure 59 and 60). By 2090 it warms by about 0.9 K to a range between  $-1.8^{\circ}\text{C}$  and  $-3.0^{\circ}\text{C}$ . The trumpet plots in Figure 59 and Figure 60 show the same trends regarding shifts and anomalies at layer boundaries.

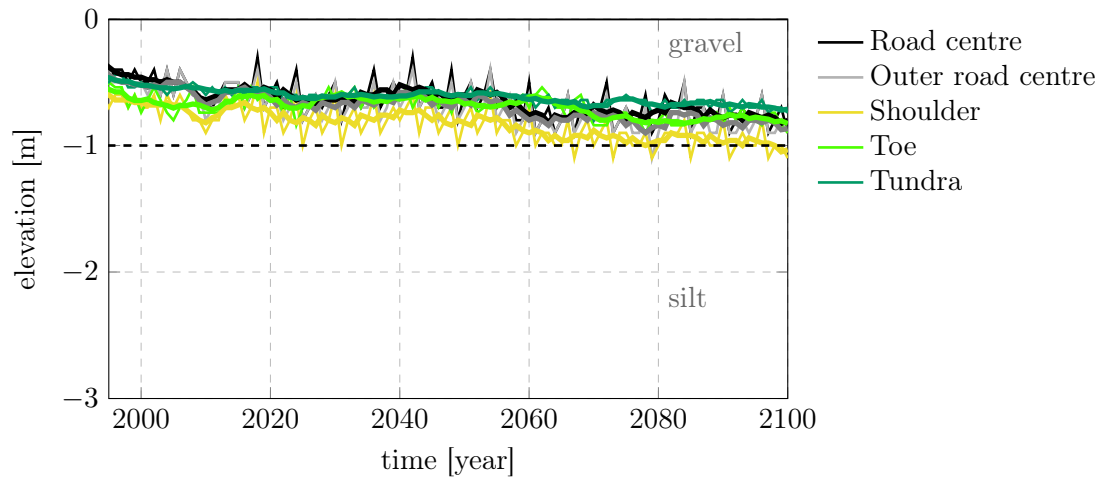


Figure 58: Simulated temporal evolution of maximum thaw depth (MTD) for all structural units with annual means (thin lines) and 5-year moving means (thick lines) for scenario e) with changed gravel layer properties. The dotted line represents the layer boundary gravel-silt and all elevations are referenced to the tundra surface.

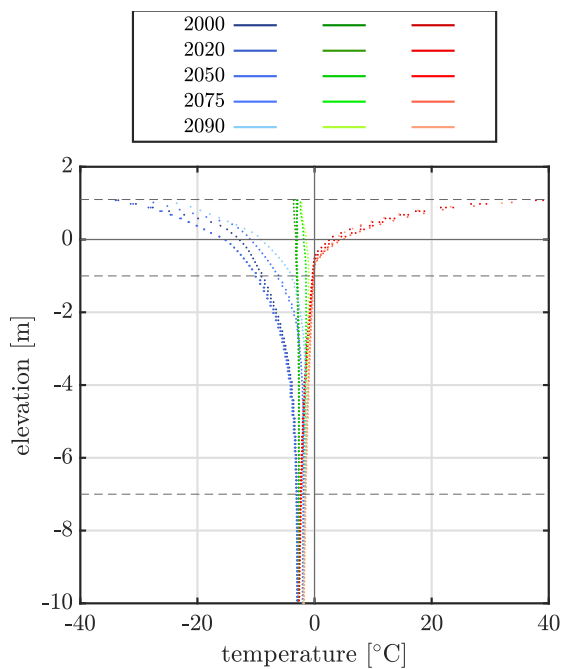


Figure 59: Modelled trumpet curve for road tile with max. (red), mean (green), and min. (blue) temperatures within the specified years 2000, 2020, 2050, 2075, and 2090 for scenario e) with changed gravel layer properties. The dashed lines show the layer boundaries air–gravel, gravel–silt, and silt–bedrock. The solid line refers to the tundra surface, thus the road is elevated above.

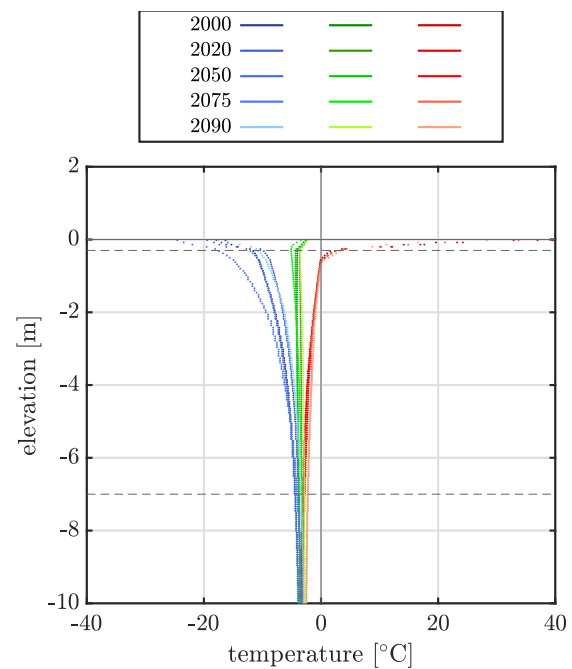


Figure 60: Modelled trumpet curve for tundra tile with max. (red), mean (green), and min. (blue) temperatures within the specified years 2000, 2020, 2050, 2075, and 2090 for scenario e) with changed gravel layer properties. The dashed lines show the layer boundaries peat–silt, and silt–bedrock. The solid line refers to the tundra surface.

For the simulated ground temperatures in Figure 61, the upper 10 cm (tundra) to 54 cm (road) are below  $-15^{\circ}\text{C}$  in winter. For the shoulder, the minimum temperatures are  $-8.6^{\circ}\text{C}$  below snow in 2000. These are declining with shrinking cover to  $-16.4^{\circ}\text{C}$  in 2090. For the toe, the minimum temperature is  $-6.0^{\circ}\text{C}$ . Especially below the road body and the adjacent toe, temperatures rise again relatively quickly and a dew bubble in the form of an emerging talik formation is already visible in the shoulder tile (Figure 61). In the summer situation (September 01<sup>st</sup>), the AL is identifiable, although at 64 cm (tundra) in 2090 it remains thinner than in the previous scenarios. The increase of the AL with time is recognisable according to Figure 58. However, the thaw depth for all tiles extends to a maximum of 1 m below terrain level, so that this occurs within the gravel layer and does not reach the silt layer until 2090. However, about 10 years later, in 2100 the AL has increased to about 5 cm into the silt layer (Figure 58).

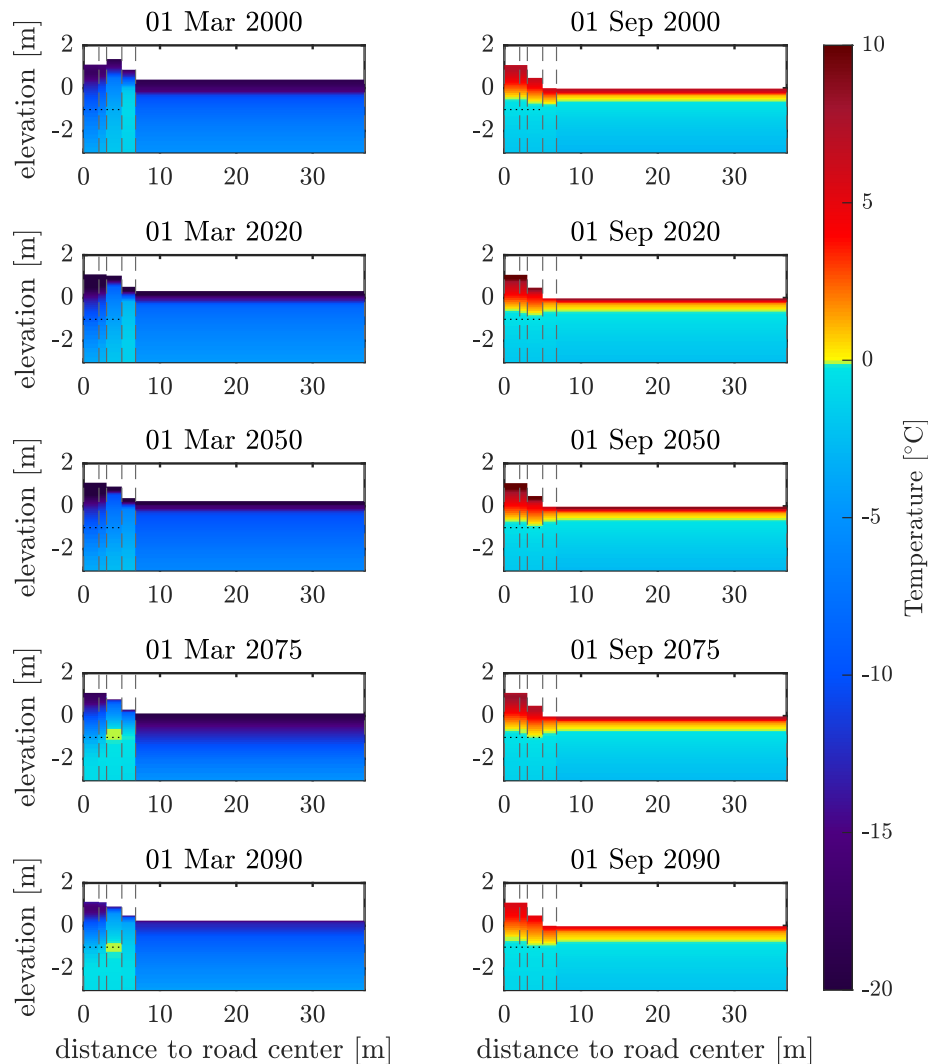


Figure 61: Simulated ground temperatures in the road, shoulder, toe, and adjacent tundra at the end of winter (left) and summer (right) for past (2000), present (2020), and future (2050, 2075, and 2090) climate conditions for scenario e) with changed gravel layer properties. The dotted line represents the lower boundary of the gravel layer.

#### 4.3.7 Scenario f) Excess ice

In scenario f), excess ice is assumed at a depth of 1 m to 2 m (Figure 25). The snow is present on shoulder and toe with double amount of the forcing input and the albedo is kept at  $\alpha = 0.3$ . After initialisation, the road is at 80 cm to 86 cm AL depth below terrain level and the shoulder at 105 cm (Figure 62). The units without gravel and with peat are between 72 cm (toe) and 61 cm (tundra). By 2095, the road increases by 45 cm to 58 cm, the shoulder by 80 cm and the tundra by 14 cm. In the toe, the largest AL increase occurs at 168 cm by 2095, with a large drop occurring from 2080. The occurrence of a pond from 2070 seems to play a role in this. The permafrost

temperature in 2000 is between  $-2.7^{\circ}\text{C}$  and  $-3.6^{\circ}\text{C}$  for road and tundra respectively (Figure 63 and 64) and increases to  $-1.4^{\circ}\text{C}$  to  $-2.5^{\circ}\text{C}$  by 2095. The tundra is several tenths  $^{\circ}\text{C}$  colder than the other tiles. The trumpet plots show the shifting of the minimum and mean temperatures to warmer areas. Furthermore, anomalies at the layer boundaries are observed, with an additional one at the boundaries of the excess ice at 1 m and 2 m depth.

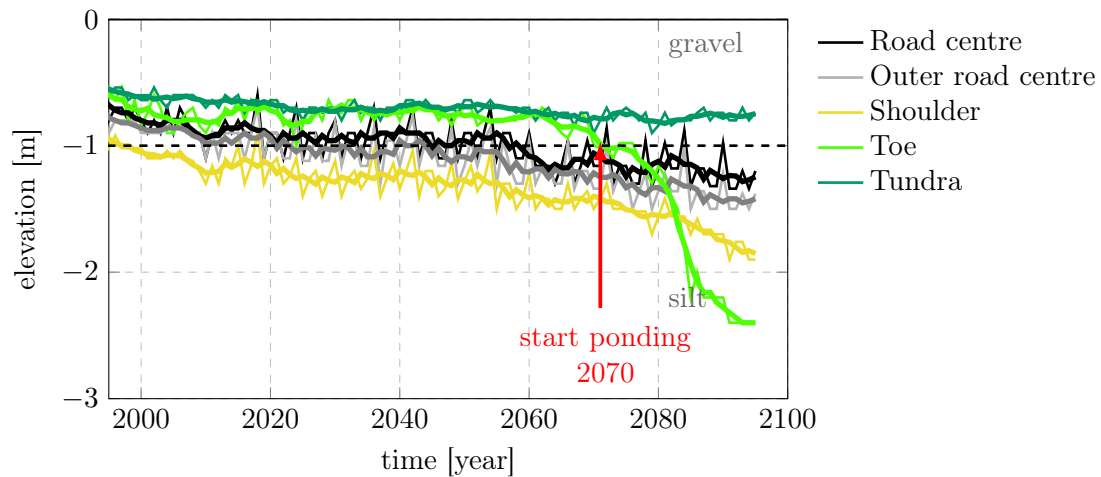


Figure 62: Simulated temporal evolution of maximum thaw depth (MTD) for all structural units with annual means (thin lines) and 5-year moving means (thick lines) for scenario f) with excess ice between  $-1$  and  $-2$  m. The dotted line represents the layer boundary gravel–silt and all elevations are referenced to the tundra surface.

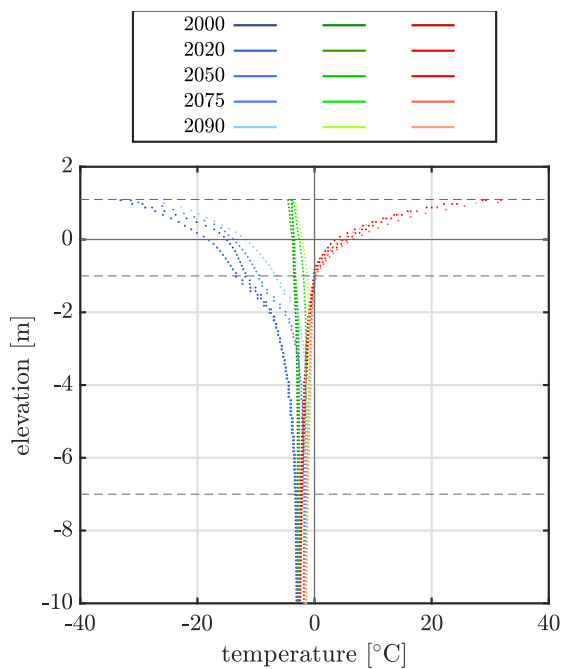


Figure 63: Modelled trumpet curve for the road tile with max. (red), mean (green), and min. (blue) temperatures within the specified years 2000, 2020, 2050, 2075, and 2090 for scenario e) with excess ice between  $-1$  and  $-2$  m. The dashed lines show the layer boundaries air–gravel, gravel–silt, and silt–bedrock. The solid line refers to the tundra surface, thus the road is elevated above.

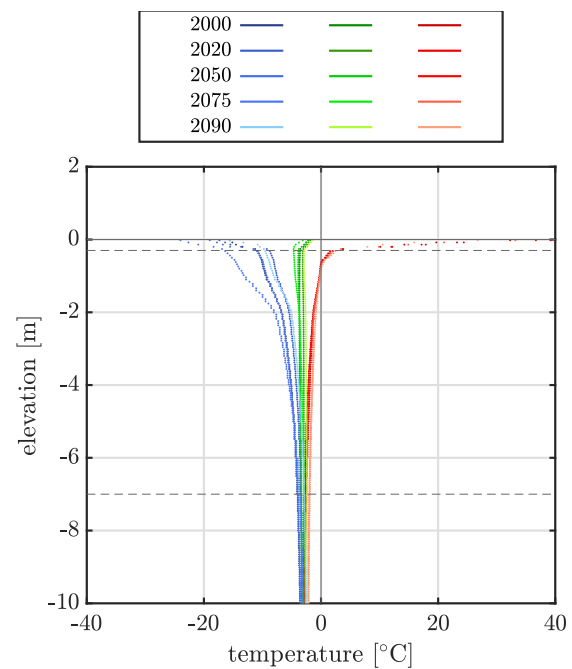


Figure 64: Modelled trumpet curve for tundra tile with max. (red), mean (green), and min. (blue) temperatures within the specified years 2000, 2020, 2050, 2075, and 2090 for scenario e) with excess ice between  $-1$  and  $-2$  m. The dashed lines show the layer boundaries peat–silt, and silt–bedrock. The solid line refers to the tundra surface.

With regard to the simulated ground temperatures in Figure 65, it can be seen for winter that although the surface temperatures are cold, as the time axis progresses the cold layer becomes thinner and thinner and a greater gradient towards warm temperatures develops. In 2020 the temperature at the surface of the road tile is below  $-30$  °C and staying below  $15$  °C up to the elevation of  $-60$  cm. By contrast, in 2090 these values are only reached up to  $+32$  cm, a difference of 92 cm. This applies similarly to shoulder and toe. Especially the toe is already about 4 K warmer than the surrounding tiles from 2000 onward. From 2075 onward, a beginning talik formation is observed, which increases significantly by 2090 and includes the outer road, shoulder and toe tiles. The talik is located beneath the gravel layer in the silt, including the excess ice layer and the silt underneath, that does not contain excess ice (Figure 65). The surface temperatures for shoulder and toe are cold only for a narrow area and become warmer than  $-10$  °C after only 10 cm, whereas this is the case for the tundra only after 26 cm. The summer situation shows that in 2000 the thaw depth reaches already through the gravel layer into the silt for the scenario with excess ice. Initially, an even increase in AL thickness is observed across all tiles, whereas from 2075 onward a clear acceleration of mainly shoulder and toe is visible. For the year 2090, temperatures of  $+5.7$  °C are simulated at the boundary between gravel and silt (Figure 65). The soil thaws more than 2 m deep and up to 85 cm into the silt beneath the gravel layer in the shoulder.

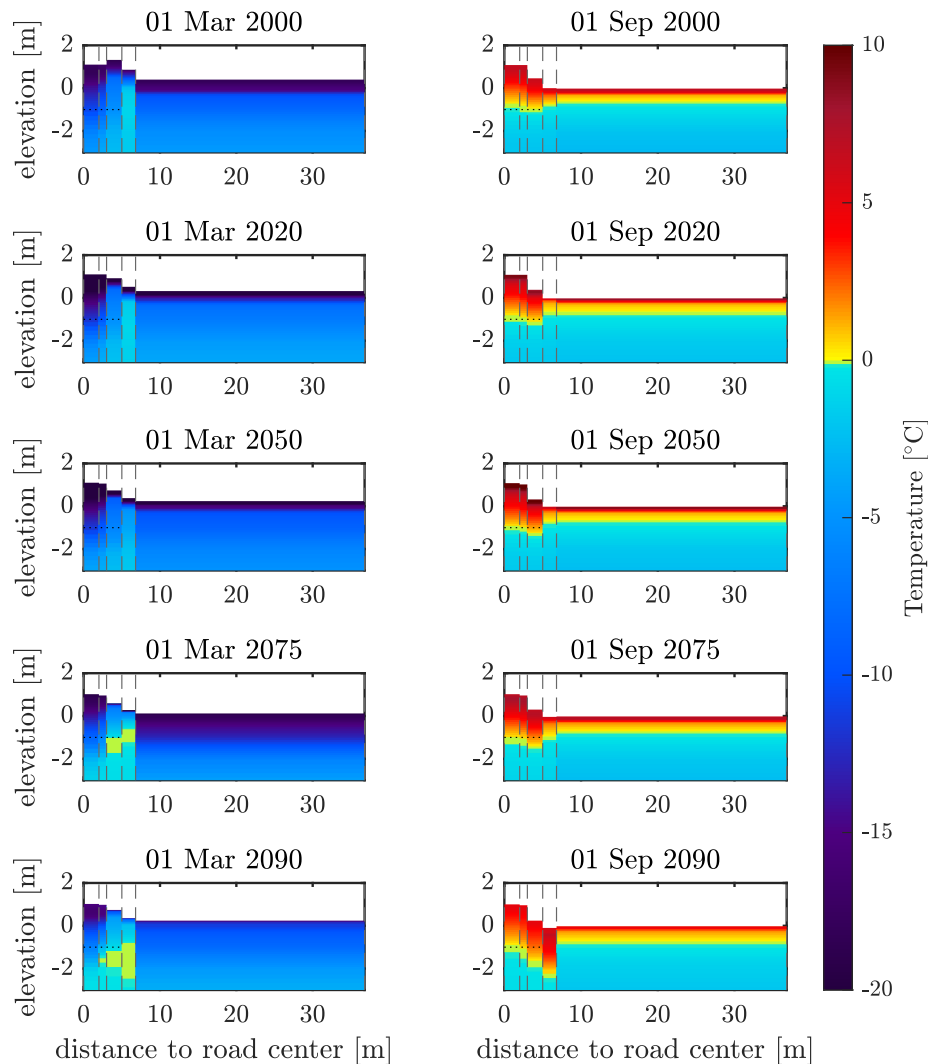


Figure 65: Simulated ground temperatures in the road, shoulder, toe, and adjacent tundra at the end of winter (left) and summer (right) for past (2000), present (2020), and future (2050, 2075, and 2090) climate conditions for scenario f) with excess ice between  $-1$  and  $-2$  m. The dotted line represents the lower boundary of the gravel layer.

#### 4.4 Comparison of the scenarios

Now that the details of the different scenarios are known, I look at them from different points of view regarding their changes. This includes the changes in road surface color, the road layer properties, excess ice and the snow removal practice.

#### 4.4.1 Influence of road surface color

In order to evaluate the influence of the surface colour, the standard scenario is compared with scenario b) with low road albedo and scenario d) with cleared embankment is compared with scenario c) with cleared embankment and changed albedo. The most obvious effect is that the AL thickness is about 7 cm to 25 cm deeper over the entire study period for the two units road and outer road, since the albedo is higher and therefore the incoming radiation heats the soil (Figure 66). The road is slightly more affected, than the outer road. The outer road is influenced by the untouched shoulder and therefore soften in the response. The shoulder experiences changes up to 10 cm due to the change in albedo, whereas the lower albedo  $\alpha = 0.1$ , i.e. darker surface of the road, leads to greater thaw depths immediately below the adjusted tiles (here: road and outer road). The shoulder is affected because the model is lateral coupled and takes the temperature change from the road into account. When comparing the scenarios, it is noticeable that there are very small up to 5 cm changes for both toe and tundra with an acceleration in the toe around 2070, i.e. the albedo of the road has a small influence on these tiles in terms of permafrost degradation. There occurs heave for some years in those tiles.

In general, it can be observed for all tiles that the scenarios with snow on the shoulder are more affected than those where the snow is removed. This is the case because the snow removal has the opposite effect and tends to cool the cross-section (see subsection 5.2). For the initial conditions the changes for all tiles are equal, except the shoulder with another snow situation. Therefore, it can be assumed that those changes are mainly related to the change in albedo.

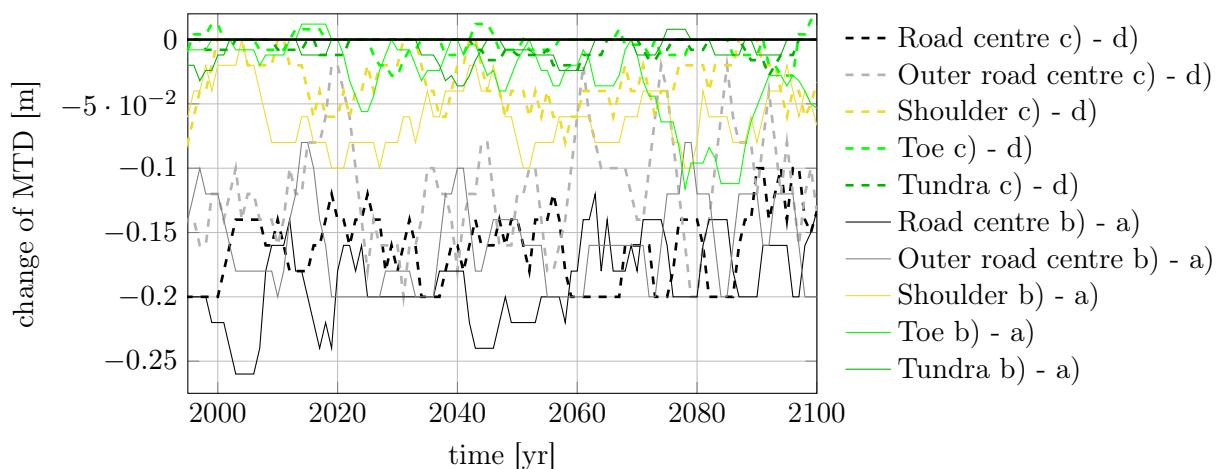


Figure 66: Simulated temporal evolution of change of maximum thaw depth (MTD) for all structural units with difference in scenarios a) and b) as well as c) and d) to see the influence of change in road albedo.

The permafrost temperatures are identical for the scenarios with double the amount of snow a) with higher and b) with lower albedo. For the scenarios with cleared embankment c) and d) deviations of maximum 0.2K occur, so that I conclude that the change in albedo from  $\alpha = 0.3$  to  $\alpha = 0.1$  has only very little influence on deeper layers in the permafrost.

#### 4.4.2 Influence of road layer properties

In order to investigate the influence of the road layer properties, scenario a) as reference scenario and scenario e) with the changed values for thermal conductivity and volumetric heat capacity of the mineral components are compared. This means that although mainly the gravel is adjusted, the constants also influence the mineral fraction in the silt and bedrock. Peat with  $\theta_m = 0.05$  (Table 6) is just slightly affected. The tiles road, outer road and shoulder experience the largest differences in AL depth. Thus, the AL for the standard scenario a) is up to 40 cm deeper than for scenario e) with the changed thermal properties (Figure 67). This means that the road for scenario e) only thaws within the gravel layer and does not reach the silt, whereas for the standard scenario a) the silt layer already thaws from 2060 onward, which leads to greater subsidence, as silt is more susceptible to settlements due to significantly smaller grain sizes and the grain structure (subsection 5.2). This is not the case for scenario e) until 2100, as all tiles thaw above the layer boundary and only the shoulder allows the silt layer to thaw slightly in the last two years.

With regard to the toe and tundra, the change in thermal properties leads to AL deepening of up to 10 cm for the tundra and up to 15 cm for the toe. I conclude that the change mainly affects the gravel layer and only to a minor extent the other soil types. Through lateral processes they are influenced as well. Exchange of heat and water/moisture are implemented in the CryoGrid model, that allow the tiles to transfer them and therefore show an extenuated effect in the adjacent tiles. I conclude that the shoulder radiates slightly onto the toe for the purpose of temperatures and that a greater change occurs there compared to the tundra.

Furthermore, an increasing trend of changes in AL deepening are observed with consecutive time. This means that the change has a constant effect, largely independent of how warm the ground is. If the soil has different temperatures depending on scenario a) or c), the AL thickness will still develop with an almost linear trend.

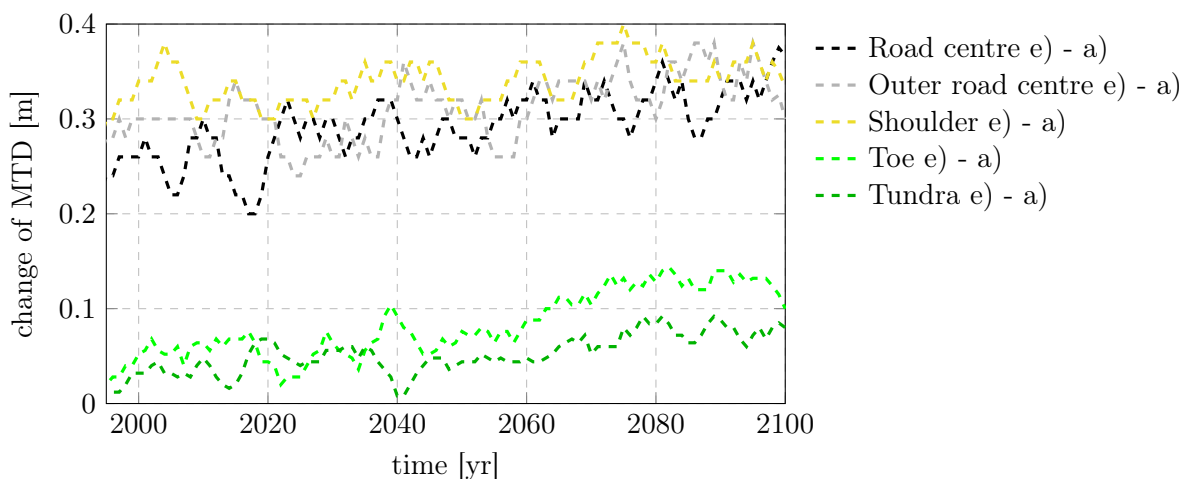


Figure 67: Simulated temporal evolution of change of maximum thaw depth (MTD) for all structural units with difference in scenarios a) and e) to see the influence of change in road layer properties.

The permafrost temperatures difference of scenario e) and scenario a) is about two to four tenths °C, with scenario e) being the colder one. That is another indication of the influence of

the change in thermal properties. The permafrost temperature is measured at the ZAA, which is typically at greater depths. Since the bedrock in the model is located at 7 m depth, the change in mineral properties may play a role here. Both scenarios show a developing talik formation in the shoulder from 2075 onward, which is only shifted in depth by the difference in the AL differences.

#### 4.4.3 Influence of excess ice in the ground

To determine the influence of excess ice, I compare scenario a) as reference and f) with excess ice between 1 m and 2 m depth. For the AL deepening, only minor differences initially occur in the comparison of the two scenarios. Until 2077, the increase in all tiles remains below 20 cm (Figure 68). After 2077, there is a strong increase mainly in the toe, as the AL deepening is triggered by the onset of ponding in 2070. The toe experiences a change of just under 1.5 m due to the excess ice layer. The shoulder has a change of about 50 cm and the road 20 cm to 25 cm. The tundra is hardly affected by the excess ice and experiences changes of at most 8 cm. I conclude that the presence of built infrastructure on the permafrost has a decisive influence on the thaw behaviour and thus the subsidence in ice-rich soil. The thawing of the AL beneath the gravel layer with soil containing excess ice is less dominant than the thawing of the adjacent toe into the ice-rich permafrost. The thawing of the excess ice releases a lot of water, which immediately collects in the same year as a pond next to the road.

The excess ice does not have a major influence on the permafrost temperatures within the period of 100 years, as these change by a maximum of two tenths °C. The warm layers near the surface have not yet transferred this heat to deeper layers. However, due to the shifts in the trumpet plot, it is clear that there is a warming trend.

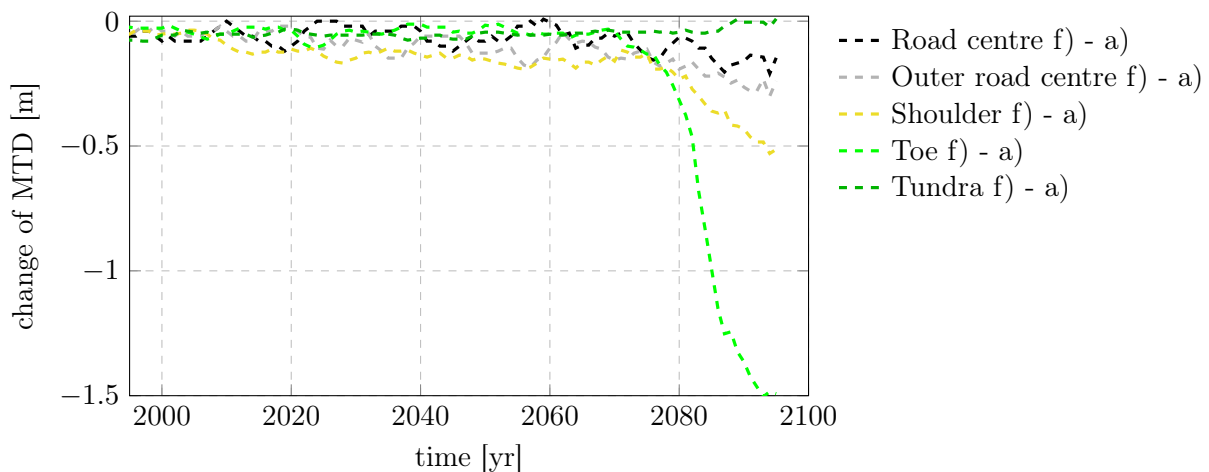


Figure 68: Simulated temporal evolution of change of maximum thaw depth (MTD) for all structural units with difference in scenarios a) and f) to see the influence of excess ice.

#### 4.4.4 Influence of snow removal practice

The influence of snow removal practice on the shoulder by clearing the snow are investigated using scenarios a) as a reference scenario and d) with a cleared shoulder. Additionally, I examine the two scenarios b) with low albedo and c) with low albedo and cleared shoulder. Due to the

removal of snow, temperatures are significantly cooler on the ground, especially in winter, and the AL is thinner across almost all tiles (Figure 69). However, the tundra shows less than 5 cm change for both comparison cases and is thus hardly affected by the removal of the snow. Contrariwise, the adjacent toe indicates a change in AL averaging 5 cm to 15 cm with a peak of up to 23 cm change between 2070 and 2090. Road and outer road also vary greatly in changes in AL layer depth from 0 cm to 17 cm. The shoulder, where the snow removal is executed, represent comparatively little change. For the case with the higher albedo, there is even AL deepening by 2060 through to the removal of the snow. Due to the insulating effect of snow, the AL is usually deeper underneath those settings. In these scenarios the snow affected shoulder indicates about 10 cm change with a peak of 13 cm by 2080. The silt is also affected for the cases without snow on the shoulder, only somewhat delayed.

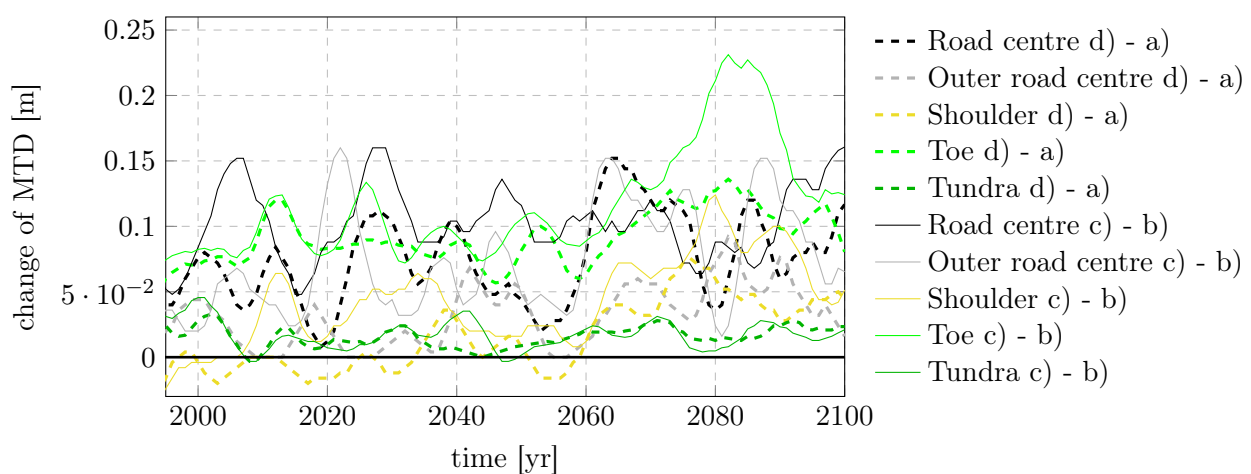


Figure 69: Simulated temporal evolution of change of maximum thaw depth (MTD) for all structural units with difference in scenarios a) and d) as well as b) and c) to see the influence of snow removal from the shoulder.

The decisive influence of the snow removal practice is that the temperatures throughout the entire profile are a few degrees cooler in winter. For the scenarios with snow on the shoulder, the incipient talik formation is already visible from 2075 onward, whereas the scenarios in which the snow has been removed show a continuously rising temperature gradient from the cold surface to the permafrost temperature. The permafrost temperature is four to eight tenths °C colder when the snow on the shoulder has been removed.

The forcing data indicates a decrease of snow over time for Ilulissat, so that the insulation on the shoulder and toe would also become thinner (subsection 5.1). However, the positive effect of this is not apparent and is covered by warmer temperatures and the release of water, as an increase in AL over time is apparent for all scenarios.

For the iButton sensors, a good agreement with the modeled soil temperatures is shown. The differences caused by the snow removal practice are reflected in the model. The sensors overlaid with snow in winter remain between 2 K and 5 K warmer than the temperature of the sensors further away and less influenced by snow.

## 5 Discussion

Now that all results are known, I discuss the forcing data in terms of how realistic they are and what possible reasons for deviations might be. Furthermore, I review the model results and compare them to studies where similar parameters are considered. Finally, I discuss to what extent the regulations for road construction are met and which measures can be useful.

### 5.1 Forcing data

The climate forcing data I use in CryoGrid consists of ERA5 reanalysis data and the MPI-ESM projection, coupled with the overlap period of six years and downscaled with the distance-weighted interpolation. Regarding the reanalysis data, there is a good agreement with the data from the weather station in Ilulissat. The projection data with MPI-ESM for scenario SSP5-8.5 show a slight warming in the current century with respect to temperature. However, the measured linear trend of the projection is lower than for the observation period or the ERA5 data. Since the SSP5-8.5 scenario is used, a stronger effect is expected in terms of climatic changes.

The geographical location of Ilulissat causes difficulties in the downscaling process of climate model data. The town is located on the coast in a mountainous area with large local differences. The distance to the Greenland Ice Sheet amounts to just 30 to 40 km. The ERA5 data have a small grid with sufficient cells on the mainland, which are well suited for downscaling. The closest is just 5 km away. This provides very accurate values after downscaling, which was also confirmed by comparison with the data from the weather station. For the projection data, on the other hand, the grid is much larger, so the cells are far away from the POI and are located on the water and on the ice, making them much colder and representing a different setting. The nearest grid point is about 80 km away from the town on the ocean. The downscaling algorithm cannot capture the local differences with another micro climate. Although the results are weighted and interpolated, they tend to be too cold and thus do not correspond to the conditions for Ilulissat. The approach via TopoSCALE only covers the topography and the orientation towards the sun, but cannot consider such local specifics. Schneider von Deimling et al. (2021) has a similar setup for the road structure at another location. They investigate the Dalton Highway in Alaska at a comparable latitude but different setting and surroundings. Dalton is located more inland with a flat topography, whereas Ilulissat is located on the coast and is more mountainous with large local differences. The downscaling seems to be more realistic with grid cells in the same climatic conditions.

The reanalysis data is validated and captures the climatic conditions very well, but the projections are less trustworthy. This hypothesis is supported by the data from the local weather station in Ilulissat but also by the thermal regime of the ground. The borehole temperatures are close to the simulated temperature distribution. Therefore, I focus on the projection data. Comparing my forcing data set from Ilulissat to the forcing data from Schneider von Deimling et al. (2021) used for the same SSP scenario and the same time period in Alaska, notice that they show a stronger warming trend. The MAAT increases by about 10 °C, whereas the MAAT for Ilulissat only increases by just under 5 °C. The thawing index  $I_t$  starts with similar values for both locations, whereas Dalton is about 800 ° d larger from 2040 onward. For the freezing index  $I_f$ , this is about 1500 ° d lower than in Ilulissat in 2020. However, by the end of the 21<sup>st</sup> century these are comparable. This means that significantly greater warming is projected for Dalton for the same forcing setup. Another parameter is the snow data, which is very limited for the reanalysis and cannot be validated very well. The

declaration of a rate and the depth are transferable for the amount of snow, but the start and end of the season can strongly vary. With a single event of cold temperature and precipitation, a thin snow cover in summer is captured and falsifies the data. A statement on the reanalysis data is only possible to a limited extent, as the validation period is not very long. For the projection, there is a decrease in total snowfall per season. This applies to both Ilulissat and Dalton and raises slight inconsistencies, as higher temperatures are expected due to climate change and thus more moisture is stored in the air, which in turn leads to more precipitation (liquid and solid). Precipitation is projected to increase by 2100 for the Baffin Bay/Davis Strait (BBDS) region, which includes West Greenland and East Canada (AMAP 2017a). The forcing data and the model run results tend to decrease the snowfall and therefore does not reflect this prediction. The snowfall season from the projection is shortening for Ilulissat by 2 to 4 weeks, whereas it is reduced by 6 to 10 weeks in Alaska. Due to the higher air temperatures, snow forms later in the year and ends earlier. Thus, a higher liquid precipitation is expected. This shortened snow cover period has an effect on the surface albedo by reflecting radiation. Contrarily, snow serves as an insulator and makes it more difficult for heat to escape from the ground. Both locations show the same general behaviour, but more extenuated for Ilulissat. The setting of scenario and period are identical, therefore one influencing factor is the geographical positioning of the two locations and the issue of local scale. By changing the POI for Ilulissat more inland, the weighting of the oceanic grid cells might be less dominant. Contrarily, the grid cells from higher elevation and ice sheet related are getting stronger, which ultimately ends in similar forcing data sets for the alternative POI.

MPI-ESM is just one projection model and might be not well suitable for my location in Greenland. The projection of the NorESM, which has delivered good results for Greenland so far, is another model with a relatively rough grid of  $1.9^\circ$  in latitude direction and  $2.5^\circ$  in longitude direction (Figure 16). The closest grid points are therefore on the water between Disko Island and Ilulissat and in the Jakobshavn Isbræ near the ice sheet. As for the MPI-ESM, the temperatures for

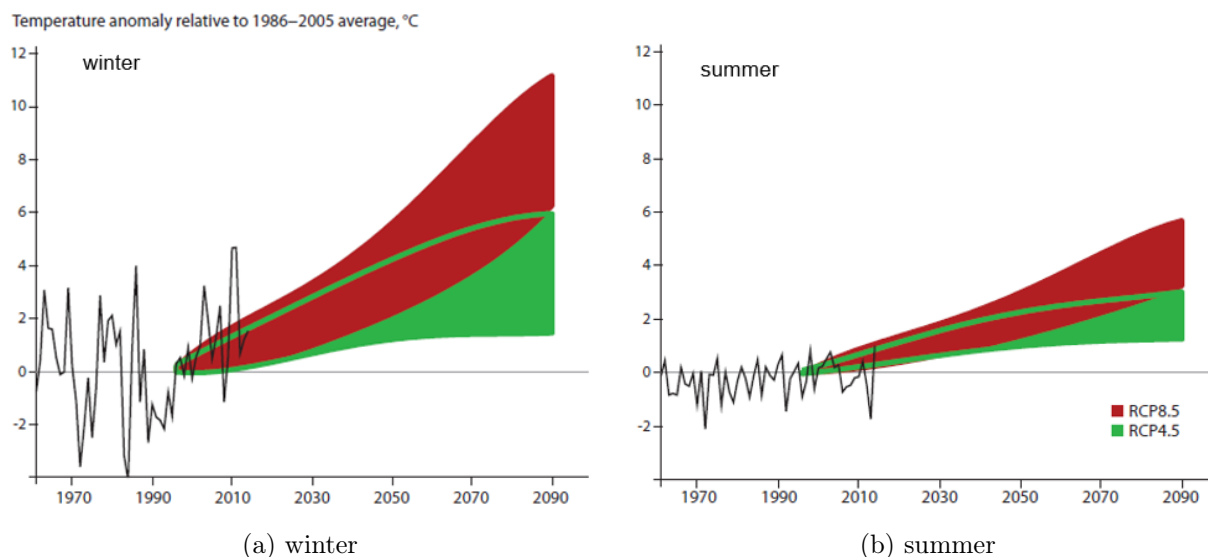


Figure 70: Observed and projected anomalies in 2-meter air temperature averaged over the land portion of the BBDS region, relative to the 1986–2005 average (AMAP 2017a)  
black = observations; green = RCP4.5; red = RCP8.5

the city are accordingly underestimated. Downscaling using TopoSCALE resulted in temperatures about 2.1 °C lower than for the measured data from the DMI weather station. That has the same reason as for the MPI-ESM, that the grid cells are mainly on ocean and ice or higher elevation having a different micro climate.

When looking at a broader scale the future estimation of the BBDS region is convenient as it includes the study site. For the region including West Greenland and Eastern Canada, medium to high emissions are assumed for the climate projections (AMAP 2017a). Continuous warming is assumed for the region, so that the air temperature in winter rises 1 to 4 °C by 2030 and up to 10 °C in 2080 (Figure 70). That is already more than my projection assesses. The values are relative to the observation period between 1986 and 2005 or half of the time for the summer temperatures respectively (AMAP 2017a). The north-western part of the region is more severely affected than the south-eastern part. Due to this forecasted warming, the length of the thawing season will be extended by around 1-2 months (AMAP 2017a). For the end of the 21st century, a shorter snow cover period of 40-60 days can be expected, mainly in the coastal regions, including Ilulissat. My analysis accounts only for 2 to 4 weeks. With regard to the depth of snow, hardly any changes are to be expected in response to warming (AMAP 2017a). The values from the AMAP (2017a) report are significantly higher for the changes in temperature and also forecast a much shorter snowfall season and are closer to the values forecast for Dalton. This suggests that the forcing data I use as input to the CryoGrid model significantly underestimates the actual predicted values and thus shows less critical situations in terms of warming.

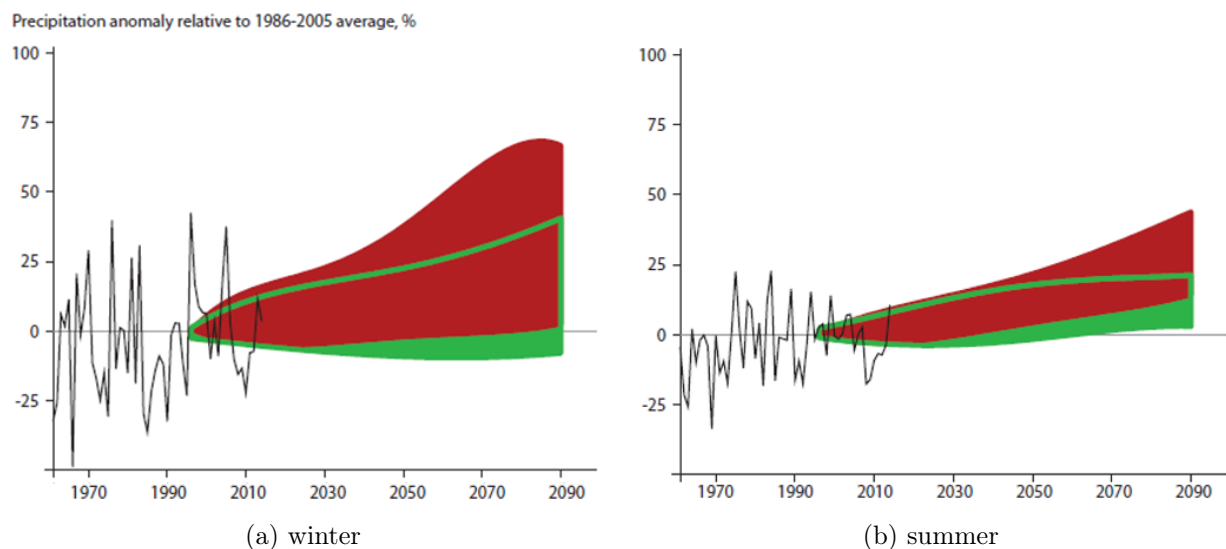


Figure 71: Observed and projected anomalies in total (liquid and solid) precipitation averaged over the land portion of the BBDS region, Changes are expressed as percentage differences with respect to the 1986–2005 average (AMAP 2017a)  
black = observations; green = RCP4.5; red = RCP8.5

In addition to the higher temperature, the precipitation is also influenced by the climatic changes, as the air can absorb more moisture, which results in more precipitation. For the winter, a change between -10 % and +25 % by 2030 and up to +70 % by 2080 is forecasted (AMAP 2017a).

The reference period is between 1986 and 2005. The projected amount of snowfall for my forcing data set is about  $-50\%$  less compared to present day conditions. That is almost an opposite trend. In summer,  $-5\%$  to  $+35\%$  can be expected (Figure 71). The greatest relative changes are again to be expected in the northwest of the BBDS region (AMAP 2017a).

## 5.2 Model results

The modeling of the scenarios shows a good agreement with the measured borehole temperatures for the present day conditions. The permafrost temperatures are between  $-1.6^\circ\text{C}$  and  $-4^\circ\text{C}$ . This corresponds to a larger range than Biskaborn et al. (2019) indicated in their study. According to this, a globally consistent assessment of temperature change in permafrost is conducted between 2007 and 2016. The permafrost temperature is approximately  $-3$  to  $0^\circ\text{C}$  in Mid-West Greenland, where Ilulissat is located (Biskaborn et al. 2019). An average increase of  $+0.3\pm 0.1^\circ\text{C}$  within 10 years is observed. This indicated trend is larger than the permafrost temperatures projected in my simulation. The change for me is a maximum of 1.2 K, i.e., 0.12 K in a 10-year interval. The observation supports the assumption that forcing underestimates real conditions and thus predicts a milder course of temperature increase. Nevertheless, it is evident from the shifts of the trumpet plot that the ground is subject to warming. The mean temperature of the areas near the surface tends to rise strongly, which results in the warming of the entire soil over a long period of time. The 100 years considered in my thesis are not sufficient to reflect this trend well, because the heat transfer in the soil by convection and conduction is a slow process. The more ice the ground contains and the colder it is, the longer it takes because the ice must first be warmed by the incoming heat energy before melting occurs. The phase transition of the melting itself requires large amounts of energy, which is why the temperature around  $0^\circ\text{C}$  is almost constant for a long time before it continues to rise, the so called zero curtain effect (Batbaatar et al. 2020). The trumpet plots also show anomalies at the layer boundaries. As the porosity changes to higher values, it is easier for heat to reach adjacent layers by heat transfer, so the warming is faster. The simulated processes of lateral interaction at layer boundaries are reflected in the temperature distribution. Realistic results are simulated for present day conditions.

The marine limit as well as the briefly mentioned laboratory investigations indicate a slightly saline soil, which is why freezing point depression occurs and the soil already thaws below  $0^\circ\text{C}$ . Consequently, the areas that already show an incipient talik formation are exposed to these changes. Thawing of the soil releases the bound ice, which leads to ponding in the area of the shoulder and thus increases the degradation. The road is exposed to subsidence and damage due to melting. When the ice melts the volume of the soil shrinks resulting in subsidence and cracking. The study of Schneider von Deimling et al. (2021) considers the case of ponding and comes to the conclusion that the degradation is strongly accelerated as soon as the ponding starts. In my standard scenario, ponding occurs for the excess ice scenario. The resulting effect agrees with the findings from Schneider von Deimling et al. (2021), hence pronounced and accelerated AL deepening occurs beneath the tile where the pond starts to form.

When the AL is penetrating the silt layer, it may cause subsidence and damage. Due to the finer pore spaces, water is better retained in the silt and thus forms a stable framework of soil grains and ice, which experiences greater subsidence during thaw processes. The ice saturation of the pores  $S_{r,i}$  for the investigated boreholes ILU2021-01, ILU2021-02 and ILU2021-03 range between  $S_{r,i} = 0.68$  near the surface and up to  $S_{r,i} = 1.28$  in the excess ice layer in the area between 0.80 m

and 1.48 m depth (Scheer & Ingeman-Nielsen 2022). Thus, it can be assumed that in the critical area from 1 m depth below the gravel, subsidence is to be expected. As the settlements for road, outer road and shoulder are not uniform but differential, cracks are to be expected. Because the cold periods are less cold, however, this has an impact on the permafrost, which is no longer cooled as much in winter and therefore more likely to thaw in summer. Thus, the permafrost table could slowly decrease, which can lead to stability problems, especially in the soil layers with large ice content. This would have an impact on the construction and long-term stability of the roads, as settlements are to be expected.

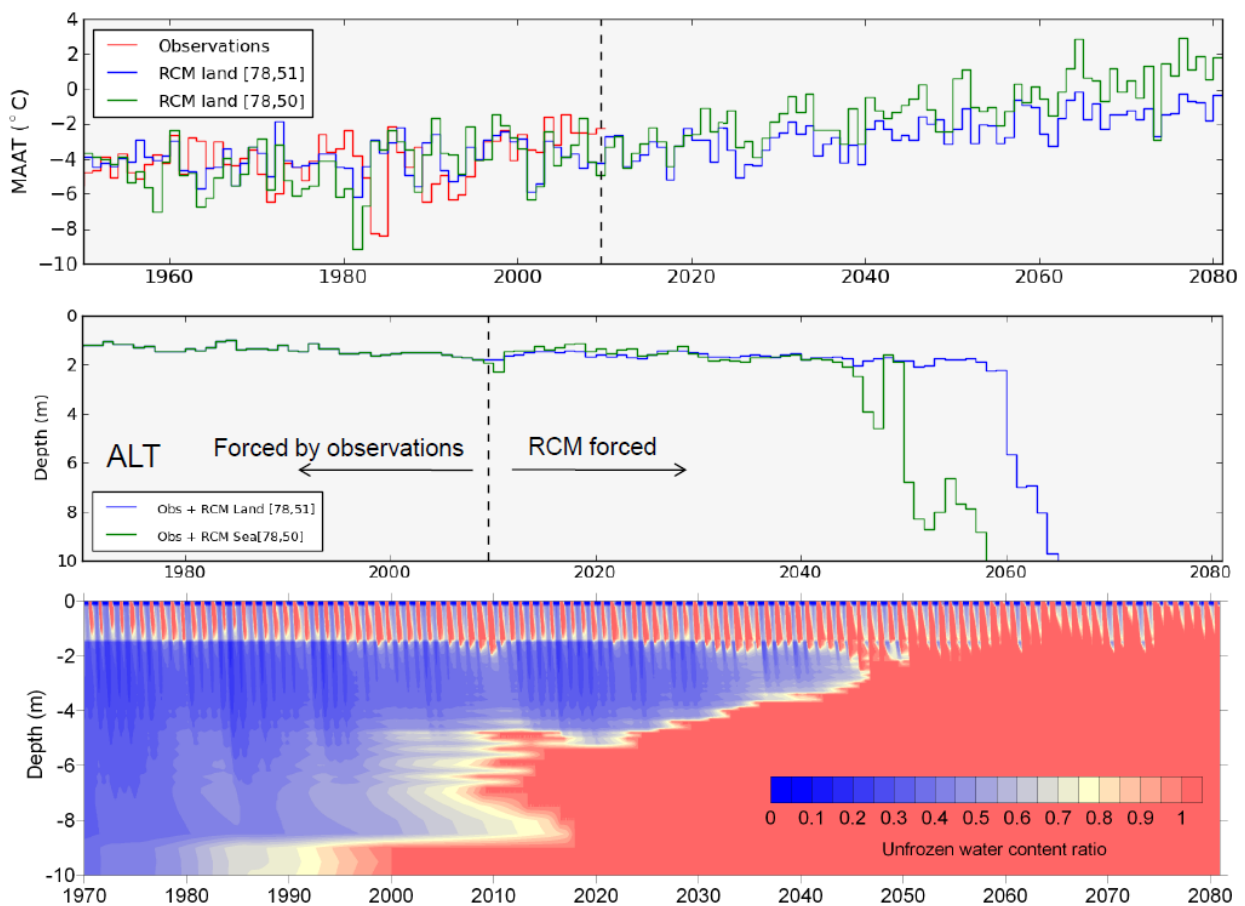


Figure 72: **Top:** Mean Annual Air Temperature for measured climatic time series (red) as well as the two closest regional climate model (RCM) timeseries to Ilulissat, which have been scaled and debiased to match the properties of the measured time series over the last 30 years

**Middle:** Modelled Active Layer Thicknesses in Ilulissat using the two RCM time series as forcing for the model

**Bottom:** Modelled ground unfrozen water content ratio using RCM gridpoint [78,50] on the sea in front of Ilulissat as forcing

(Ingeman-Nielsen et al. 2010)

According to the SWIPA<sup>4</sup> report, a warming of the permafrost and an increase in the AL thick-

<sup>4</sup>Snow, Water, Ice and Permafrost in the Arctic

ness can already be observed in almost all Arctic regions (AMAP 2017b). This can be confirmed for the location Ilulissat. Both borehole data and the results of the CryoGrid model runs indicate AL deepening. A significant decrease in the permafrost area is forecast by the end of the century, so that more erosion and frost heave are to be expected (AMAP 2017b). This loss is also predicted for Ilulissat, which has a significant impact on the construction of infrastructure. Based on the high resolution RCM HIRHAM, a reanalysis for the permafrost temperature dynamics and active layer thickness was generated by Thomas Ingeman-Nielsen 13 years ago (Ingeman-Nielsen et al. 2010). The freezing point depression due to the salinity in soil was included. The results in Figure 72 predict that the mean annual temperature increases by about 2 °C by 2080 (Ingeman-Nielsen et al. 2010). The AL thickness between 2050 and 2060 (depending on the grid point in the forcing) is expected to be over 10 m, which is equivalent to a complete thawing (Ingeman-Nielsen et al. 2010). This results in settlements and stability problems. This is contrary to the results I simulated. The AL thaws for me to a maximum depth of 2.5 m for the scenario with excess ice by the end of the century, whereas Ingeman-Nielsen et al. (2010) results predict complete thawing by 2050. This supports my assumption that the forcing data underestimate the expected behavior.

### Road surface color

The influence of changing the albedo of the road surface was investigated out on a test section on the Alaska Highway near Beaver Creek, Yukon, Canada, where different road surfaces with albedos ranging from 1.4 to 5.5 were investigated (Dumais & Doré 2016). In the study by Dumais & Doré (2016), a correlation was found between the albedo of the road and the radiation index, so that the albedo can be used to calculate the temperature at the surface of the road. This shows that the albedo has an influence on the surface temperature, which also radiates to deeper layers. That the albedo has an influence on the ground thermal regime is shown by numerous studies that suggest light colour painting for the embankment to achieve a cooling effect (Qin, Liang, Huang & Tan 2016). Furthermore, there are studies that examine the albedo for crushed-rock layer depending on particle size, diurnal, solar and seasonal conditions and can determine an effect of this (Wang et al. 2019, Qin, Tan, Yang & Li 2016). It was found that by raising the albedo of the sun-facing embankment up to  $\alpha = 0.2$ , can balance to a symmetric thermal distribution with the shaded side (Qin, Liang, Luo, Tan & Zhu 2016). In addition, there are studies on road deformation after the change from natural surfaces to asphalt roads based on laser scanning tools, which detect subsidence of up to 6 cm within one year, although this is not exclusively due to the albedo change (Iurov & Marchenko 2019).

### Road layer properties

The study by Galkin et al. (2023) investigates the extent to which the pores of a gravel bedding are filled with water or sand and its effect on the thermal conductivity of such a gravel mixture. According to the study, the thermal resistance of the road structure changes significantly depending on the filling material. With increasing ice content, the thermal conductivity of the gravel also increases, and the greater the value for thermal conductivity, the stronger this dependence. In addition, there are differences in the change of thermal conductivity depending on whether the pores are filled with sand (smaller) or ice (larger). Hence, the thermal conductivity and thus the thermal regime of the soil can be influenced by the filling material and the filling quantity of the pores (Galkin et al. 2023). My model result are showing an influence of the change of thermal properties as well. Due to the procedure that I changed the properties of the mineral fraction, it is not a simple comparison, since

other minerals are influenced as well.

Furthermore, a test section at Gonghe-Yushu Expressway in the south-eastern Tibetan plateau was constructed with different embankment structures to investigate and model the ground temperature distribution (Tai et al. 2017). It was found that the heat budget around the permafrost table of the embankment depends on the heat capacity of the respective material (Tai et al. 2017). As well as in my model the change of the properties has an influence on the permafrost degradation. Unfortunately, most studies do not focus on the change of a single parameter like this, since this is not a realistic approach for the practice.

### Excess ice in the ground

Excess ice has a major influence on the thermal degradation of my model. For the ice lens to be thawed, a lot of heat is necessary for phase change, which keeps the temperature more or less constant. Basically, phase change is a kind of barrier for heat transfer. When the ice is fully melted, the heat transfer would occur much easier, and the layers below will be highly affected. In the modelling of Schneider von Deimling et al. (2021), a similar phenomenon was shown, that when the AL entered the excess ice layer, ponding started and led to enormous AL layer deepening in the toe and with a time lag also in shoulder, outer road and road (Appendix A). The same process occurs in my scenario with excess ice. Since water has a higher thermal conductivity than air, the thermal energy can be transferred efficiently into the ground and it thaws faster beneath the pond. The surface water insulates the ground from cold temperatures that could have a cooling effect. In addition, the sun heats the water, which stores the heat and transfers it to the ground.

In the real setting in Ilulissat, the layers with ice-rich permafrost are mainly between 80 cm and 148 cm with ice saturation  $S_{r,i} > 1.0$  and thus excess ice in the ground (Scheer & Ingeman-Nielsen 2022). Based on the thaw depths of the boreholes and the simulation, which models excess ice between 1 m and 2 m, this area is extremely endangered. There is a high probability that it will begin to thaw this century if the selected climate forcing is close to reality. My model results show a less extreme scenario, since the forcing is not realistic. Therefore, the real setting would lead to an increased vulnerability of the excess ice layers.

The Chen et al. (2023) study at Qinghai-Tibet Railway (QTR) also includes excess ice in deeper layers. As soon as the permafrost table for future projections is below the embankment, the destabilisation of the subgrade begins. Ultimate embankment destabilisation occurs as soon as the excess ice melts and is accompanied by strong subsidence of the embankment structure (Chen et al. 2023). According to this study, the bottom settles by 0.8 m when the excess ice has melted. A large influence of depth and thickness of the excess ice layer on the timing of subsidence was found (Chen et al. 2023). Similarly, my results show that the change becomes much more dramatic once excess ice is contained. In the study by Schneider von Deimling et al. (2021) the vulnerable case (Appendix A) was modelled with excess ice and ponding. Here, a significantly earlier degradation of permafrost could be observed (Figure 79). Therefore, ponding occurs already in 2013, whereas in my own model for Ilulissat it is only the case in 2070. There is agreement in the prediction that the AL for the toe is the first to experience a rapid drop and the tundra tile has the fewest changes.

### Snow removal practice

The snow removal has a major influence on the permafrost degradation beneath the cleared em-

bankment. As the removed snow allows the cold air to cool the embankment during winter, thus delaying thawing in summer. The insulating effect of the snow keeps the heat in the ground during the winter, which heats up even more in the summer. With warmer initial temperatures after winter, the temperature can rise faster in summer and the thaw process can advance to greater depths. My simulated models show, that snow removal has a noticeable impact on the condition and preservation of permafrost. In practice, therefore, numerous structural solutions are used to keep the embankment in a state, as cold as possible, and thus delay permafrost degradation. These include ACE, heat drains, air convection culverts, snow/sun sheds or thermosyphons (subsubsection 1.2.2).

In the paper by Schneider von Deimling et al. (2021), iButton sensors were also used along a transect of the road up to 50 m away. According to this, warmer soil surface winter temperatures were recorded in the immediate vicinity of the road. The cleared road has significantly colder surface temperatures than shoulder, toe and tundra. The warming effect is clearly visible in the simulation by Schneider von Deimling et al. (2021), but with strong annual fluctuations. In my simulation as well as in the iButton temperature loggers of Johanna Scheer (DTU) this insulating effect could be shown, which leads to warmer ground temperatures especially in winter. That increases the summer temperatures and the MTD. The change in AL depth may result in not only gravel thawing but also silt being affected, leading to greater subsidence and cracking. The thesis only shows a part of what can be realised with the model, an extension with other scenarios and combinations is possible at any time. Furthermore, the model results are highly dependent on the input data and even small changes in climate forcing or soil composition change the output enormously.

### 5.3 Road construction

The simulated temperature distributions reach the silt layer below the gravel for nearly all scenarios. Due to its properties of thermal conductivity, heat capacity, porosity and mineral fraction, the gravel is a very suitable material for the construction of a non-frost-sensitive embankment (Luo et al. 2019). Silt, on the other hand, as a fine-grained soil, loses the stability of its grain structure with the thawing of the ground, resulting in damage or failure of the road. I have adapted the model setup according to the guidelines for road construction in Greenland (Bigum and Steenfos (1984), Grønlands Hjemmestyre & Rambøll (2008)) and the existing roads on site. However, in the simulation it becomes clear that the AL already completely thaws the gravel layer in the present day conditions. If the construction method is maintained, that a part of the soils is excavated, it is practical to increase the thickness of the gravel layer and to follow the recommendations of Andersland & Ladanyi (2004) with 1.5 m. Alternatively, the embankment can be raised as is common practice in North America (Schneider von Deimling et al. 2021, De Guzman et al. 2021). This way the two systems road and tundra can be decoupled a bit. Additional measures to preserve the permafrost are desirable. It is a great advantage if new roads to be built are constructed in winter, so that the cold remains in the ground and it is not exposed to additional heat in summer. Additional measures to preserve the permafrost as in subsubsection 1.2.2 are desirable. Maintenance, in particular, plays a major role here. By removing the snow from the shoulder instead of storing it there, the permafrost stays much colder and preserves the road from damage. This is being partially implemented in Greenland, but there is still potential for further development.

## 6 Conclusion

The aim of the thesis was to show the influence of different parameters on the degradation of permafrost around and underneath roads. My thesis focused on Ilulissat in West Greenland. Using data from the local weather station and borehole temperatures, I validated ERA5 climate forcing and initial temperatures to use with the model in CryoGrid. The forcing data itself is based on ERA5 reanalysis data and the model projection from MPI-ESM. These fit the meteorological station for current conditions well, but underestimate the expected values for the future projections in terms of temperature and snowfall period, so that the model only delivers a weakened response.

For the simulation itself, the laterally coupled heat transfer model CryoGrid was used in the community version, whereby various scenarios were simulated. It was shown that a higher albedo of the road transports less heat into the ground. The AL becomes up to 25 cm deeper for the road, whereas the influence decreases strongly towards the tundra. The change in the thermal properties of the gravel layer make a difference of up to 40 cm in the layers associated with gravel for the values thermal conductivity and heat capacity, as the heat transfer is changed. Excess ice has the greatest impact on thermal degradation in this study, increasing the AL for the toe to 1.5 m by the end of the century, leading to subsidence in this area due to the loss of ice volume. As these are differential settlements, damage to the road structure in Ilulissat can be assumed. The rapid drop occurs when the AL enters the excess ice layer. For the snow removal practice, the model setup chosen here shows warmer ground temperatures and a decrease in MTD averaging up to almost 20 cm for cleared embankment. This does not change so much for the shoulder itself, but this approach affects the entire road structure.

Based on my simulations, a high albedo of the road should be chosen for the ideal setup and the routing should be designed to avoid excess ice. The thermal properties of the gravel can be varied according to scenario e) and the layer thickness should be increased so that the AL does not enter the underlying soil layer or only very late, as degradation is increased from this point on. In addition, great importance should be attached to snow removal practice and the shoulder should be kept free of snow in winter in order to realise the cooling of the permafrost and to slow down the AL deepening.

In order to continue working on this project in the future, I would suggest that, on the one hand, the extent to which the model projection for climate forcing can be made more realistic is investigated. On the other hand, further scenarios and combinations can be carried out. I would create a best case scenario with all positively influencing factors and a worst case scenario with all negatively influencing factors. I would also run the model through more tiles with a higher resolution and run other future projections with different SSP scenarios to get an idea of the spread of responses. By using additional tiles, snow redistribution can be simulated more realistically. Ilulissat does not have a uniform soil composition, so other layering with greater depth to bedrock and more sandy or clayey components could be investigated to have a more realistic picture of the site.

Overall, my simulations show the enormous influence of excess ice in the ground and the importance of snow-plowing practices to maintain the permafrost beneath infrastructure.

## References

- Aas, K. S., Martin, L., Nitzbon, J., Langer, M., Boike, J., Lee, H., Berntsen, T. K. & Westermann, S. (2019), 'Thaw processes in ice-rich permafrost landscapes represented with laterally coupled tiles in a land surface model', *The Cryosphere* **13**(2), 591–609.  
**URL:** <https://tc.copernicus.org/articles/13/591/2019/>
- Adam, Q. F., Levenberg, E., Ingeman-Nielsen, T. & Skar, A. (2023), 'Modeling the use of an electrical heating system to actively protect asphalt pavements against low-temperature cracking', *Cold Regions Science and Technology* **205**, 103681.  
**URL:** <https://doi.org/10.1016/j.coldregions.2022.103681>
- Alexander, A., Obu, J., Schuler, T. V., Ka̧b, A. & Christiansen, H. H. (2020), 'Subglacial permafrost dynamics and erosion inside subglacial channels driven by surface events in Svalbard', *Cryosphere* **14**(11), 4217–4231.
- Allard, M., Lemay, M., Barrette, C., L'Hérault, E. & Sarrazin, D. (2012), Permafrost and climate change in Nunavik and Nunatsiavut : Importance for municipal and transportation, in ArcticNet Inc., ed., 'Nunavik and Nunatsiavut: From science to policy. An Integrated Regional Impact Study (IRIS) of climate change and modernization', 1 edn, ArcticNet Inc., Quebec City, chapter 6, pp. 171–197.
- AMAP (2017a), *Adaptation Actions for a Changing Arctic - Perspectives from the Baffin Bay/Davis Strait Region*, 1 edn, Arctic Monitoring and Assessment Programme (AMAP), Oslo, Norway.
- AMAP (2017b), *Snow, Water, Ice and Permafrost in the Arctic (SWIPA)*, Arctic Monitoring and Assessment Programme (AMAP), Oslo, Norway.  
**URL:** <https://www.amap.no/documents/doc/snow-water-ice-and-permafrost-in-the-arctic-swipa-2017/1610>
- Andersland, O. B. & Ladanyi, B. (1994), *An Introduction to Frozen Ground Engineering*, Springer, Dordrecht.
- Andersland, O. B. & Ladanyi, B. (2004), *Frozen Ground Engineering*, John Wiley & Sons.
- Batbaatar, J., Gillespie, A. R., Sletten, R. S., Mushkin, A., Amit, R., Liaudat, D. T., Liu, L. & Petrie, G. (2020), 'Toward the detection of permafrost using land-surface temperature mapping', *Remote Sensing* **12**(695), 1–22.
- beadedstream inc. (2022), 'A Guide to Thermistor Strings'.  
**URL:** <https://www.beadedstream.com/a-guide-to-thermistor-strings/>
- Bentsen, M., Bethke, I., Debernard, J. B., Iversen, T., Kirkevåg, A., Seland, O., Drange, H., Roelandt, C., Seierstad, I. A., Hoose, C. & Kristjánsson, J. E. (2013), 'The Norwegian Earth System Model, NorESM1-M – Part 1: Description and basic evaluation of the physical climate', *Geoscientific Model Development* **6**(3), 687–720.
- Bezeau, P., Sharp, M. & Gascon, G. (2015), 'Variability in summer anticyclonic circulation over the Canadian Arctic Archipelago and west Greenland in the late 20th/early 21st centuries and its effect on glacier mass balance', *International Journal of Climatology* **35**(4), 540–557.  
**URL:** <https://onlinelibrary.wiley.com/doi/full/10.1002/joc.4000>

- Bigum and Steenfos (1984), *Bygdeveje i Grønland*, Technical report, Grønlands tekniske organisation.
- Biskaborn, B. K., Smith, S. L., Noetzli, J., Matthes, H., Vieira, G., Streletskiy, D. A., Schoeneich, P., Romanovsky, V. E., Lewkowicz, A. G., Abramov, A., Allard, M., Boike, J., Cable, W. L., Christiansen, H. H., Delaloye, R., Diekmann, B., Drozdov, D., Etzelmüller, B., Grosse, G., Guglielmin, M., Ingeman-Nielsen, T., Isaksen, K., Ishikawa, M., Johansson, M., Johannsson, H., Joo, A., Kaverin, D., Kholodov, A., Konstantinov, P., Kröger, T., Lambiel, C., Lanckman, J. P., Luo, D., Malkova, G., Meiklejohn, I., Moskalenko, N., Oliva, M., Phillips, M., Ramos, M., Sannel, A. B. K., Sergeev, D., Seybold, C., Skryabin, P., Vasiliev, A., Wu, Q., Yoshikawa, K., Zheleznyak, M. & Lantuit, H. (2019), 'Permafrost is warming at a global scale', *Nature Communications* **10**(1), 1–11.
- Boike, J., Nitzbon, J., Anders, K., Grigoriev, M., Bolshiyarov, D., Langer, M., Lange, S., Bornemann, N., Morgenstern, A., Schreiber, P., Wille, C., Chadburn, S., Gouttevin, I., Burke, E. & Kutzbach, L. (2019), 'A 16-year record (2002–2017) of permafrost, active-layer, and meteorological conditions at the Samoylov Island Arctic permafrost research site, Lena River delta, northern Siberia: An opportunity to validate remote-sensing data and land surface, snow, and', *Earth System Science Data* **11**(1), 261–299.
- Brubaker, M. Y., Bell, J. N., Berner, J. E. & Warren, J. A. (2011), 'Climate change health assessment: A novel approach for alaska native communities', *International Journal of Circumpolar Health* **70**(3), 266–273.
- Burt, W. V. (1954), 'Albedo over wind-roughened water', *Journal of the Atmospheric Sciences* **11**(4), 283–290.
- Cahoon, S. M., Sullivan, P. F. & Gray, A. N. (2022), 'Interactions among wildfire, forest type and landscape position are key determinants of boreal forest carbon stocks', *Journal of Ecology* **110**(10), 2475–2492.
- Chai, M., Mu, Y., Zhang, J., Ma, W., Liu, G. & Chen, J. (2018), 'Characteristics of Asphalt Pavement Damage in Degrading Permafrost Regions: Case Study of the Qinghai–Tibet Highway, China', *Journal of Cold Regions Engineering* **32**(2).
- Chalov, S. & Prokopenko, K. (2022), 'Sedimentation and Erosion Patterns of the Lena River Anabranching Channel', *Water (Switzerland)* **14**(23).
- Che, L., Zhang, H. & Wan, L. (2023), 'Spatial distribution of permafrost degradation and its impact on vegetation phenology from 2000 to 2020', *Science of The Total Environment* p. 162889.
- Chen, R., Schneider Von Deimling, T., Boike, J., Wu, Q. & Langer, M. (2023), 'Simulating the thermal regime of a railway embankment structure on the Tibetan Plateau under climate change', *Cold Regions Science and Technology* **212**, 103881.  
**URL:** <http://creativecommons.org/licenses/by/4.0/>
- Chuvilin, E. M., Bukhanov, B. A., Mukhametdinova, A. Z., Grechishcheva, E. S., Sokolova, N. S., Alekseev, A. G. & Istomin, V. A. (2022), 'Freezing point and unfrozen water contents of permafrost soils: Estimation by the water potential method', *Cold Regions Science and Technology* **196**, 103488.

- City population (2022), ‘Greenland: Municipalities, Major Towns, Settlements & Stations - Population Statistics, Maps, Charts, Weather and Web Information’.  
**URL:** <https://www.citypopulation.de/en/greenland/>
- Colgan, W., Wansing, A., Mankoff, K., Lösing, M., Hopper, J., Loudon, K., Ebbing, J., Christiansen, F. G., Ingeman-Nielsen, T., Liljedahl, L. C., MacGregor, J. A., Hjartarson, A., Bernstein, S., Karlsson, N. B., Fuchs, S., Hartikainen, J., Liakka, J., Fausto, R. S., Dahl-Jensen, D., Bjørk, A., Naslund, J. O., Mørk, F., Martos, Y., Balling, N., Funck, T., Kjeldsen, K. K., Petersen, D., Gregersen, U., Dam, G., Nielsen, T., Khan, S. A. & Løkkegaard, A. (2022), ‘Greenland Geothermal Heat Flow Database and Map (Version 1)’, *Earth System Science Data* **14**(5), 2209–2238.
- Connor, B., Goering, D. J., Kanevskiy, M., Trochim, E., Bjella, K. L. & McHattie, R. L. (2020), Roads and Airfields Constructed on Permafrost: A Synthesis of Practice, Technical Report 0005927, The Alaska Department of Transportation and Public Facilities, Fairbanks.
- Copernicus Climate Change Service, C. D. S. (2021), ‘CMIP6 climate projections’.
- Côté, J. & Konrad, J.-M. (2005), ‘Thermal conductivity of base-course materials’, *Canadian Geotechnical Journal* **42**(1), 61–78.  
**URL:** <https://cdnsiencepub.com/doi/10.1139/t04-081>
- De Guzman, E. M. B., Alfaro, M. C., Doré, G., Arenson, L. U. & Piamsalee, A. (2021), ‘Performance of highway embankments in the Arctic constructed under winter conditions’, *Canadian Geotechnical Journal* **58**(5), 722–736.  
**URL:** <https://doi.org/10.1139/cgj-2019-0121>
- Dearborn, K. D., Wallace, C. A., Patankar, R. & Baltzer, J. L. (2021), ‘Permafrost thaw in boreal peatlands is rapidly altering forest community composition’, *Journal of Ecology* **109**(3), 1452–1467.
- DMI (2022a), ‘Klimanormaler Grønland’.  
**URL:** <https://www.dmi.dk/vejrarkiv/normaler-gronland/>
- DMI (2022b), ‘Publikationer fra DMI’.  
**URL:** <https://www.dmi.dk/publikationer/>
- DMI (2022c), ‘Vejrarkiv’.  
**URL:** <https://www.dmi.dk/vejrarkiv/>
- Doré, G. (2004), ‘Development and validation of the thaw weakening index’, *International journal of pavement engineering* **4**(5), 185–192.
- Dumais, S. & Doré, G. (2016), ‘An albedo based model for the calculation of pavement surface temperatures in permafrost regions’, *Cold Regions Science and Technology* **123**, 44–52.  
**URL:** <http://dx.doi.org/10.1016/j.coldregions.2015.11.013>
- ECMWF (2022a), ‘ECMWF Reanalysis v5’.  
**URL:** <https://www.ecmwf.int/en/forecasts/dataset/ecmwf-reanalysis-v5>
- ECMWF (2022b), ‘ERA5’.  
**URL:** <https://www.ecmwf.int/en/forecasts/datasets/reanalysis-datasets/era5>

- ECMWF (2023), ‘ERA5: data documentation’.
- Encyclopædia Britannica Inc. (2023), ‘Pingo’.  
**URL:** <https://www.britannica.com/science/pingo>
- Epstein, H. E. (2013), *Earth Observation of Ecosystem Services*, 1 edn, CRC Press, Boca Raton.  
**URL:** <https://www.taylorfrancis.com/books/9781466505896>
- Esch, D. C. (1996), Road and airfield design for permafrost conditions, in T. S. Vinson, J. W. Rooney & W. H. Haas, eds, ‘Roads and Airfields in Cold Regions’, ASCE Tech. Council on Cold Reg. Eng. Monog, New York, pp. 121–150.
- Farouki, O. T. (1982), Thermal properties of soils, Technical report, United States Army Corps of engineers, Cold regions research and engineering laboratory, Hanover, New Hampshire, USA.
- Fiddes, J. & Gruber, S. (2014), ‘TopoSCALE v.1.0: Downscaling gridded climate data in complex terrain’, *Geoscientific Model Development* **7**(1), 387–405.
- Fiedler, S., Stevens, B., Wieners, K.-H., Giorgetta, M., Reick, C., Jungclaus, J., Esch, M., Bittner, M., Legutke, S., Schupfner, M., Wachsmann, F., Gayler, V., Haak, H., de Vrese, P., Lorenz, S., Raddatz, T., Mauritsen, T., von Storch, J.-S., Mikolajewicz, U., Behrens, J., Brovkin, V., Claussen, M., Crueger, T., Fast, I., Hagemann, S., Hohenegger, C., Jahns, T., Kloster, S., Kinne, S., Lasslop, G., Kornblueh, L., Marotzke, J., Matei, D., Meraner, K., Modali, K., Müller, W., Nabel, J., Notz, D., Peters-von Gehlen, K., Pincus, R., Pohlmann, H., Pongratz, J., Rast, S., Schmidt, H., Schnur, R., Schulzweida, U., Six, K., Voigt, A. & Roeckner, E. (2019), ‘MPI-M MPIESM1.2-LR model output prepared for CMIP6 RFMIP’.  
**URL:** <https://doi.org/10.22033/ESGF/CMIP6.784>
- Foged, N. & Bæk-Madsen, C. (1980), Thermal Stability in uplifted marine deposits at Jakobshavn, Greenland, in ‘The 2nd International Symposium on Ground Freezing. Trondheim June 24.-26.,1980. Norwegian Institute of Technology.’, p. 10.
- Forbes, D. L., Craymer, M. R., James, T. S. & Whalen, D. (2022), ‘Subsidence drives habitat loss in a large permafrost delta, Mackenzie River outlet to the Beaufort Sea, western Arctic Canada’, *Canadian Journal of Earth Sciences* **59**(11), 914–934.
- Fortier, R., LeBlanc, A. M. & Yu, W. (2011), ‘Impacts of permafrost degradation on a road embankment at Umiujaq in Nunavik (Quebec), Canada’, *Canadian Geotechnical Journal* **48**(5), 720–740.
- Foster, A. C., Wang, J. A., Frost, G. V., Davidson, S. J., Hoy, E., Turner, K. W., Sonnentag, O., Epstein, H., Berner, L. T., Armstrong, A. H., Kang, M., Rogers, B. M., Campbell, E., Miner, K. R., Orndahl, K. M., Bourgeau-Chavez, L. L., Lutz, D. A., French, N., Chen, D., Du, J., Shestakova, T. A., Shuman, J. K., Tape, K., Virkkala, A. M., Potter, C. & Goetz, S. (2022), ‘Disturbances in North American boreal forest and Arctic tundra: impacts, interactions, and responses’, *Environmental Research Letters* **17**(11).
- Galkin, A., Pankov, V. & Zhirkova, E. (2023), ‘Thermal Conductivity of a Gravel Layer of a Road’, *E3S Web of Conferences* **371**.
- Gao, B. & Coon, E. T. (2022), ‘Evaluating simplifications of subsurface process representations for field-scale permafrost hydrology models’, *Cryosphere* **16**(10), 4141–4162.

- Gao, M., Chen, X., Li, G., Wang, J. & Dong, J. (2023), 'Impacts of elevational variability of climate and frozen ground on streamflow in a glacierized catchment in Tibetan Plateau', *Journal of Hydrology* **619**.
- Gautier, E. (2021), The impacts of climate change on the hydrological dynamics of high latitude periglacial environments, in 'Spatial Impacts of Climate Change', John Wiley & Sons, Ltd, chapter 7, pp. 143–165.
- Geo (2017), Grønlandske lufthavne, geotekniske undersøgelser, Technical Report 200648, DTU Byg, Department of Civil Engineering, Technical University of Denmark, Kgs. Lyngby.
- Geological Survey of Denmark and Greenland (GEUS) (2022), 'Map of the Ilulissat area'.  
**URL:** <https://eng.geus.dk/explore-geology/learning-about-geology/explore-ilulissat-icefjord/map-of-the-ilulissat-area>
- Gibson, C. M., Brinkman, T., Cold, H., Brown, D. & Turetsky, M. (2021), 'Identifying increasing risks of hazards for northern land-users caused by permafrost thaw: Integrating scientific and community-based research approaches', *Environmental Research Letters* **16**(6).
- Grønlands Hjemmestyre & Rambøll (2008), Veje i Grønland: Vejledning i projektering og udførelse, Technical report, Rambøll, Nuuk, Sisimiut, Qaqortoq.  
**URL:** [www.ramboll.gl](http://www.ramboll.gl)
- Grosse, G., Harden, J., Turetsky, M., McGuire, A. D., Camill, P., Tarnocai, C., Frohling, S., Schuur, E. A., Jorgenson, T., Marchenko, S., Romanovsky, V., Wickland, K. P., French, N., Waldrop, M., Bourgeau-Chavez, L. & Striegl, R. G. (2011), 'Vulnerability of high-latitude soil organic carbon in North America to disturbance', *Journal of Geophysical Research: Biogeosciences* **116**(3).
- Gruber, S. (2012), 'Derivation and analysis of a high-resolution estimate of global permafrost zonation', *The Cryosphere* **6**, 221–233.  
**URL:** [www.the-cryosphere.net/6/221/2012/](http://www.the-cryosphere.net/6/221/2012/)
- Günther, F., Overduin, P. P., Yakshina, I. A., Opel, T., Baranskaya, A. V. & Grigoriev, M. N. (2015), 'Observing Muostakh disappear: Permafrost thaw subsidence and erosion of a ground-ice-rich island in response to arctic summer warming and sea ice reduction', *Cryosphere* **9**(1), 151–178.
- Guo, C., Bentsen, M., Bethke, I., Ilicak, M., Tjiputra, J., Toniazzo, T., Schwinger, J. & Helge Otterä, O. (2019), 'Description and evaluation of NorESM1-F: A fast version of the Norwegian Earth System Model (NorESM)', *Geoscientific Model Development* **12**(1), 343–362.
- Haagmans, V. J. (2021), 'Modelling the significance of snow-vegetation interactions for active layer dynamics in an Arctic permafrost region subjected to tundra shrubification'.
- Haeberli, W. & Funk, M. (1991), 'Borehole temperatures at the Colle Gnifetti core-drilling site (Monte Rosa, Swiss Alps)', *Journal of Glaciology* **37**(125), 37–46.
- Hassn, A., Chiarelli, A., Dawson, A. & Garcia, A. (2016), 'Thermal properties of asphalt pavements under dry and wet conditions', *Materials & Design* **91**, 432–439.
- Haynes, K. M., Cannon, R. F. & Quinton, W. L. (2019), 'Hydrometeorological measurements in peatland-dominated, discontinuous permafrost at Scotty Creek, Northwest Territories, Canada', *Geoscience Data Journal* **6**(2), 85–96.

- Hillel, D. (1982), Introduction to Soil Physics, in A Subsidiary of Harcourt Brace Jovanovich, ed., 'Composite properties and behaviour', Academic Press, New York, London, Paris, San Diego, San Francisco, Sao Paulo, Sydney, Tokyo, Toronto, chapter 9, pp. 154–175.
- Hjort, J., Streletskiy, D., Doré, G., Wu, Q., Bjella, K. & Luoto, M. (2022), 'Impacts of permafrost degradation on infrastructure', *Nature Reviews Earth & Environment* **3**(1), 24–38.  
**URL:** <https://doi.org/10.1038/s43017-021-00247-8>
- Hollesen, J., Matthiesen, H. & Elberling, B. (2017), 'The Impact of Climate Change on an Archaeological Site in the Arctic', *Archaeometry* **59**(6), 1175–1189.
- Hornum, M. T. (2018), Postglacial Rebound, Permafrost Growth and its impact on Groundwater Flow and Pingo Formation - An investigation combining electrical resistivity tomography, hydro-geochemistry and decoupled heat and groundwater transport modelling, Adventdalen, Svalbard., PhD thesis, University of Copenhagen, The University Centre in Svalbard.
- iButtonLink (2023), 'DS1922L-F5# Thermochron iButton'.  
**URL:** <https://www.ibuttonlink.com/products/ds1922l>
- Ingeman-Nielsen, T. (2016), Kalibrering af termistorstrengte til boringer i Ilulissat, Technical report, Technical University of Denmark, Kgs. Lyngby.
- Ingeman-Nielsen, T. (2022), 'Exercise: Road embankments on permafrost from course 11854 of DTU'.  
**URL:** <http://files.artek.byg.dtu.dk/courses/11854/tutorials>
- Ingeman-Nielsen, T., Foged, N., Romanovsky, V., Marchenko, S., Daanen, R. & Svendsen, K. (2010), 'Geotechnical Implications of a Warming Climate in Greenland Evaluated on the Basis of Permafrost Temperature Reanalysis and Model Projections', *Proceedings of the 3rd European Conference on Permafrost* p. 612533.
- Ingeman-Nielsen, T., Kaas, M., Lorentzen, T., Scheer, J. & Tomaškovičová, S. (2022), Permafrost conditions on Storsletten , Ilulissat - Mapped using surface geophysics and boreholes, Technical report, DTU Civil Engineering, Kgs. Lyngby, Denmark.
- Ingeman-Nielsen, T., Scheer, J. & Tomaškovičová, S. (2022), Ground Temperatures : Ilulissat Season report 2021 - DRAFT, Technical report, DTU Civil Engineering, Kgs. Lyngby, Denmark.
- IUCN (2021), Peatlands and climate change, Technical Report November, International Union for Conservation of Nature, Gland.
- Iurov, F. D. & Marchenko, N. A. (2019), 'Laser scanning as a tool for monitoring road deformations in svalbard', *Proceedings of the International Conference on Port and Ocean Engineering under Arctic Conditions, POAC 2019-June*.
- Jafarov, E. E., Marchenko, S. S. & Romanovsky, V. E. (2012), 'Numerical modeling of permafrost dynamics in Alaska using a high spatial resolution dataset', *The Cryosphere* **6**(3), 613–624.
- Jørgensen, A. S., Doré, G., Voyer, E., Chataigner, Y. & Gosselin, L. (2008), 'Assessment of the effectiveness of two heat removal techniques for permafrost protection', *Cold Regions Science and Technology* **53**(2), 179–192.

- Jungsberg, L., Byskov Herslund, L., Nilsson, K., Wang, S., Tomaškovičová, S., Madsen, K., Scheer, J. & Ingeman-Nielsen, T. (2022), 'Adaptive capacity to manage permafrost degradation in North-west Greenland', *Polar Geography* p. 19.  
**URL:** <https://www.tandfonline.com/action/journalInformation?journalCode=tpog20>
- Kelley, J. & Weaver, D. (1969), 'Physical Processes at the Surface of the Arctic Tundra', *ARCTIC* **22**(4), 425–437.  
**URL:** <https://journalhosting.ucalgary.ca/index.php/arctic/article/view/66284>
- Kokelj, S. V., Kokoszka, J., Van Der Sluijs, J., Rudy, A. C., Tunnicliffe, J., Shakil, S., Tank, S. E. & Zolkos, S. (2021), 'Thaw-driven mass wasting couples slopes with downstream systems, and effects propagate through Arctic drainage networks', *Cryosphere* **15**(7), 3059–3081.
- Kong, X. & Doré, G. (2021), 'Thermal Stabilization of Embankments Built on Thaw-Sensitive Permafrost', *Journal of Cold Regions Engineering* **35**(3), 1–8.
- Kong, X., Doré, G. & Calmels, F. (2018), 'Thermal modeling of heat balance through embankments in permafrost regions', *Cold Regions Science and Technology* **158**(August 2018), 117–127.  
**URL:** <https://doi.org/10.1016/j.coldregions.2018.11.013>
- Langer, M., Westermann, S., Boike, J., Kirillin, G., Grosse, G., Peng, S. & Krinner, G. (2016), 'Rapid degradation of permafrost underneath waterbodies in tundra landscapes—Toward a representation of thermokarst in land surface models', *Journal of Geophysical Research: Earth Surface* **121**(12), 2446–2470.  
**URL:** <https://onlinelibrary.wiley.com/doi/abs/10.1002/2016JF003956>
- Langer, M., Westermann, S., Heikenfeld, M., Dorn, W. & Boike, J. (2013), 'Satellite-based modeling of permafrost temperatures in a tundra lowland landscape', *Remote Sensing of Environment* **135**, 12–24.
- Langer, M., Westermann, S., Muster, S., Piel, K. & Boike, J. (2011), 'The surface energy balance of a polygonal tundra site in northern Siberia - Part 1: Spring to fall', *Cryosphere* **5**(1), 151–171.
- Lavrillier, A. & Gabyshev, S. (2021), 'An Indigenous science of the climate change impacts on landscape topography in Siberia', *Ambio* **50**(11), 1910–1925.
- Lawrence, D. M., Slater, A. G., Romanovsky, V. E. & Nicolsky, D. J. (2008), 'Sensitivity of a model projection of near-surface permafrost degradation to soil column depth and representation of soil organic matter', *Journal of Geophysical Research: Earth Surface* **113**(F2).  
**URL:** <https://onlinelibrary.wiley.com/doi/full/10.1029/2007JF000883>
- Lawrence, D. M., Slater, A. G. & Swenson, S. C. (2012), 'Simulation of Present-Day and Future Permafrost and Seasonally Frozen Ground Conditions in CCSM4', *Journal of Climate* **25**(7), 2207–2225.  
**URL:** <https://journals.ametsoc.org/view/journals/clim/25/7/jcli-d-11-00334.1.xml>
- Li, G., Ma, W., Wang, F., Jin, H., Fedorov, A., Chen, D., Wu, G., Cao, Y., Zhou, Y., Mu, Y., Mao, Y., Zhang, J., Gao, K., Jin, X., He, R., Li, X. & Li, Y. (2022), 'A newly integrated ground temperature dataset of permafrost along the China-Russia crude oil pipeline route in Northeast China', *Earth System Science Data* **14**(11), 5093–5110.

- Lima, O., Freitas, E., Cardoso, P., Segundo, I. R., Margalho, E., Moreira, L., José, J. H., Landi, S. & Carneiro, J. (2023), 'Mitigation of Urban Heat Island Effects by Thermochromic Asphalt Pavement', *Coatings* **13**(1).
- Lin, Z., Niu, F., Liu, H. & Lu, J. (2011), 'Disturbance-related thawing of a ditch and its influence on roadbeds on permafrost', *Cold Regions Science and Technology* **66**(2-3), 105–114.
- Liu, S., Wu, T., Wang, X., Wu, X., Yao, X., Liu, Q., Zhang, Y., Wei, J. & Zhu, X. (2020), 'Changes in the global cryosphere and their impacts: A review and new perspective', *Sciences in Cold and Arid Regions* **12**(6), 343–354.
- Luo, Q., Wu, P. & Wang, T. (2019), 'Evaluating frost heave susceptibility of well-graded gravel for HSR subgrade based on orthogonal array testing', *Transportation Geotechnics* **21**.
- Lytkin, V., Suleymanov, A., Vinokurova, L., Grigorev, S., Golomareva, V., Fedorov, S., Kuzmina, A. & Syromyatnikov, I. (2021), 'Influence of permafrost landscapes degradation on livelihoods of Sakha Republic (Yakutia) rural communities', *Land* **10**(2), 1–22.
- Mackay, J. R. (1993), 'Air temperature, snow cover, creep of frozen ground, and the time of ice-wedge cracking, western Arctic coast', *Canadian Journal of Earth Sciences* **30**(8), 1720–1729.
- Malenfant-Lepage, J., Doré, G., Fortier, D. & Murchison, P. (2012), Thermal Performance of the Permafrost Protection Techniques at Beaver Creek Experimental Road Site, Yukon, Canada, in 'Tenth International Conference on Permafrost', The Northern Publisher, pp. 261–266.
- Martel, J. L., Brissette, F., Troin, M., Arsenault, R., Chen, J., Su, T. & Lucas-Picher, P. (2022), 'CMIP5 and CMIP6 Model Projection Comparison for Hydrological Impacts Over North America', *Geophysical Research Letters* **49**(15), e2022GL098364.  
**URL:** <https://onlinelibrary.wiley.com/doi/full/10.1029/2022GL098364>
- Martin, L. C. P., Nitzbon, J., Scheer, J., Aas, K. S., Eiken, T., Langer, M., Filhol, S., Etzelmüller, B. & Westermann, S. (2021), 'Lateral thermokarst patterns in permafrost peat plateaus in northern Norway', *The Cryosphere* **15**(7), 3423–3442.  
**URL:** <https://tc.copernicus.org/articles/15/3423/2021/>
- McGuire, A. D., Lawrence, D. M., Koven, C., Clein, J. S., Burke, E., Chen, G., Jafarov, E., MacDougall, A. H., Marchenko, S., Nicolsky, D., Peng, S., Rinke, A., Ciais, P., Gouttevin, I., Hayes, D. J., Ji, D., Krinner, G., Moore, J. C., Romanovsky, V., Schädel, C., Schaefer, K., Schuur, E. A. & Zhuang, Q. (2018), 'Dependence of the evolution of carbon dynamics in the northern permafrost region on the trajectory of climate change', *Proceedings of the National Academy of Sciences of the United States of America* **115**(15), 3882–3887.  
**URL:** <https://www.pnas.org/doi/abs/10.1073/pnas.1719903115>
- Mętrak, M., Chachulski, L., Pawlikowski, P., Rojan, E., Sulwiński, M. & Suska-Malawska, M. (2023), 'Potential role of high-altitude wetlands in preservation of plant biodiversity under changing climatic conditions in the arid Eastern Pamir', *Catena* **220**.
- Monteux, S., Mariën, J. & Krab, E. J. (2022), 'Dispersal of bacteria and stimulation of permafrost decomposition by Collembola', *Biogeosciences* **19**(17), 4089–4105.

National Centers for Environmental Information (NCEI) (2022), ‘Climate Forcing’.

**URL:** <https://www.ncei.noaa.gov/products/paleoclimatology/climate-forcing>

National Snow and Ice Data Center (2023a), ‘Excess Ice’.

**URL:** <https://nsidc.org/learn/cryosphere-glossary/excess-ice>

National Snow and Ice Data Center (2023b), ‘massive ice’.

**URL:** <https://nsidc.org/learn/cryosphere-glossary/massive-ice>

National Snow and Ice Data Center (2023c), ‘Science of Frozen Ground’.

**URL:** <https://nsidc.org/learn/parts-cryosphere/frozen-ground-permafrost/science-frozen-ground>

Nicu, I. C., Lombardo, L. & Rubensdotter, L. (2021), ‘Preliminary assessment of thaw slump hazard to Arctic cultural heritage in Nordenskiöld Land, Svalbard’, *Landslides* **18**(8), 2935–2947.

Nicu, I. C., Tanyas, H., Rubensdotter, L. & Lombardo, L. (2022), ‘A glimpse into the northernmost thermo-erosion gullies in Svalbard archipelago and their implications for Arctic cultural heritage’, *Catena* **212**.

Nitzbon, J., Langer, M., Martin, L. C. P., Westermann, S., von Deimling, T. & Boike, J. (2021), ‘Effects of multi-scale heterogeneity on the simulated evolution of ice-rich permafrost lowlands under a warming climate’, *The Cryosphere* **15**(3), 1399–1422.

**URL:** <https://tc.copernicus.org/articles/15/1399/2021/>

Nitzbon, J., Langer, M., Westermann, S., Martin, L., Aas, K. S. & Boike, J. (2019), ‘Pathways of ice-wedge degradation in polygonal tundra under different hydrological conditions’, *The Cryosphere* **13**(4), 1089–1123.

**URL:** <https://tc.copernicus.org/articles/13/1089/2019/>

Nitzbon, J., Westermann, S., Langer, M., Martin, L. C. P., Strauss, J., Laboor, S. & Boike, J. (2020), ‘Fast response of cold ice-rich permafrost in northeast Siberia to a warming climate’, *Nature Communications* **11**(1), 2201.

**URL:** <https://doi.org/10.1038/s41467-020-15725-8>

Noetzli, J., Arenson, L. U., Bast, A., Beutel, J., Delaloye, R., Farinotti, D., Gruber, S., Gubler, H., Haeberli, W., Hasler, A., Hauck, C., Hiller, M., Hoelzle, M., Lambiel, C., Pellet, C., Springman, S. M., Vonder Muehll, D. & Phillips, M. (2021), ‘Best Practice for Measuring Permafrost Temperature in Boreholes Based on the Experience in the Swiss Alps’, *Frontiers in Earth Science* **9**, 280.

NorESM (2016), ‘About NorESM’.

**URL:** <https://www.noresm.org/about/>

Obu, J. (2021), ‘How Much of the Earth’s Surface is Underlain by Permafrost?’, *Journal of Geophysical Research: Earth Surface* **126**(5).

**URL:** <https://onlinelibrary.wiley.com/doi/full/10.1029/2021JF006123>

Obu, J., Westermann, S., Bartsch, A., Berdnikov, N., Christiansen, H. H., Dashtseren, A., Delaloye, R., Elberling, B., Etzelmüller, B., Kholodov, A., Khomutov, A., Kääb, A., Leibman, M. O., Lewkowicz, A. G., Panda, S. K., Romanovsky, V., Way, R. G., Westergaard-Nielsen, A., Wu, T., Yamkhin, J. & Zou, D. (2019), ‘Northern Hemisphere permafrost map based on TTOP modelling for 2000–2016 at 1 km<sup>2</sup> scale’, *Earth-Science Reviews* **193**, 299–316.

- Osterkamp, T. E. & Sherman, D. (2019), Sub-sea Permafrost, in 'Encyclopedia of Ocean Sciences', 6 edn, Vol. 3, Academic Press, pp. 219–230.
- Overduin, P. P., Schneider von Deimling, T., Miesner, F., Grigoriev, M. N., Ruppel, C., Vasiliev, A., Lantuit, H., Juhls, B. & Westermann, S. (2019), 'Submarine Permafrost Map in the Arctic Modeled Using 1-D Transient Heat Flux (SuPerMAP)', *Journal of Geophysical Research: Oceans* **124**(6), 3490–3507.
- O'Neill, H. B. & Burn, C. R. (2017), 'Impacts of variations in snow cover on permafrost stability, including simulated snow management, Dempster Highway, Peel Plateau, Northwest Territories<sup>1</sup>', <https://doi.org/10.1139/as-2016-0036> **3**(2), 150–178.  
**URL:** <https://cdnsiencepub.com/doi/10.1139/as-2016-0036>
- Painter, S. L. & Karra, S. (2014), 'Constitutive Model for Unfrozen Water Content in Subfreezing Unsaturated Soils', *Vadose Zone Journal* **13**(4), 1–8.  
**URL:** <https://onlinelibrary.wiley.com/doi/full/10.2136/vzj2013.04.0071>
- Parent, M., Doré, G., Lemieux, C., De Guzman, E. M. B. & Alfaro, M. C. (2019), 'Preliminary Investigation for Mechanical Degradation of Permafrost Embankment: Inuvik Tuktoyaktuk Highway Case Study', *Cold Regions Engineering* pp. 186–194.
- PCMDI (2023), 'CMIP5 Overview'.  
**URL:** <https://pcmdi.llnl.gov/mips/cmip5/>
- Plach, A., Nisancioglu, K. H., Le Clec'h, S., Born, A., Langebroek, P. M., Guo, C., Imhof, M. & Stocker, T. F. (2018), 'Eemian Greenland SMB strongly sensitive to model choice', *Climate of the Past* **14**(10), 1463–1485.
- Pörtner, H.-O., Roberts, D. C., Adams, H., Adler, C., Aldunce, P., Ali, E., Begum, R. A., Betts, R., Kerr, R. B., Biesbroek, R. & others (2022), IPCC 2022: Summary for Policymakers, in 'Climate Change 2022: Impacts, Adaptation and Vulnerability. Contribution of Working Group II to the Sixth Assessment Report of the Intergovernmental Panel on Climate Change', Cambridge University Press, Cambridge, UK and New York, NY, USA, pp. 3–33.
- Qin, Y., Liang, J., Huang, Z. & Tan, K. (2016), 'Painting the roadway embankment with non-white high reflective pigments to raise the albedo', *Environmental Earth Sciences* **75**(4), 1–7.
- Qin, Y., Liang, J., Luo, Z., Tan, K. & Zhu, Z. (2016), 'Increasing the southern side-slope albedo remedies thermal asymmetry of cold-region roadway embankments', *Cold Regions Science and Technology* **123**, 115–120.
- Qin, Y., Tan, K., Yang, H. & Li, F. (2016), 'The albedo of crushed-rock layers and its implication to cool roadbeds in permafrost regions', *Cold Regions Science and Technology* **128**, 32–37.
- Ran, Q., Aires, F., Ciais, P., Qiu, C., Hu, R., Fu, Z., Xue, K. & Wang, Y. (2023), 'The Status and Influencing Factors of Surface Water Dynamics on the Qinghai-Tibet Plateau During 2000-2020', *IEEE Transactions on Geoscience and Remote Sensing* **61**.
- Rasch, M. (2000), 'Holocene Relative Sea Level Changes in Disko Bugt, West Greenland', *Journal of Coastal Research* **16**(2), 306–315.  
**URL:** <https://www.jstor.org/stable/4300039>

- Riahi, K., van Vuuren, D. P., Kriegler, E., Edmonds, J., O'Neill, B. C., Fujimori, S., Bauer, N., Calvin, K., Dellink, R., Fricko, O., Lutz, W., Popp, A., Cuaresma, J. C., KC, S., Leimbach, M., Jiang, L., Kram, T., Rao, S., Emmerling, J., Ebi, K., Hasegawa, T., Havlik, P., Humpenöder, F., Da Silva, L. A., Smith, S., Stehfest, E., Bosetti, V., Eom, J., Gernaat, D., Masui, T., Rogelj, J., Strefler, J., Drouet, L., Krey, V., Luderer, G., Harmsen, M., Takahashi, K., Baumstark, L., Doelman, J. C., Kainuma, M., Klimont, Z., Marangoni, G., Lotze-Campen, H., Obersteiner, M., Tabeau, A. & Tavoni, M. (2017), 'The Shared Socioeconomic Pathways and their energy, land use, and greenhouse gas emissions implications: An overview', *Global Environmental Change* **42**, 153–168.
- Rolph, R., Overduin, P. P., Ravens, T., Lantuit, H. & Langer, M. (2022), 'ArcticBeach v1.0: A physics-based parameterization of pan-Arctic coastline erosion', *Frontiers in Earth Science* **10**.
- Rosenfeld, A. H., Akbari, H., Bretz, S., Fishman, B. L., Kurn, D. M., Sailor, D. & Taha, H. (1995), 'Mitigation of urban heat islands: materials, utility programs, updates', *Energy and Buildings* **22**(3), 255–265.
- Scheer, J. (2019), Summer fieldwork Ilulissat, October 2019 - Technical report, Technical report, DTU Byg Technical Reports, Kgs. Lyngby, Denmark.
- Scheer, J. (2020), Summer Fieldwork Ilulissat, September 2020 - Technical report, Technical report, DTU Byg Technical Reports, Kgs. Lyngby, Denmark.
- Scheer, J. & Ingeman-Nielsen, T. (2022), Classification of frozen cores from Ilulissat, Greenland - Boreholes drilled in 2018 and 2021, Technical report, Technical University of Denmark, Kgs. Lyngby.
- Scheer, J., Ingeman-Nielsen, T. & Tomaskovicova, S. (2021), Multi-disciplinary hazard mapping framework for critical infrastructure on permafrost, Ilulissat, West-Greenland, in 'Abstract from Arctic Science Summit Week 2021', pp. 10–10.
- Schneider von Deimling, T., Lee, H., Ingeman-Nielsen, T., Westermann, S., Romanovsky, V., Lamoureux, S., Walker, D. A., Chadburn, S., Trochim, E., Cai, L., Nitzbon, J., Jacobi, S. & Langer, M. (2021), 'Consequences of permafrost degradation for Arctic infrastructure - Bridging the model gap between regional and engineering scales', *Cryosphere* **15**(5), 2451–2471.
- Schruben, L. W. (1982), 'Detecting Initialization Bias in Simulation Output', *Operations Research* **30**(3), 569–590.
- Schupfner, M., Wieners, K.-H., Wachsmann, F., Steger, C., Bittner, M., Jungclaus, J., Früh, B., Pankatz, K., Giorgetta, M., Reick, C., Legutke, S., Esch, M., Gayler, V., Haak, H., de Vrese, P., Raddatz, T., Mauritsen, T., von Storch, J.-S., Behrens, J., Brovkin, V., Claussen, M., Crueger, T., Fast, I., Fiedler, S., Hagemann, S., Hohenegger, C., Jahns, T., Kloster, S., Kinne, S., Lasslop, G., Kornbluh, L., Marotzke, J., Matei, D., Meraner, K., Mikolajewicz, U., Modali, K., Müller, W., Nabel, J., Notz, D., Peters-von Gehlen, K., Pincus, R., Pohlmann, H., Pongratz, J., Rast, S., Schmidt, H., Schnur, R., Schulzweida, U., Six, K., Stevens, B., Voigt, A. & Roeckner, E. (2019), 'DKRZ MPI-ESM1.2-HR model output prepared for CMIP6 ScenarioMIP'.  
**URL:** <https://doi.org/10.22033/ESGF/CMIP6.2450>
- Schuur, E. A. & Abbott, B. (2011), 'Climate change: High risk of permafrost thaw'.

- Schuur, E. A., Bockheim, J., Canadell, J. G., Euskirchen, E., Field, C. B., Goryachkin, S. V., Hagemann, S., Kuhry, P., Laflour, P. M., Lee, H., Mazhitova, G., Nelson, F. E., Rinke, A., Romanovsky, V. E., Shiklomanov, N., Tarnocai, C., Venevsky, S., Vogel, J. G. & Zimov, S. A. (2008), 'Vulnerability of permafrost carbon to climate change: Implications for the global carbon cycle', *BioScience* **58**(8), 701–714.
- Schuur, E. A. & Mack, M. C. (2018), 'Ecological response to permafrost thaw and consequences for local and global ecosystem services', *Annual Review of Ecology, Evolution, and Systematics* **49**, 279–301.
- Schuur, E. A., Vogel, J. G., Crummer, K. G., Lee, H., Sickman, J. O. & Osterkamp, T. E. (2009), 'The effect of permafrost thaw on old carbon release and net carbon exchange from tundra', *Nature* **459**(7246), 556–559.
- Schwamborn, G., Schirrmeister, L., Mohammadi, A., Meyer, H., Kartozia, A., Maggioni, F. & Strauss, J. (2023), 'Fluvial and permafrost history of the lower Lena River, north-eastern Siberia, over late Quaternary time', *Sedimentology* **70**(1), 235–258.
- Seland, O., Bentsen, M., Olivie, D., Toniazzo, T., Gjermundsen, A., Graff, L. S., Debernard, J. B., Gupta, A. K., He, Y. C., Kirkevåg, A., Schwinger, J., Tjiputra, J., Schanke Aas, K., Bethke, I., Fan, Y., Griesfeller, J., Grini, A., Guo, C., Ilicak, M., Karset, I. H. H., Landgren, O., Liakka, J., Moseid, K. O., Nummelin, A., Spensberger, C., Tang, H., Zhang, Z., Heinze, C., Iversen, T. & Schulz, M. (2020), 'Overview of the Norwegian Earth System Model (NorESM2) and key climate response of CMIP6 DECK, historical, and scenario simulations', *Geoscientific Model Development* **13**(12), 6165–6200.
- Sturm, M., Taras, B., Liston, G. E., Derksen, C., Jonas, T. & Lea, J. (2010), 'Estimating Snow Water Equivalent Using Snow Depth Data and Climate Classes', *Journal of Hydrometeorology* **11**(6), 1380–1394.
- Tai, B., Liu, J., Wang, T., Tian, Y. & Fang, J. (2017), 'Thermal characteristics and declining permafrost table beneath three cooling embankments in warm permafrost regions', *Applied Thermal Engineering* **123**, 435–447.
- Tarnocai, C., Canadell, J. G., Schuur, E. A., Kuhry, P., Mazhitova, G. & Zimov, S. (2009), 'Soil organic carbon pools in the northern circumpolar permafrost region', *Global Biogeochemical Cycles* **23**(2).
- Taylor, K. E., Stouffer, R. J. & Meehl, G. A. (2012), 'An overview of CMIP5 and the experiment design', *Bulletin of the American Meteorological Society* **93**(4), 485–498.
- Timlin, U., Ingimundarson, J. H., Jungsberg, L., Kauppila, S., Larsen, J. N., Nordström, T., Scheer, J., Schweitzer, P. & Rautio, A. (2021), 'Living conditions and mental wellness in a changing climate and environment: focus on community voices and perceived environmental and adaptation factors in Greenland', *Heliyon* **7**(4), e06862.
- Tomaskovicova, S., Scheer, J. & Ingeman-Nielsen, T. (2021), Basic vs. applied science for effective climate adaptation-narrowing the gap, in 'Abstract from Arctic Science Summit Week 2021', pp. 4–4.

- Treat, C. C., Jones, M. C., Alder, J. & Frolking, S. (2022), 'Hydrologic Controls on Peat Permafrost and Carbon Processes: New Insights From Past and Future Modeling', *Frontiers in Environmental Science* **10**.
- Varlamov, S., Skryabin, P., Zhirkov, A. & Wen, Z. (2022), 'Monitoring the Permafrost Conditions along Pipeline Routes in Central Yakutia, Russia', *Land* **11**(12).
- Villumsen, A., Jørgensen, A. S., Barten, A., Fritt-Rasmussen, J., Løgstrup, L., Brock, N., Hoedeman, N., Gunnarsdottir, R., Borre, S. & Ingeman-Nielsen, T. (2007), Road construction in Greenland - The Greenlandic Case, Technical report, ROADDEX III The Northern Periphery Research and Arctic Technology Center, Sisimiut.  
**URL:** <http://www.roadex.org/wp-content/uploads/2014/01/The-Greenlandic-Case-RIII.pdf>
- Wang, G. (2017), 'Common Problems in Construction of Road and Bridge and the Application of Quality Inspection Technology', **130**, 284–287.
- Wang, J., Zhang, M., You, Z., Pei, W. & Bai, R. (2019), 'A developed method to measure and calculate the solar albedo of discrete-particle layers', *Solar Energy* **194**, 671–681.
- Wang, S., He, X., Kang, S., Yan, F., Fu, H., Hong, X., Xue, Y. & Feng, Z. (2023), 'Insights into the streamwater age in the headwater catchments covered by glaciers and permafrost, Central Tibetan Plateau', *Science of the Total Environment* **866**.
- Wang, S. J., Chen, J. B., Zhang, J. Z. & Li, Z. L. (2009), 'Development of highway constructing technology in the permafrost region on the Qinghai-Tibet plateau', *SCIENCE IN CHINA PRESS* **52**(2), 497–506.  
**URL:** [www.scichina.com](http://www.scichina.com)
- Wang, S., Jin, L., Peng, H., Chen, J. & Mu, K. (2017), 'Damage analysis of the characteristics and development process of thermosiphon embankment along the Qinghai-Tibet Highway', *Cold Regions Science and Technology* **142**, 118–131.
- Wang, X., Yu, Q., Ma, J., Yang, L., Liu, W. & Li, J. (2022), 'Study and Prediction of Surface Deformation Characteristics of Different Vegetation Types in the Permafrost Zone of Linzhi, Tibet', *Remote Sensing* **14**(18).
- Webb, E. E., Liljedahl, A. K., Cordeiro, J. A., Loranty, M. M., Witharana, C. & Lichstein, J. W. (2022), 'Permafrost thaw drives surface water decline across lake-rich regions of the Arctic', *Nature Climate Change* **12**(9), 841–846.
- Weidick, A. & Bennike, O. (2007), 'Quaternary glaciation history and glaciology of Jakobshavn Isbræ and the Disko Bugt region, West Greenland: A review', *Geological Survey of Denmark and Greenland Bulletin* **1**(14), 1–78.
- Westermann, S., Aalstad, K., Zweigel, R. B., Renette, C., Schmidt, L. S., Aga, J., Nitzbon, J., Angelopoulos, M., Stuenzi, S. M., Chaudhary, N., Miesner, F., Martin, L., Morard, S., Ben-Asher, M., Kääb, A., Ingeman-Nielsen, T., Groenke, B., Boike, J., Scheer, J., Overduin, P., Filhol, S. & Langer, M. (2022), 'The CryoGrid community model (version 1.0) – a multi-physics toolbox for climate-driven simulations in the terrestrial cryosphere', *Geoscientific Model Developmen. preprint* **2022**(June), 1–61.  
**URL:** <https://gmd.copernicus.org/preprints/gmd-2022-127/>

- Westermann, S., Ingeman-Nielsen, T., Scheer, J., Aalstad, K., Aga, J., Chaudhary, N., Etzelmüller, B., Filhol, S., Kääb, A., Renette, C., Schmidt, L. S., Schuler, T. V., Zweigel, R. B., Martin, L., Morard, S., Ben-Asher, M., Angelopoulos, M., Boike, J., Groenke, B., Miesner, F., Nitzbon, J., Overduin, P., Stuenzi, S. M. & Langer, M. (2023), 'The CryoGrid community model (version 1.0)-a multi-physics toolbox for climate-driven simulations in the terrestrial cryosphere', *Geosci. Model Dev* **16**, 2607–2647.  
**URL:** <https://doi.org/10.5194/gmd-16-2607-2023>
- Westermann, S., Langer, M., Boike, J., Heikenfeld, M., Peter, M., Etzelmüller, B. & Krinner, G. (2016), 'Simulating the thermal regime and thaw processes of ice-rich permafrost ground with the land-surface model CryoGrid 3', *Geoscientific Model Development* **9**(2), 523–546.  
**URL:** <https://gmd.copernicus.org/articles/9/523/2016/>
- Yun, H., Zhu, Q., Tang, J., Zhang, W., Chen, D., Ciais, P., Wu, Q. & Elberling, B. (2023), 'Warming, permafrost thaw and increased nitrogen availability as drivers for plant composition and growth across the Tibetan Plateau', *Soil Biology and Biochemistry* **182**.
- Zeinali, A., Dagli, D. & Edeskär, T. (2016), 'Freezing-thawing laboratory testing of frost susceptible soils', *Proceedings of the 17th Nordic Geotechnical Meeting* pp. 267–276.
- Zotikov, I. A. (1986), *The thermophysics of glaciers*, D. Reidel Pub. Co.  
**URL:** <https://link.springer.com/book/9789027721631>

# Appendices

## A Dalton Highway, Alaska

In order to get to know the CryoGrid Community Model and to better understand the processes as well as the integration of all necessary input parameters, I aimed to recreate the simulation by Schneider von Deimling et al. (2021). In their study, the Dalton Highway in Alaska is modelled using the previous version CryoGrid 3. The modelled half cross section is shown in Figure 73. Schneider von Deimling et al. (2021) divides their model into 4 structural units with different compositions. Different experiments are simulated. These range from low resolution (2 tiles: road and tundra) to medium resolution (5 tiles: see Figure 73) to high resolution (30 tiles: see Figure 74). In addition, a distinction is made between the conservative case (snow accumulation at shoulder and toe) and the vulnerable case (snow accumulation at shoulder and toe, ponding at toe, southern facing shoulder) (Schneider von Deimling et al. 2021). In this work, all parameters of CryoGrid 3 were first transferred to the community version. Initially, only 4 tiles were used, as the model uses parallel computing and is thus strongly limited by the computing power, especially the number of cores of the computer. As soon as a model run was running locally, the setup was extended by one tile to the medium resolution approach. This could then be calculated on the AWI server, although licensing problems regularly occurred here as well. A 16 tiles run was carried out as a test. However, this is not presented here.

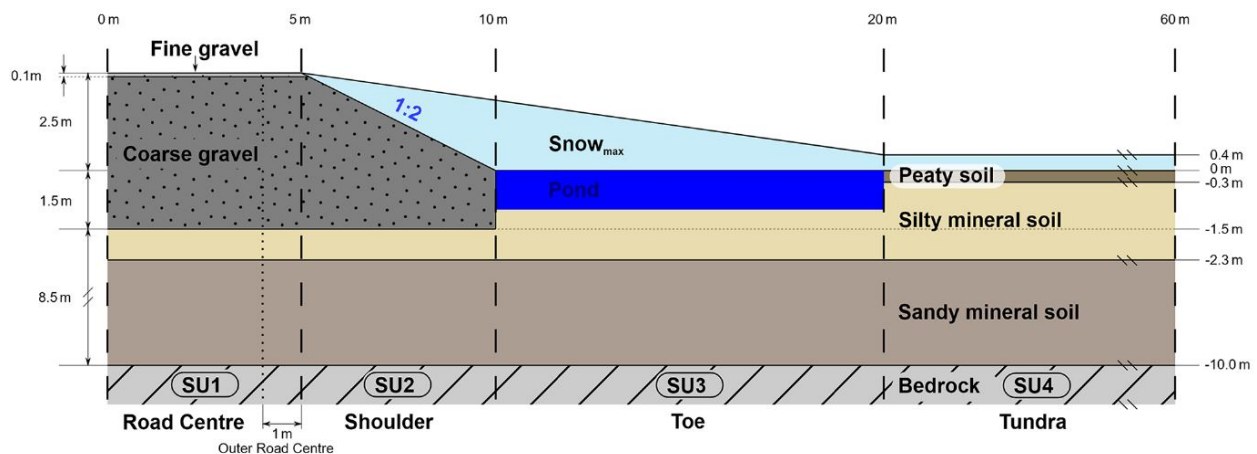


Figure 73: Modelled half cross section from the road centre to the adjacent tundra in Dalton. (Schneider von Deimling et al. 2021)

In Figure 74 the results of the simulated ground temperature of Schneider von Deimling et al. (2021) and my simulation with the CryoGrid Community Model were compared. The parameters of my simulation are the same as in Schneider von Deimling et al. (2021), I compare here the conservative case with no excess ice, i.e. no ponding. I compare the high resolution 30 tile setting with my medium resolution 5 tile setting, which does not reflect the transition and progression so well. Basically it can be said that the results are very similar. Both simulations show similar temperatures and thaw depths for the past (year 2000). In 2020, no emerging talik formation is apparent for both models, but the ground is not yet thawed in winter. For the scenario in summer, this is equally evident for the results of Schneider von Deimling et al. (2021) at the transition from

shoulder to toe, whereas my model runs are not so well resolved to detect such a process. In the future (2050 and 2075) fundamentally similar processes are observable, but in the own simulation somewhat weaker than in the original from the paper. Already in 2050 there are thaw depths of 4m and a pronounced thaw bubble with temperatures slightly above 0 °C. This is strengthened in 2075 and the thaw depth is at 5 m with a thaw bubble of about 4 m diameter and temperatures above 0.5 °C. In my own simulation, the thaw bubble forms in the same area - mainly toe and shoulder, remaining just below 0 °C in 2050, but is elevated in thaw. The thaw depth is just below 2 m. For 2075, the bubble has actually thawed and is about 3 m in diameter. The thaw depth at the end of the summer is just under 4 m. Since this is the vulnerable setting of Schneider von Deimling et al. (2021), it is to be expected that the own model without excess ice underestimates this case.

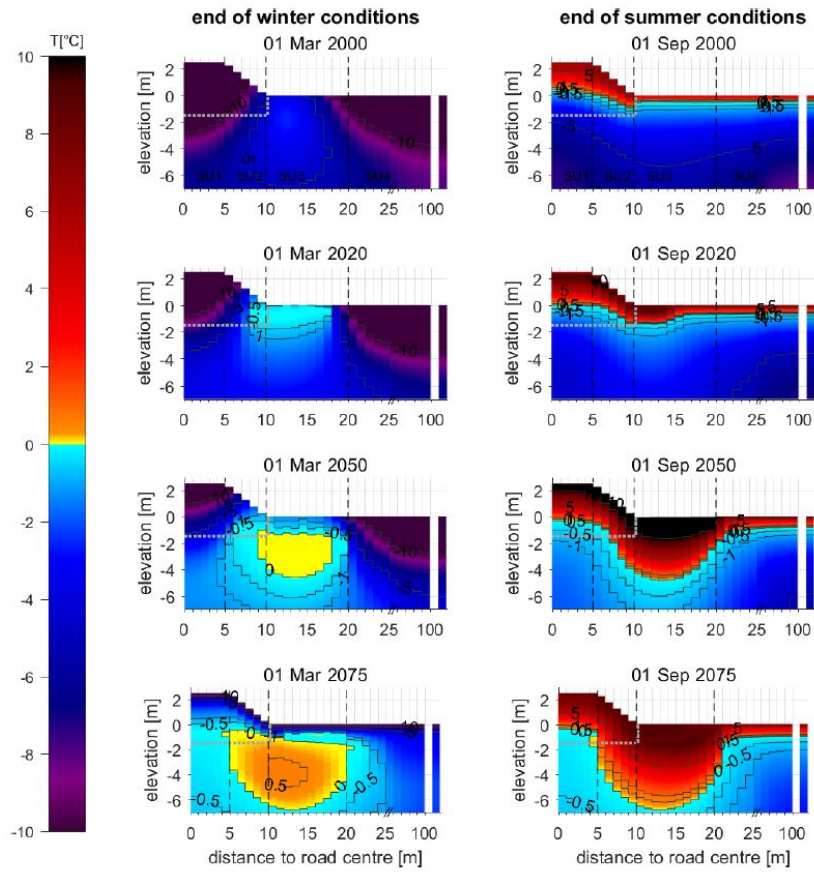


Figure 74: Simulated ground temperatures for the Dalton Highway by Schneider von Deimling et al. (2021) in the road embankment, subgrade, and adjacent tundra at the end of winter (left) and summer (right) for past (uppermost panels), present day (upper mid-panel), and future (lower two panels) climate conditions (based on the RCP8.5 scenario).

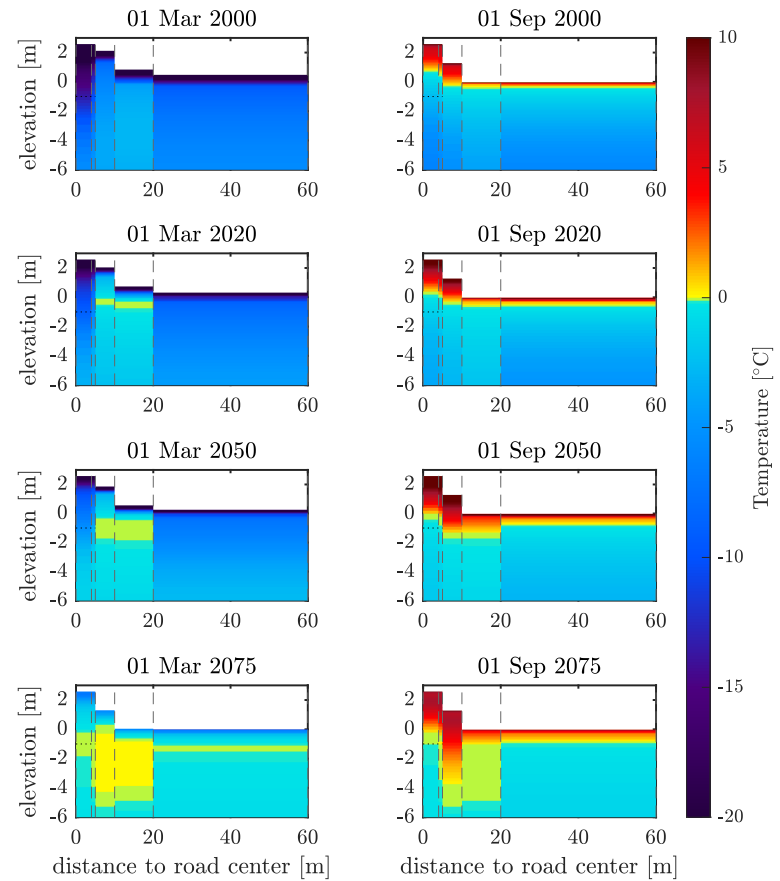


Figure 75: Simulated ground temperatures for the Dalton Highway by myself in the road embankment, subgrade, and adjacent tundra at the end of winter (left) and summer (right) for past (uppermost panels), present day (upper mid-panel), and future (lower two panels) climate conditions (based on the RCP8.5 scenario).

In Figure 76 and 77, the conservative case of Schneider von Deimling et al. (2021) and that of my own simulation are compared in terms of MTD. Both show very similar behavior. The tundra tile has a regular increase of AL, whereas all other tiles experience a drastic increase after a certain point in time. For the outer road and road this drop is after 2070 and 2080 respectively. For the road, there is a deviation of just under 10 years here. Shoulder and toe are more affected by the increase in MTD and drop after 2050 for both comparison scenarios.

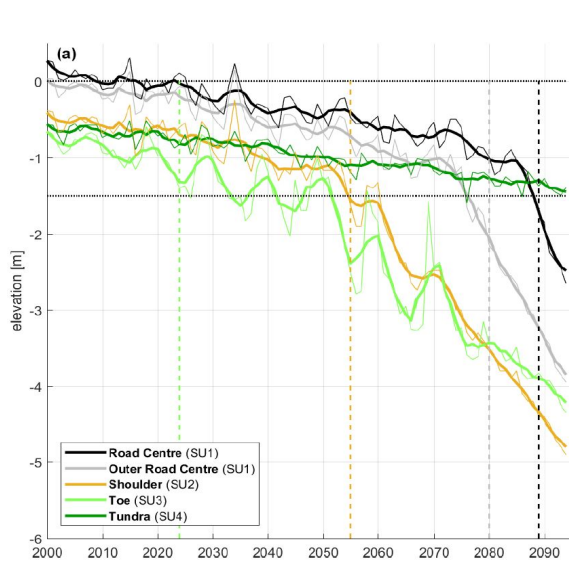


Figure 76: Temporal evolution of maximum thaw depth (MTD) for Dalton Highway from Schneider von Deimling et al. (2021) for all structural units under RCP8.5 warming - conservative case without ponding at the toe.

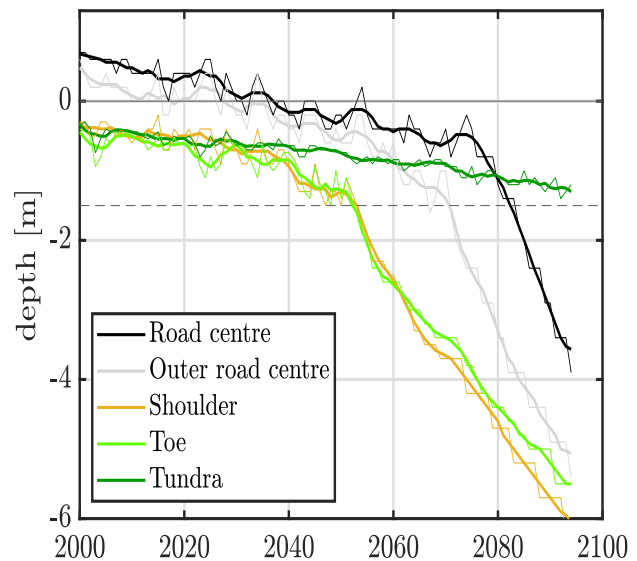


Figure 77: Temporal evolution of maximum thaw depth (MTD) for Dalton Highway from my model results for all structural units under RCP8.5 warming - conservative case without ponding at the toe.

For the comparison of the vulnerable case, excess ice was added at a depth between 1 m and 2 m as in the study of Schneider von Deimling et al. (2021). This scenario is now closer to the vulnerable case presented in Figure 74. The thaw bubble has already developed slightly positive temperatures in winter 2050, which will be enhanced in 2075 with higher temperatures and a diameter above 5 m (see Figure 78). Also, the MTD for the toe exceeds 6 m depth. The gravel layer of the road is still sufficiently thick.

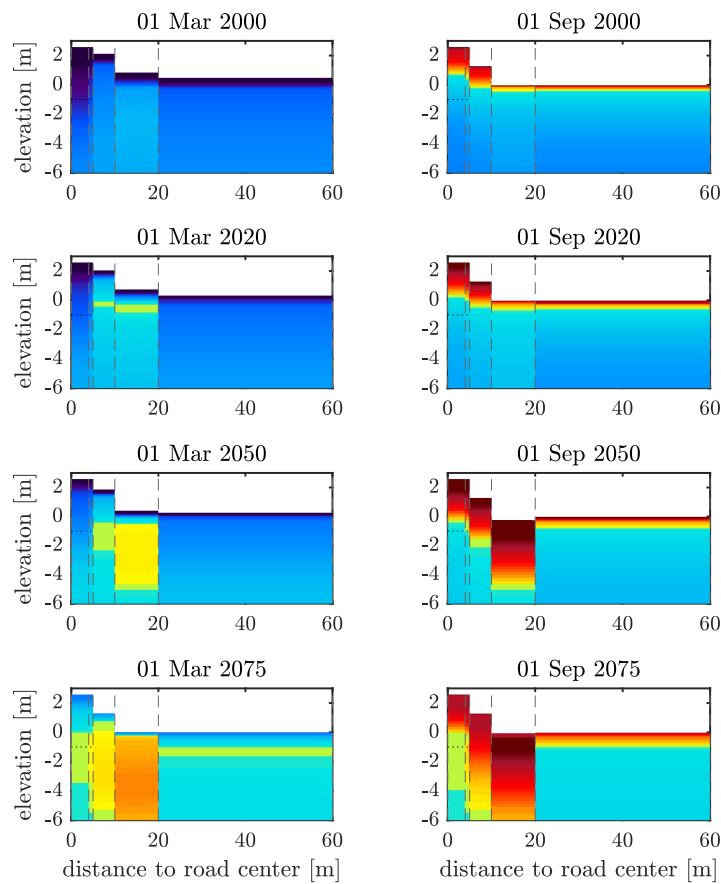


Figure 78: Simulated ground temperatures for the Dalton Highway by myself (with excess ice) in the road embankment, toe, and adjacent tundra at the end of winter (left) and summer (right) for past (uppermost panels), present day (upper mid-panel), and future (lower two panels) climate conditions (based on the RCP8.5 scenario).

The MTD for the vulnerable case with excess ice in the own simulated model is similar for the course and the drop of the individual curves. The shoulder tile drops about 10 to 15 years earlier in Schneider von Deimling et al. (2021) model and for all other tiles the timing is almost identical. It should be noted that the two road tiles are shifted in their depth by about 30cm.

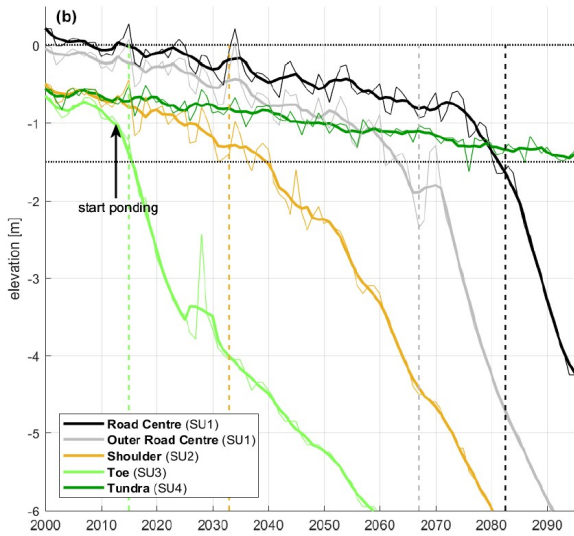


Figure 79: Temporal evolution of maximum thaw depth (MTD) for Dalton Highway from vulnerable case of Schneider von Deimling et al. (2021) for all structural units under RCP8.5 warming - conservative case without ponding at the toe.

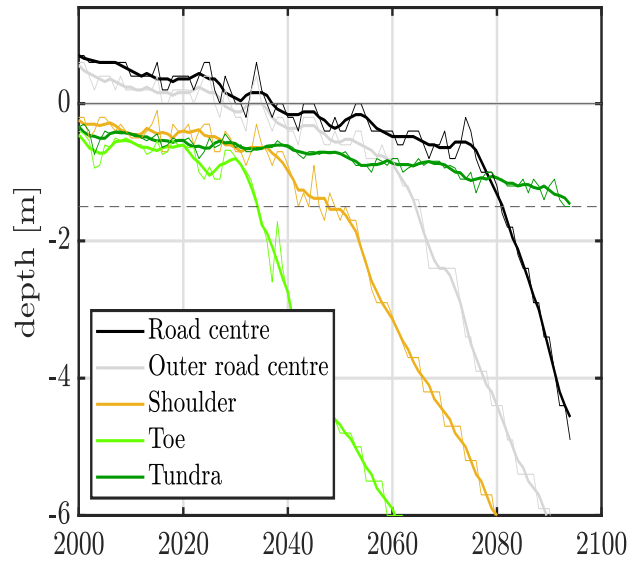


Figure 80: Temporal evolution of maximum thaw depth (MTD) for Dalton Highway with excess ice from my model results for all structural units under RCP8.5 warming - conservative case without ponding at the toe.

The trumpet tiles for road and tundra (Figure 81 and 82) show a shift to much warmer temperatures over the period of investigation. The change in maximum temperatures in 2090 is particularly drastic, with an extreme increase in AL below the gravel layer into the silt and sand, which is expected to cause subsidence and dramatic damage to the road.

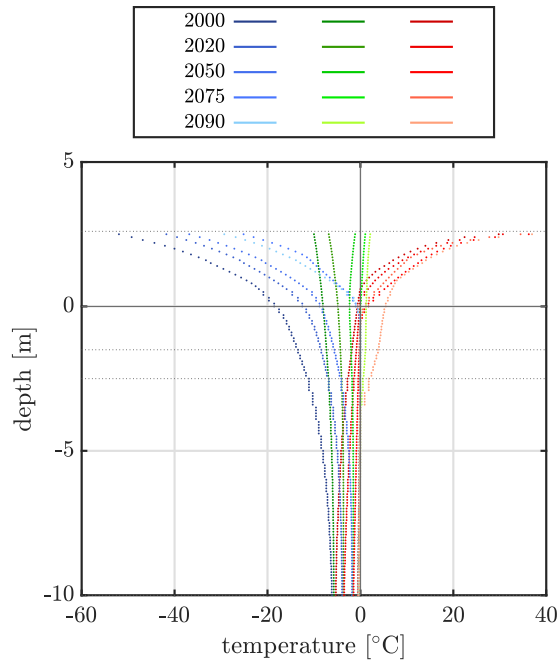


Figure 81: Modelled trumpet curve for road tile with max. (red), mean (green), and min. (blue) temperatures within the specified years 2000, 2020, 2050, 2075, and 2090 for Dalton. The dashed lines show the layer boundaries air-gravel, gravel-silt, and silt-bedrock. The solid line refers to the tundra surface, thus the road is elevated above.

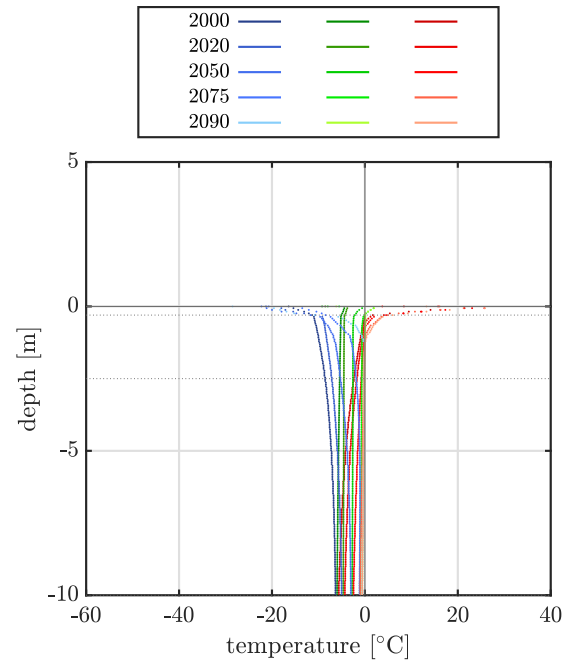


Figure 82: Modelled trumpet curve for road tile with max. (red), mean (green), and min. (blue) temperatures within the specified years 2000, 2020, 2050, 2075, and 2090 for Dalton. The dashed lines show the layer boundaries peat-silt, and silt-bedrock. The solid line refers to the tundra surface.

## B Temperature profiles old boreholes

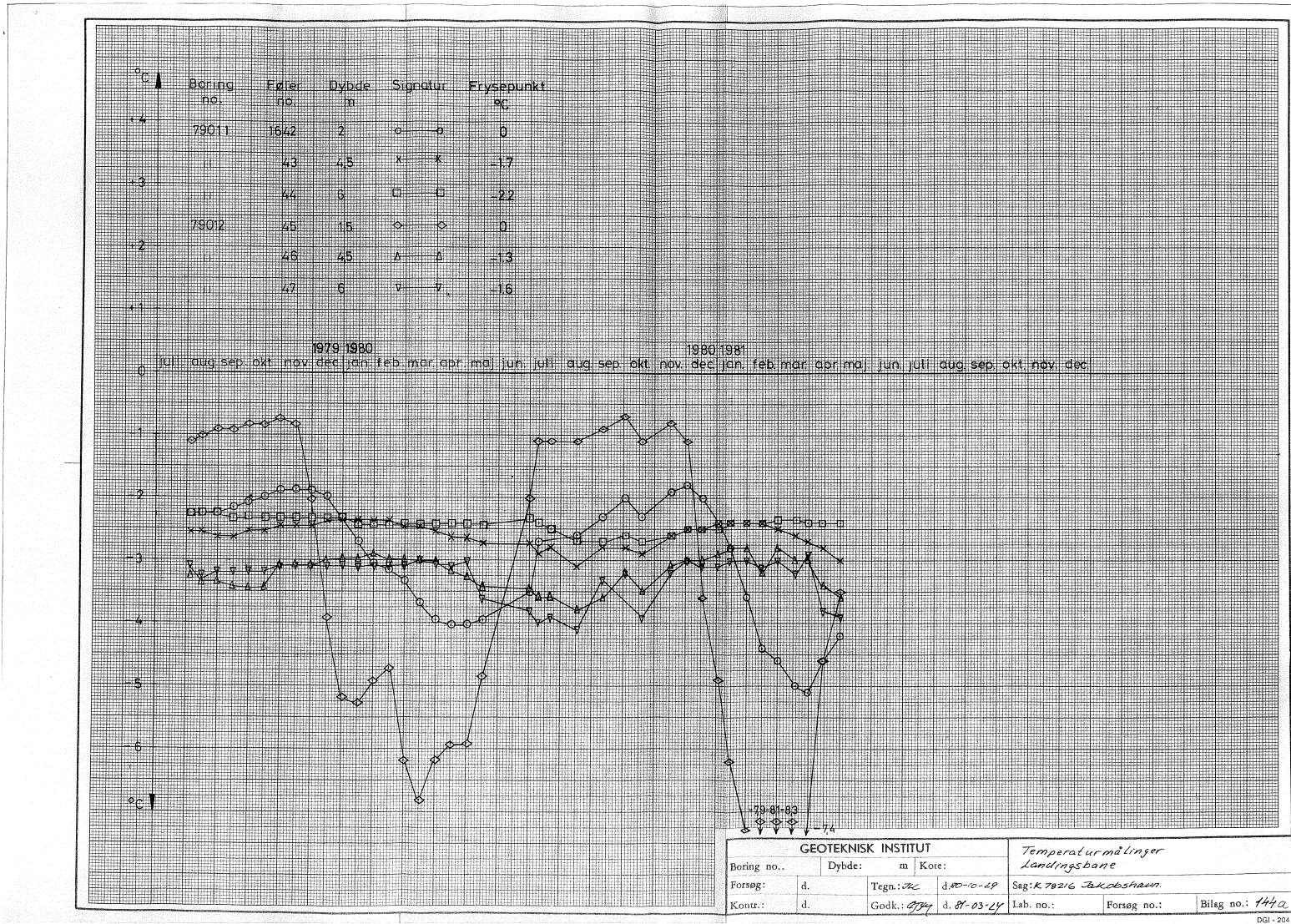


Figure 83: Temperature profiles of some two old boreholes at the airport in Ilulissat from August 1979 to April 1981 with temperatures measured in three different depths.

### C Trumpet plots

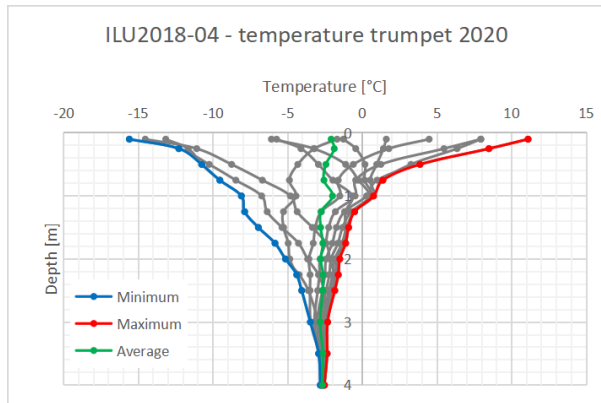


Figure 84: Temperature trumpet of borehole ILU2018-04 for 2020

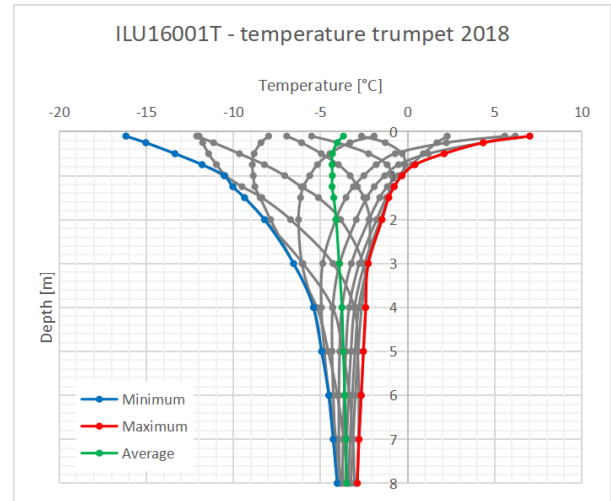


Figure 85: Temperature trumpet of borehole ILU16001T for 2018

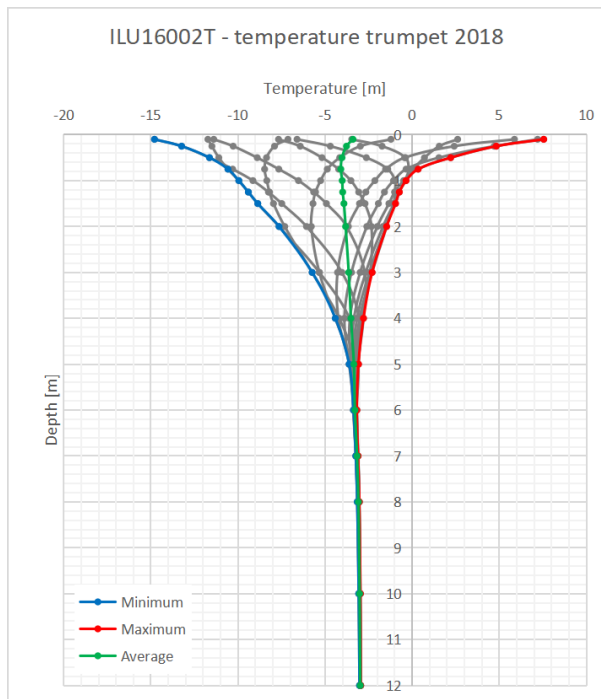


Figure 86: Temperature trumpet of borehole ILU16002T for 2018

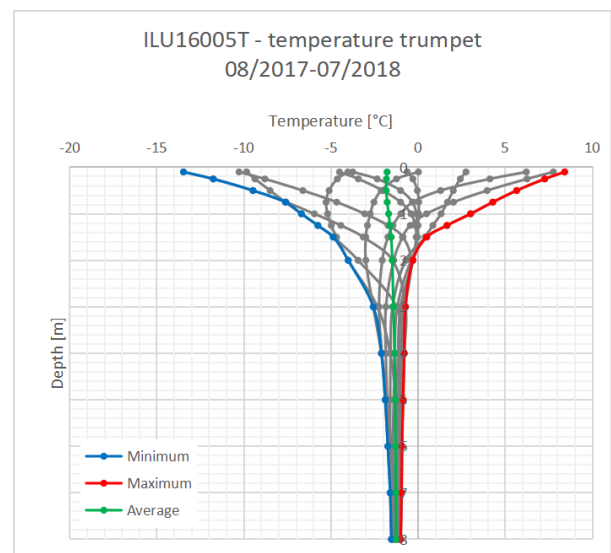


Figure 87: Temperature trumpet of borehole ILU16005T from August 2017 to July 2018

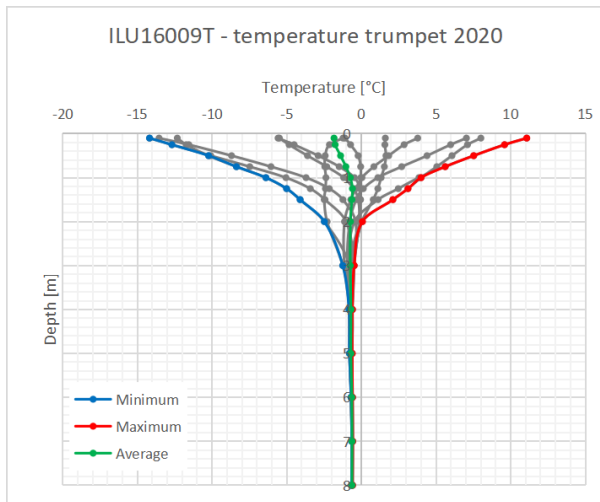


Figure 88: Temperature trumpet of borehole ILU16009T for 2020

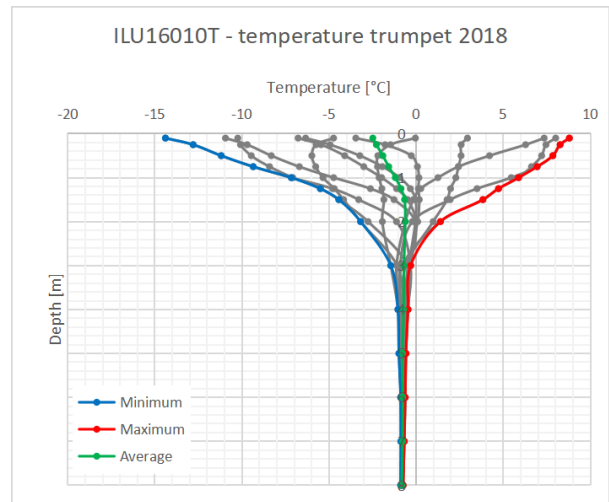


Figure 89: Temperature trumpet of borehole ILU16010T for 2018

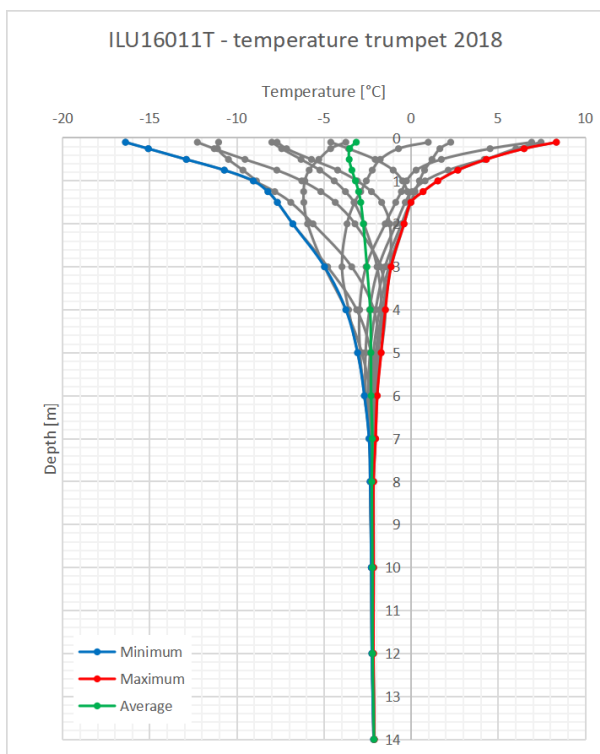


Figure 90: Temperature trumpet of borehole ILU16011T for 2018

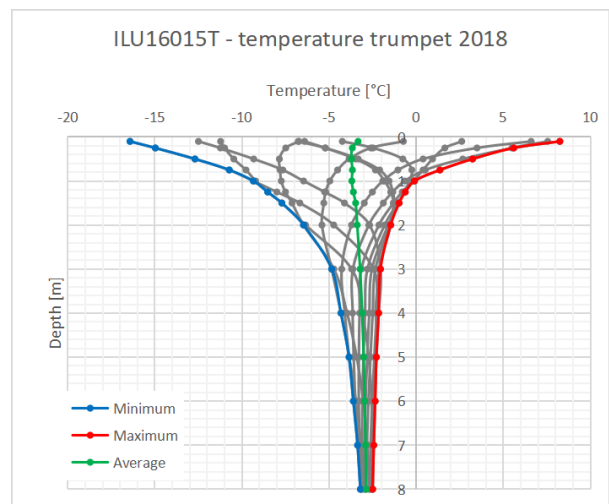


Figure 91: Temperature trumpet of borehole ILU16015T for 2018

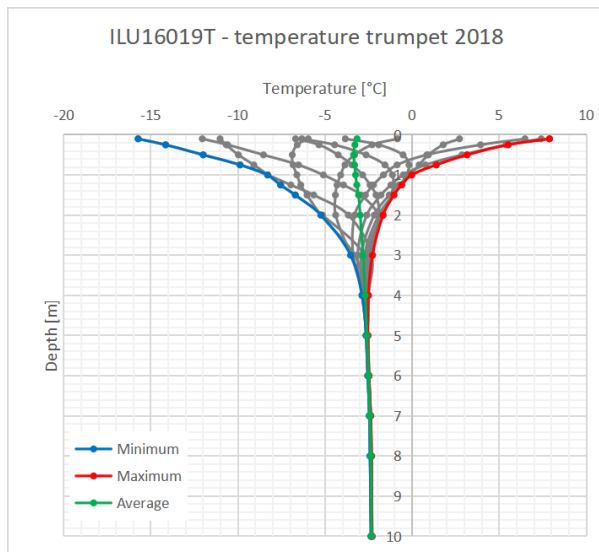


Figure 92: Temperature trumpet of borehole ILU16019T for 2018

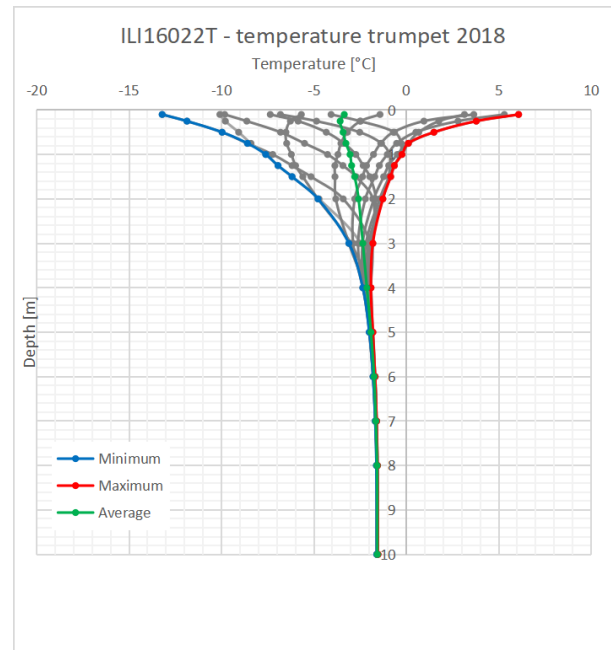


Figure 93: Temperature trumpet of borehole ILU16022T for 2018